Behrmann, J.H., Lewis, S.D., Musgrave, R.J., et al., 1992
Proceedings of the Ocean Drilling Program, Initial Reports, Vol. 141

9. SITE 862[1]

Shipboard Scientific Party[2]

HOLE 862A

Date occupied: 24 December 1991, 1642[3]

Date departed: 25 December 1991, 0615

Time on hole: 13 hr, 33 min

Position: 46°30.475'S, 75°49.603'W

Bottom felt (rig floor; m, drill-pipe measurement): 1286.3

Distance between rig floor and sea level (m): 11.44

Water depth (drill-pipe measurement from sea level, m): 1274.9

Total depth (rig floor, m): 1308.4

Penetration (m): 22.1

Number of cores (including cores with no recovery): 5

Total length of cored section (m): 22.1

Total core recovered (m): 21.45

Core recovery (%): 97.1

Oldest sediment cored:
Depth (mbsf): 22.1
Nature: Matrix-supported conglomerate
Age: late Pliocene

HOLE 862B

Date occupied: 25 December 1991, 0615

Date departed: 25 December 1991, 2030

Time on hole: 14 hr, 15 min

Position: 46°30.475'S, 75°49.603'W

Bottom felt (rig floor, m; drill-pipe measurement): 1280.0

Distance between rig floor and sea level (m): 11.44

Water depth (drill-pipe measurement from sea level, m): 1268.6

Total depth (rig floor, m): 1322.9

Penetration (m): 42.9

Number of cores (including cores with no recovery): 4

Total length of cored section (m): 25.4

Total core recovered (m): 6.07

Core recovery (%): 23.9

Oldest sediment cored:
Depth (mbsf): 21.4
Nature: Silty claystone to claystone
Age: late Pliocene

HOLE 862C

Date occupied: 25 December 1991, 2030

Date departed: 27 December 1991, 0000

Time on hole: 1 day, 3 hr, 30 min

Position: 46°30.510'S, 75°49.566'W

Bottom felt (rig floor; m, drill-pipe measurement): 1239.0

Distance between rig floor and sea level (m): 11.44

Water depth (drill-pipe measurement from sea level, m): 1228.6

Total depth (rig floor, m): 1341.1

Penetration (m): 102.1

Number of cores (including cores with no recovery): 9

Total length of cored section (m): 62.1

Total core recovered (m): 1.97

Core recovery (%): 2.2

Oldest sediment cored:
Depth (mbsf): wash core: 0 to 40
Nature: Silty claystone and clayey siltstone
Age: late Pliocene to late Pleistocene

Principal results: Site 862 is located near the crest of the Taitao Ridge, a prominent bathymetric ridge that juts out from the South American continental margin approximately 25 km south of the present location of the Chile Triple Junction. Because of the close proximity of the Taitao Ridge to the Taitao Ophiolite, exposed 20 km to the east on the Taitao Peninsula, and marine geophysical data that suggest that the Taitao Ridge is of oceanic affinity, the Taitao Ridge was anticipated to be of oceanic origin. It might be in the process of accretion to the Chile Trench forearc. Drilling at Site 862 confirmed that the Taitao Ridge is underlain by igneous material, but the apparent youthful age of the sediment cores of the Taitao Ridge, less than approximately 3 Ma, and the recovery of likely dacitic and rhyolitic materials from the ridge, indicate that the origin and tectonic evolution of the Taitao Ridge is more complex than originally hypothesized. Three holes were drilled at Site 862; these are discussed together.

Two rock units were identified at Site 862: Unit I represents the thin sediment cover that blankets the Taitao Ridge; it is divided into three subunits. Subunit IA, approximately 1.5 m thick, is composed of silty clay that grades to clayey silt and silty fine sand with clay. Subunit IB represents an increase in lithification of Subunit IA materials, comprising claystone, silty claystone, and sandstone. Subunit IC represents the same lithology as Subunit IB, but with the addition of hydrothermal alteration deposits immediately above basement. The total sediment thickness at Site 862 is about 23 m.

Lithologic Unit II is composed of apparently intercalated submarine basalt, dacite, rhyodacite, and rhyolite flows with occasional sediment interbeds. Core 141-862B-2X recovered the depositional contact between Unit I sediment and igneous basement, and shows a clear 2-cm-thick hydrothermal reaction zone in the basal sediment. Igneous clasts display vesicular glassy chilled margins that can occasionally be observed to grade into variolitic plagioclase textures. Recognition of intersertal, subophitic, and ophitic textures suggest that a range of depths within cooling units was recovered.

The basalts are subalkalic to tholeiitic, with phenocrysts of olivine, clinopyroxene, and plagioclase. In the dacite specimens, hornblende phenocrysts often display pristine borders where they abut against plagioclase

[1]Behrmann, J.H., Lewis, S.D., Musgrave, R.J., et al., 1992. *Proc. ODP, Init. Repts.*, 141: College Station, TX (Ocean Drilling Program).
[2]Shipboard Scientific Party is as given in the list of participants preceding the contents.
[3]All times are local time, UTC – 3 hr.

phenocrysts, but are altered where they border the groundmass. This suggests that the hornblende is a primary phase in the magma chamber that erupted this material.

Drilling may have recovered a sequence of interlayered basalt and dacite to rhyolite flows, but the small size of many of the recovered clasts may have allowed a sequence of recovery in the core liner that no longer reflects the original stratigraphy. What is clear, though, is that the basement of the Taitao Ridge is likely composed of both basaltic and dacitic-to-rhyolitic eruptive materials.

Biostratigraphic observations from Site 862 indicate late Pliocene and Pleistocene ages for all the recovered sediments, and paleowater-depth estimates from benthic foraminifers bracket the present depth of the Taitao Ridge. All samples from the sediments of the Taitao Ridge show normal magnetizations. However, inclinations are 30°–35° shallower than expected for this latitude, and primary magnetostratigraphy could not be determined. Complex multiple magnetic overprints in Core 141-862A-3H imply that moderate-temperature hydrothermal activity on this part of the ridge continued until after deposition of at least the lower 4.25 m of the sediment column.

Deformation of the sediment section at Site 862 is dominated by structures related to normal faulting. Both faults and bedding are often mineralized, providing dramatic planar markers for structural analysis. The local topography surrounding Site 862 is very steep, suggesting that gravity sliding may be an important element of the deformational driving force. Recognition of boudinage of sand layers, implying some degree of brittle behavior of the sediments, suggests that deformation post-dates lithification to a large extent. No igneous samples were recovered in original orientation, so no structural analyses could be performed on those lithologies.

The total organic carbon content of the sediment section at Site 862 never exceeds 0.25%. CPI analysis indicates that the organic contents in all sediment samples are relatively mature, as does the presence of small quantities of gasoline-range hydrocarbons. This level of thermal maturity in such young, thin sediments that have never been deeply buried indicates deposition on hot, volcanic basement with vigorous hydrothermal activity. This relationship supports the inference that the Taitao Ridge cannot be much older than its sediment cover.

The seismic velocity of the sediment drilled is about 1600 m/s throughout the section, and both bulk density and grain density are constant downsection. Similarities in these properties suggest that the sediment at Site 862 is of similar provenance to that at Sites 859 and 861.

Radiometric ages from the Taitao Ophiolite are clustered between 3 and 5 Ma (early Pliocene to earliest late Pliocene), and foraminifer-bearing strata within the ophiolite yielded a late Pliocene-Pleistocene fauna (Forsythe and Prior, this volume). The probable age of the basement of the Taitao Ridge overlaps with the age of the Taitao Ophiolite. Dacites and rare rhyodacites and rhyolites have been reported from the Taitao Ophiolite (Forsythe and Prior, this volume), together with basalts and basaltic andesites. The similarity between this assemblage and the basement recovered at Site 862, together with the concordance in their ages, suggest that both features are genetically related and may in fact form one tectonostratigraphic unit.

Magnetic anomalies on the Antarctic Plate to the north of the Taitao Ridge at the same distance from the spreading axis correspond to the Nunivak Subchron, roughly 4.2 Ma. The basement at Site 862 may be close to this age, in which case the Taitao Ridge probably arose by volcanism at the spreading axis. Alternatively, if the basement is late Pliocene in age, then Taitao Ridge volcanism occurred off the spreading axis. The strike of the Taitao Ridge follows the Taitao Fracture Zone, and it may be that the ridge arose from volcanism along this fracture zone.

BACKGROUND AND OBJECTIVES

Site 862 is located near the crest of the Taitao Ridge, a bathymetric promontory that extends to the southwest from the continental margin offshore from the Taitao Peninsula (Fig. 1). Because of its close proximity to the Taitao Ophiolite mapped onshore just 20 km to the east (Forsythe and Nelson, 1985), and its geophysical characteristics discussed below, the Taitao Ridge has been hypothesized to be an offshore extension of the Taitao Ophiolite. The Taitao Ophiolite onshore is of early Pliocene age, young enough for its emplacement in the South American continental margin to be related to the passage of the triple junction. Thus, the Taitao Ridge may represent an ophiolite body in the process of emplacement into the Chile Trench. Drilling into the Taitao Ridge can potentially provide detailed information about the timing, rates, and mechanisms of ophiolite emplacement that can be applied to the study of other ophiolites around the world. Specific drilling goals at Site 862 include determining the lithology of the basement material of the Taitao Ridge, and determining its age and chemical composition for comparison to the Taitao Ophiolite and to the surrounding oceanic crust.

The Taitao Ridge extends southwestward from the continental margin, parallel to the northwestern side of the Taitao/Tres Montes Peninsula. The bathymetric expression of the Chile Trench is interrupted by the Taitao Ridge, with the axis of the trench deflected from its roughly north-south trend north of the Taitao Ridge to a more southwesterly trend south of the Taitao Ridge. The summit of the Taitao Ridge reaches to within 400 m of the sea surface seaward of the shelf edge, and the crest of the ridge deepens to the southwest. Site 862 is located near the crest of the ridge, about halfway along its length, in about 1250 m water depth (Fig. 2).

Marine geophysical observations indicate that the Taitao Ridge is underlain by material akin to oceanic crust. First, magnetic anomaly profiles over the Taitao Ridge show two strongly lineated anomalies with wavelengths and amplitudes that are characteristic of seafloor- spreading magnetic anomalies (Fig. 3). Second, the free-air gravity anomaly associated with the Taitao Ridge reaches an amplitude of about 200 mGal, indicating that the Taitao Ridge is underlain by material of high density. Third, seismic reflection profiles across the Taitao Ridge image no internal structure and indicate high seismic velocities, consistent with an igneous lithology for Taitao Ridge basement (Fig. 4).

Seismic Line 762 (Fig. 4) does not image the structural contact between the margin of the Taitao Ridge and the surrounding oceanic crust of the Antarctic Plate clearly enough to ascertain whether or not subduction is taking place there. Hence, it is unclear whether the Taitao Ridge is presently part of the Antarctic Plate and is converging with South America, or if the Taitao Ridge is already part of the South American Plate, and the Antarctic Plate is being subducted beneath it.

The Taitao Ridge lies along strike of and co-linear with the projection of the Taitao Fracture Zone farther offshore. This spatial relationship suggests that the Taitao Ridge may have originated through volcanic activity associated with "leaky" transform fault deformation along the Taitao Fracture Zone. Alternatively, the Taitao Ridge could have originated through excess volcanism at the ridge crest, or through structural offscraping and imbrication of oceanic crust at the subduction zone. The determination of the age of the basement of the Taitao Ridge, and a comparison of its chemical signature with those of both the oceanic crust and the onshore ophiolite, will provide important constraints on the origin and kinematic evolution of this feature.

OPERATIONS

Site 862

After returning from Puerto Quellon following a medical evacuation, the ship proceeded to the waypoint for the start of the pre-site survey for proposed Site SC-6 and deployed seismic gear. Two passes over the target area were required to select an optimum drill site where the maximum sediment thickness was available. Operations at Site 862 commenced at 1642 hr (local time is used throughout, local = UTC − 3 hr), 24 December 1991, when

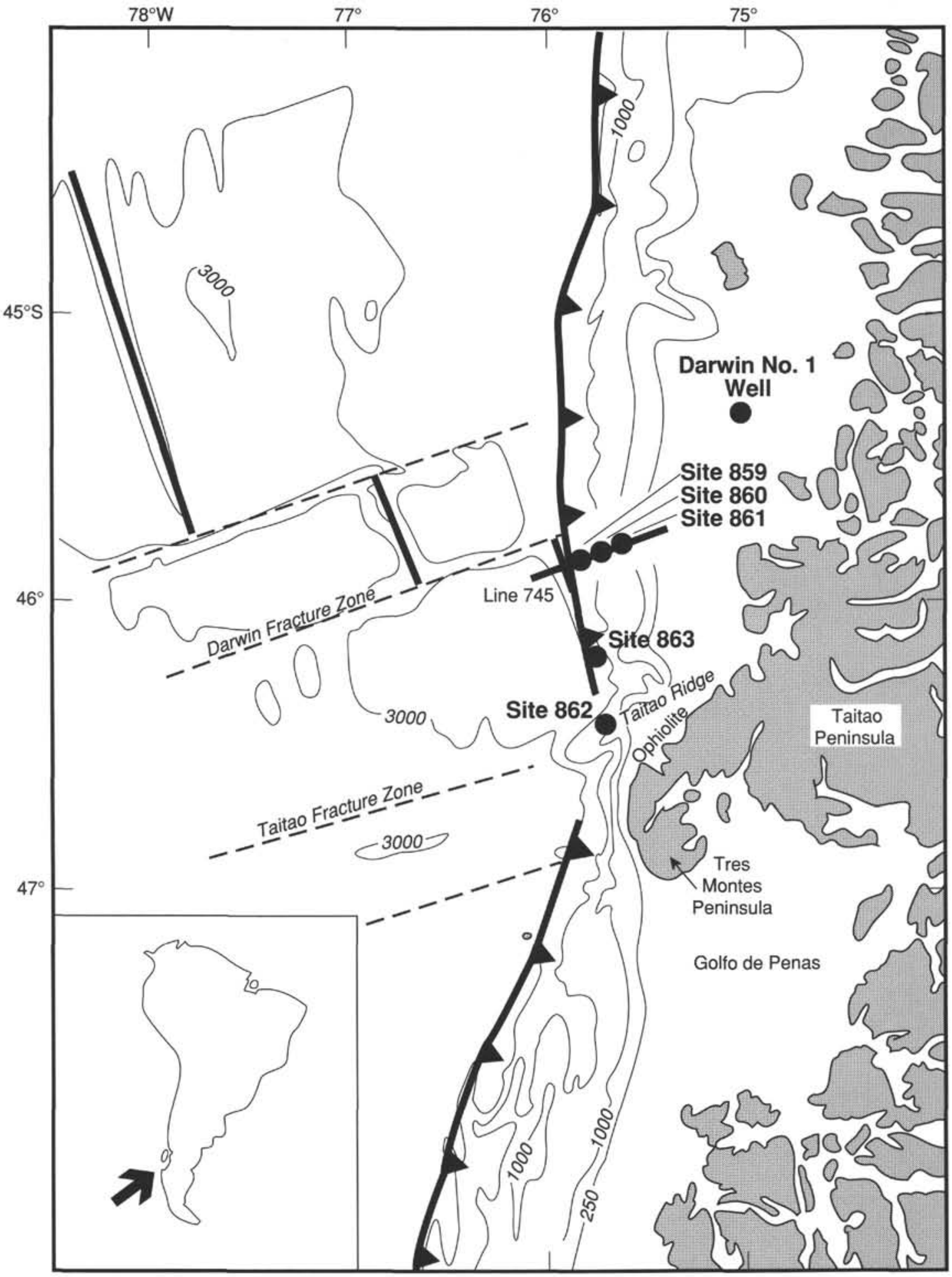

Figure 1. Location map showing the position of the Taitao Ridge, the Taitao Fracture Zone, the Taitao Peninsula, and the Taitao Ophiolite.

a 14-kHz Datasonics commandable/releasable beacon was dropped. The ship returned to the beacon location to begin dynamic positioning. The drill collars were picked up to make up an advanced piston corer/extended core barrel/motor-driven core barrel (APC/XCB/MDCB) bottom-hole assembly (BHA).

No more than 100 m of sediment was expected over basement; at least 60 m of sediment was considered desirable to enable the hole to be spudded effectively. A precision depth recorder (PDR) water-depth measurement indicated firm seafloor and maximum available sediment thickness at 1239 meters below sea level (mbsl) but, as was becoming customary for this leg, both PDR and apparent driller's tag were misleading. Thus, four APC water cores were taken in an attempt to locate the mud line accurately; this was finally found at 1275 mbsl after a second tag.

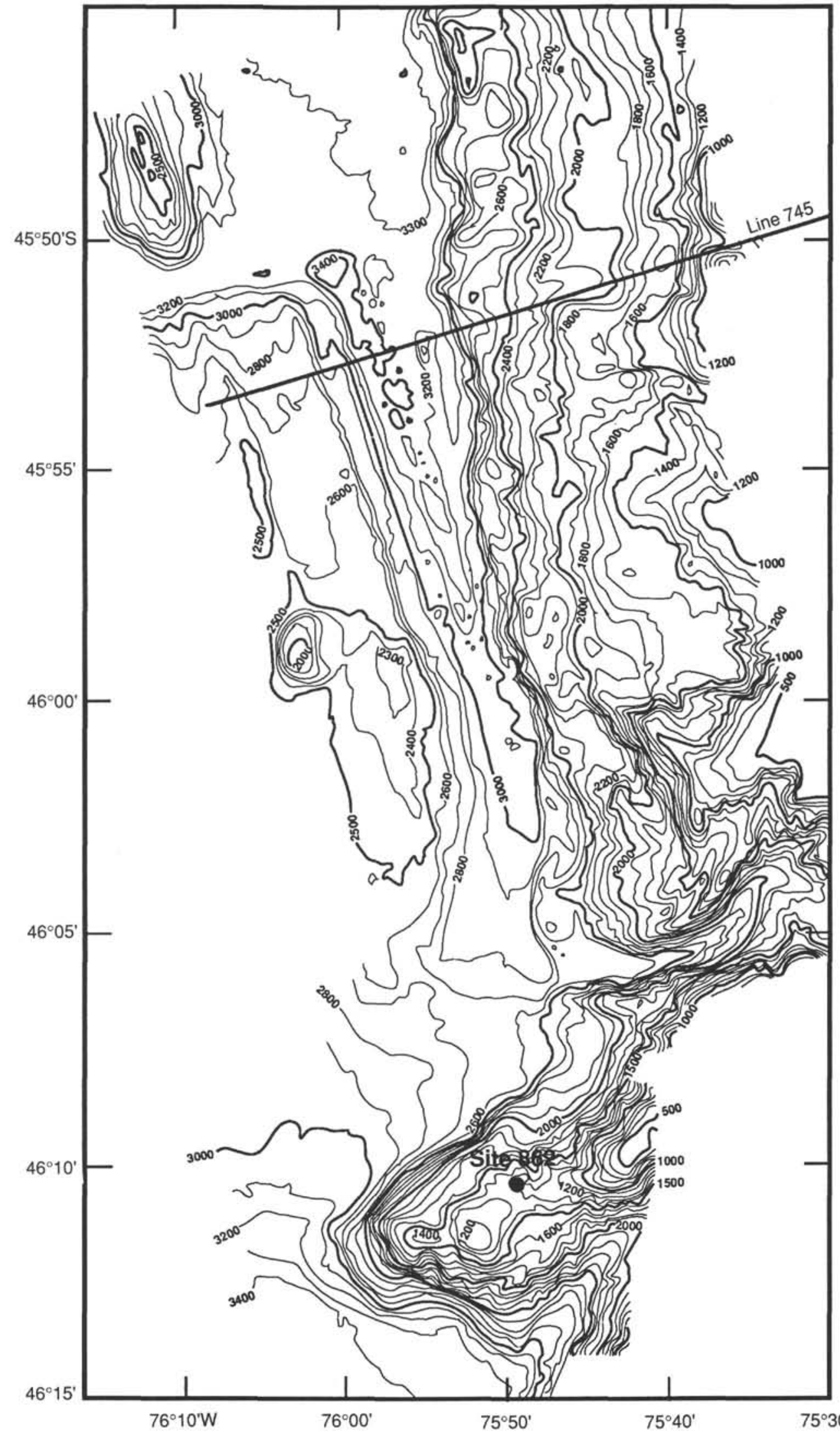

Figure 2. SeaBeam swath bathymetric map of the Chile Triple Junction region, showing Taitao Ridge and Site 862.

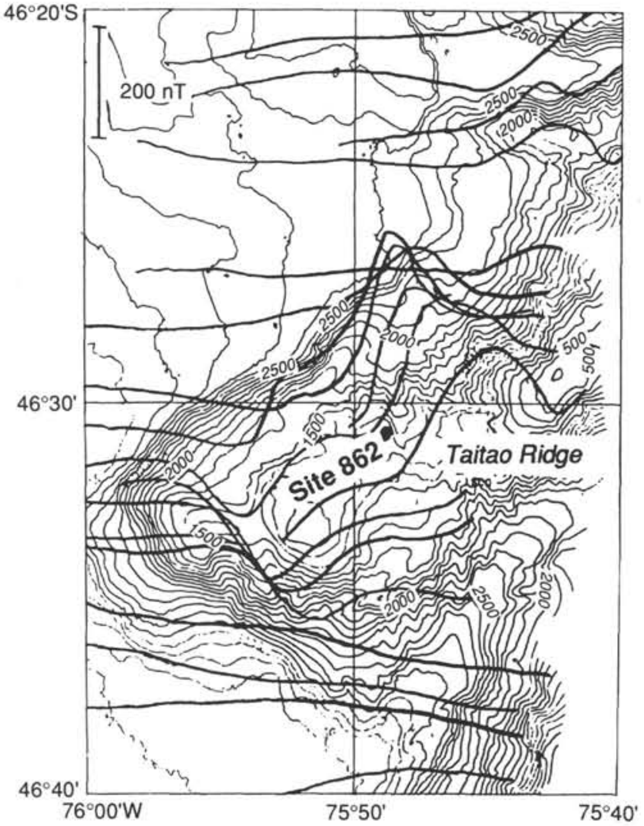

Figure 3. Magnetic anomalies across the Taitao Ridge.

Hole 862A

Four APC cores were taken with some difficulty (Table 1). Full stroke was achieved on the first two cores but the second required 100,000 lb ("kips") overpull to extract from the sediment. The third APC core did not achieve a full stroke and overpulled to 60 kips. The fourth (and last) APC core penetrated less than 1 m and defined the piston-coring refusal point.

The coring mode was changed to XCB and a single-core attempt ended in a broken XCB cutting-shoe spacer sub when the core barrel encountered hard rubble at 22.1 meters below seafloor (mbsf). Both the cutting shoe and broken half of the spacer sub were left in the hole along with the core catcher and any core that had been captured. The junk in the hole ended any further possibility of deepening in this particular spot, so the bit was pulled above the seafloor to start a second hole. The bit cleared the mudline at 0615 hr, Christmas Day, 1991, ending Hole 862A.

Hole 862B

The vessel was offset 10 m southeast, and Hole 862B was spudded with an XCB core barrel and washed to 17.5 mbsf. Recovery in the wash barrel was 0.11 m of highly disturbed sediment between rocky cobbles. Three additional XCB cores were laboriously taken in what appeared to be a rubble zone with some clay and gravel constituents. All recovery, ranging from 0.75 to 4.12 m, was made up of roller stones that did not appear to have been trimmed or recently fractured. One TC-insert XCB cutting shoe had its cutting structure obliterated and two others suffered significant damage. Torquing in the hole was severe and cuttings consistently packed-off the annulus around the bit or drill collars when flow rates were too high or held constant for more than a few minutes. Fill in the hole became a serious problem, amounting to 8 m after Core 141-862B-4X. Rate of penetration in Cores 141-862B-3X and -4X (the last two cores drilled in this hole) was as low as 3 m/hr and an additional hour or more was spent cleaning out fill to reach bottom.

As it was apparent that the objective of reaching and sampling solid basement was unlikely to be achieved at this location with XCB technology, the hole was terminated and the pipe was pulled to change over to the rotary core barrel (RCB) coring method. The option to deploy the MDCB was eliminated by the rubble fill conditions experienced at the end of this short (42.9 m) hole. Because the MDCB must be inserted into the drill string for pump-down to the bit while the string is supported on the elevators, and not heave compensated, the bit must be off bottom at that time. The hole was accumulating rubble fill as soon as the bit was pulled off bottom, so by the time the MDCB could be delivered to the bit it would not be possible to core from a clean interface at the bottom of the hole. It is not possible to clean out fill without simultaneously starting the MDCB. Coring in rubble fill would not have been either a valid test for the MDCB nor provide any chance of contributing to the science objectives of the hole. Therefore the hole was abandoned, the pipe was tripped, and the hole officially ended when the bit reached the drill floor at 2030 hr on Christmas Day.

Hole 862C

The vessel was offset 100 m SE before starting Hole 862C in hopes of finding less rubble. The RBI C-4 RCB roller cone bit was run to bottom and the hole was spudded at a depth of 1228.6 mbsl; apparently the 100 m offset had been generally uphill. A core barrel was in place in the BHA and the hole was initially washed to 40 mbsf where coring began. The sediment cover proved to be slightly thicker at this site as rapid penetration was possible to a depth of about 85 mbsf, although core recovery over this zone was very low, consistently less than 5%.

At 0100 hr on 26 December, just prior to spudding Hole 826C, operations were suspended for 30 min while an unidentified vessel on a collision course approached the ship and would not respond to normal radio hailing. Eventually a response was received to hails in Spanish, and the ship, seagoing tug *R-Lenga,* identified itself as a local workboat for servicing lighthouses. Its errand and approach were not adequately explained but it changed course after approaching to within 0.2 nmi and eventually left the area.

RCB coring was continued into the same rubble-dominated zone encountered in Hole 862B at a slightly shallower sub-bottom depth. Total recovery in seven cores was 1.38 m, just over 2%. All recovered material comprised hard-rock roller stones. As in Hole 862B, severe torquing and fill caused difficult coring conditions and very slow progress toward more solid basement. As the debate on the wisdom of continuing to core under such conditions was reaching its climax, the decision was abruptly made for us. The SEDCO crane operator badly cut several fingers on his left hand while using a table saw. The ship's surgeon ordered an immediate medical evacuation to get him to a microsurgery center at the earliest possible opportunity so that he would have the best chance of saving one or more of his damaged fingers.

Therefore, Hole 863C was terminated at 0000 hr on 27 December 1992: last core was Core 141-862C-8R at a depth of 102.1 mbsf (recovery within the drill bit constituted bit Core 141-862C-9B). The drill string was pulled and the ship got under way for Puerto Quellon to rendezvous once again with the same Chilean immigration and medical personnel who had been aboard only a

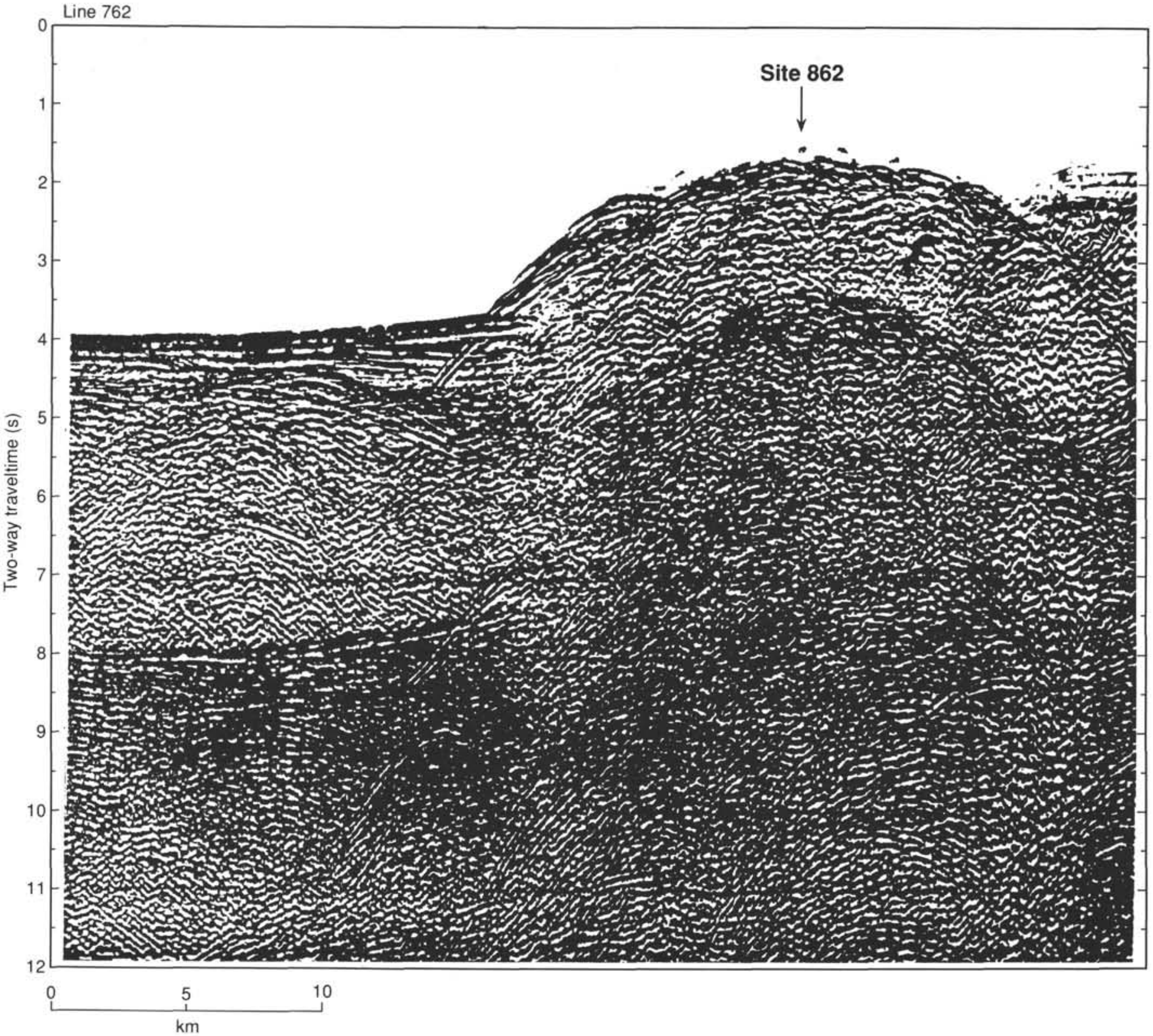

Figure 4. Seismic reflection Line 762 across the Taitao Ridge. Note the lack of internal acoustic definition within the Taitao Ridge, one acoustic characteristic of igneous oceanic basement.

few days earlier. The beacon at the site was abandoned because the weather was too rough to offer any possibility of a successful after-dark beacon recovery.

LITHOSTRATIGRAPHY AND IGNEOUS PETROLOGY

Summary

The lithostratigraphy at Site 862 is characterized by an upper marine sedimentary sequence, extending from the seabed to approximately 22 mbsf, and an underlying series of volcanic rocks that extends to a depth of at least 102 mbsf. The upper sedimentary sequence was recovered by APC coring in Hole 862A with 97% recovery. In Hole 862B, the wash core and the immediately underlying XCB core contained marine sedimentary strata that extended to a depth of 22 mbsf. The lower volcanic units, which include vesicular phyric basalts, dacites, and rhyolites were recovered from Hole 862B (between 22 and 42.9 mbsf) by continued XCB coring, then again in Hole 862C from levels represented by the wash core (0–40 mbsf) and RCB cores to a depth of 102.1 mbsf. Core recovery in the volcanic rocks was only 12% in Hole 862B and 2% in Hole 862C. The sedimentary strata and volcanic rocks are divided into Units I and II, respectively (Fig. 5, Table 2). They are further subdivided into a series of subunits on the basis of the observable changes in their lithologic characteristics (Fig. 6).

Lithologic Units

Unit I (Cores 141-862A-1H through -4X, 141-862B-1W and -2X, and 141-862C-1W; age: Quaternary and late Pliocene; depth: 0–22 mbsf)

Lithologic Unit I is formed by marine sediments that overlie a volcanic sequence encountered at approximately 22 mbsf in Hole

Table 1. Summary of coring operations at Site 862.

Core	Date (Dec 1991)	Time UTC	Depth (mbsf)	Length cored (m)	Length recovered (m)	Recovery (%)	Age
141-862A-							
1H	25	0320	0.0–5.4	5.4	5.38	99.6	U. Pleistocene
2H	25	0430	5.4–14.9	9.5	9.85	103.0	?
3H	25	0530	14.9–20.6	5.7	5.72	100.0	U. Pliocene
4H	25	0630	20.6–21.1	0.5	0.50	100.0	?
5X	25	0900	21.1–22.1	1.0	0.00	0.0	?
Coring totals				22.1	21.45	97.1	
141-862B-							
1W	25	1130	0.0–17.5	17.5	0.26	(wash core)	
2X	25	1330	17.5–27.1	9.6	4.12	42.9	
3X	25	1600	27.1–36.5	9.4	0.75	8.0	
4X	25	1945	36.5–42.9	6.4	1.20	18.7	
Coring totals				25.4	6.07	23.9	
Washing totals				17.5	0.26		
Combined totals				42.9	6.33		
141-862C-							
1W	26	0630	0.0–40.0	40.0	0.50	(wash core)	
2R	26	0700	40.0–46.3	6.3	0.00	0.0	
3R	26	1100	46.3–55.7	9.4	0.07	0.7	
4R	26	1215	55.7–65.1	9.4	0.13	1.4	
5R	26	1315	65.1–74.5	9.4	0.12	1.3	
6R	26	1400	74.5–83.4	8.9	0.43	4.8	
7R	26	1600	83.4–93.1	9.7	0.25	2.6	
8R	26	2200	93.1–102.1	9.0	0.38	4.2	
9B	27	0259	102.1–102.1	0.0	0.09	(bit core)	
Coring totals				62.1	1.38	2.2	
Washing totals				40.0	0.50		
Bit recovery					0.09		
Combined totals				102.1	1.97		

Table 2. Lithostratigraphic chart for Site 862.

Depth (mbsf)	Unit	Subunit	Age	Coring intervals: Hole 862A	Hole 862B	Hole 862C	Lithology
0–6	I	IA	Quat.	Section 141-862A-1H	Section 141-862B-1W-1	Probably not recovered	Medium gray to dark greenish gray silty clay and clayey silt, silty fine sand and clay
6–21		IB	Quat. and u. Pliocene	Section 141-862A-1H-2 to Section 141-862A-3H-4, 50 cm	Section 141-862B-2X-1 to Section 141-862B-2X-CC, 28 cm	Section 141-862C-1W-1, 0-30 cm	Olive gray to dark greenish gray claystone, silty claystone, sand, sandstone
21–22		IC	Pliocene	Section 141-862A-3H-4, 50 cm to bottom of Core 141-862A-4H	Section 141-862B-2X-CC, 28-31 cm	Section 141-862C-1W-1, 30-35 cm	Same as Subunit IB, but with hydrothermal sulfides
22–102	II		Pliocene	not reached	Section 141-862B-2X-CC, 35 cm through Core 141-862B-4X	Section 141-862C-1W-1, 37 cm through Core 141-862C-9B	Intercalated submarine basalt, dacite and rhyolite flows with one indurated layer of sediment (Core 141-862C-6R-1, Piece 6)

862B. The relation of Unit I to the volcanic sequence of Unit II is shown in Figure 5. At Hole 862A, a conglomerate with angular volcanic clasts enclosed within a matrix of oxidized, sulfide-rich, yellowish-gray silty clay was recovered just prior to abandoning the hole at a sub-bottom depth of 22 mbsf. This conglomerate likely represents the basal sediment that overlies the volcanic rocks of Unit II at this location. Hole 862B was washed to 17.5 mbsf. The wash core recovered a mixture of sediment and volcanic rock fragments but was followed by XCB coring that recovered marine sediments to a depth of approximately 22 mbsf, where, at 31 cm in Section 141-862B-2X-CC, a sharp contact was recovered that had the overlying marine sediment of Unit I in depositional contact with the upright glassy rim of a basalt flow. Due to poor recovery and difficult drilling conditions, Hole 862B was abandoned at 42.9 mbsf within the volcanic rocks of Unit II. Hole 862C was washed to a depth of 40.0 mbsf. The wash core (Core 141-862C-1W) recovered a depositional contact between marine sediment and the upright glassy rim of a basalt flow (at 37 cm, Section 141-862C-1W-1), identical in form to that seen at Hole 862B. However, in this case the underlying glassy basalt was separated from the sediment during splitting of the cores and then curated with an intervening plastic spacer. The base of Unit I is thus located within the upper 40 m at Hole 862C. The depth of 22 mbsf was recorded at Hole 862B, for this contact is used as a first

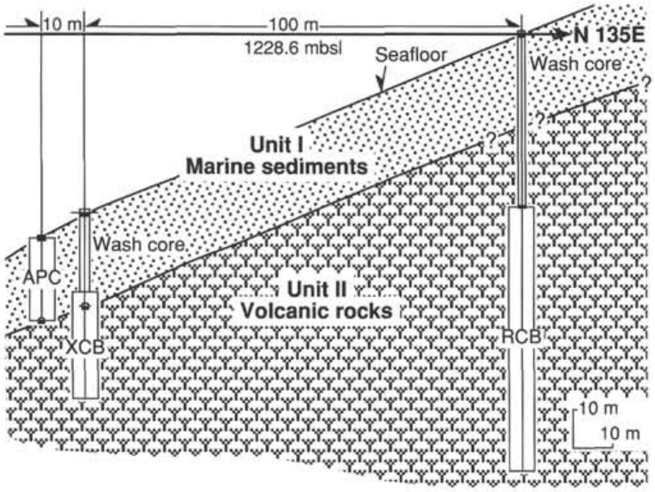

Figure 5. Profile of the Taitao Ridge along the line of section containing the three holes drilled at Site 862 (using the depth below sea level for Hole 862C as the datum). The types of drilling and core recovery are shown. The contact between the upper marine sedimentary unit (Unit I) and the lower volcanic unit (Unit II) was recovered and accurately positioned in Hole 862B; recovered in the wash core in Hole 862C but not accurately located; and likely reached, but not recovered in Hole 862A.

estimate of the base of Unit I in Hole 862C. An improved rate of drilling progress through the wash core at 862C suggests, however, that the sediment sequence at Hole 862C is thicker than at Holes 862A and 862B, which implies that the base of Unit I is closer to 40 mbsf in Hole 862C.

Unit I is subdivided into three short subunits, primarily on the basis of the APC recovery in Hole 862A and XCB recovery in Hole 862B. These are described in detail below.

Subunit IA (Core 141-862A-1H through Section 141-862A-2H-1, and parts of Cores 141-862B-1W and 141-862C-1W; age: Quaternary; depth: 0–6 mbsf)

This subunit is composed of the poorly consolidated marine sediments that were recovered in the upper 6 m of Hole 862A and cobbles recovered at the top of wash cores at Holes 862B and 862C. Short sections of marine sediments and sedimentary rocks recovered in the wash cores of Holes 862B and 862C beneath the upper cobbles likely include segments of correlative strata, but no specific correlation of the recovered sedimentary intervals is made at present with Subunit IA strata of Hole 862A. The following discussion of Subunit IA is drawn principally from observations made of APC cores from Hole 862A.

The subunit is mostly composed of moderately (thinly to thickly) interbedded, medium to dark greenish gray, silty clay to clayey silt, clay, and silty fine sand underneath a surficial drape of pebbly silt. However, at the very top of Section 141-862A-1H-1 are two angular fragments of vesicular, unaltered to slightly altered, moderately plagioclase-hornblende-phyric rhyolite. They are embedded within a pebbly nannofossil sandy silt with abundant sea urchin spines (Fig. 7). These two rhyolite clasts are described as hard-rock units of Subunit IA within the discussion of the igneous petrology that follows. Similarly, in the wash cores, Cores 141-862B-1W and 141-862C-1W, cobbles are found at the very top of the core, overlying short intervals of marine sediment. Thus, at all three holes of Site 862 a thin drape of pebble- to cobble-size clasts appears to be present along the seafloor, mixed within an upper hemipelagic (microfossil-rich) silt.

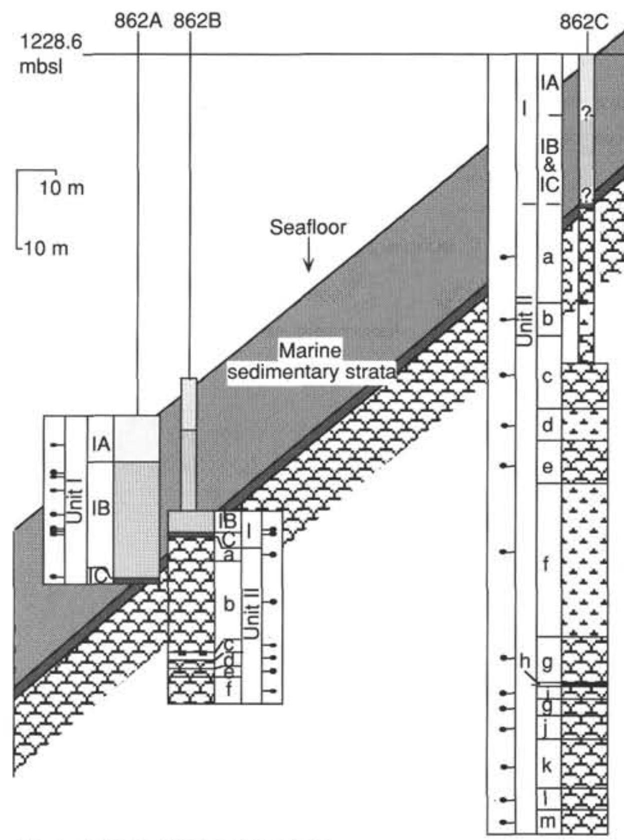

Magmatic/hydrothermal lithologies

Hydrothermal "ocher" zone (with sulfides)

Basaltic volcanics

Rhyolithic and dacitic volcanics

Intercalated metasandstone (calcareous)

Cooling units (ash/glass layers in Unit I)

Figure 6. Vertically exaggerated view of the profile shown in Figure 5, along with a correlation of the lithologic units and subunits at Site 862. Also shown are the discrete eruptive events thought to be recorded by cooling units represented within the volcanic rocks, and glass-rich (mostly nonvesicular tachylite) horizons within the sedimentary strata.

The marine sediment under the surficial drape of pebbly silt includes a number of distinctive bedding intervals that exhibit grading, lamination, and cross-lamination. Figure 8 shows typical bedding characteristics in Subunit IA, where bedding is generally subhorizontal. Graded beds are found only in the top 2 m. Beneath this uppermost interval of graded beds, four discrete zones with cross-laminations are found within very thin (<3 cm) intervals of fine sand that do not appear to be parts of graded or upward-fining sequences. Zones of disturbed bedding in Sections 141-862A-1H-4 and -CC may indicate minor synsedimentary slumping or perhaps disruption produced by burrowing activity.

Two layers containing volcanic lapilli were noted in Subunit IA. The upper layer, which contains coarse sand-size particles of black volcanic glass, occurs at 68–72 cm in Section 141-862A-1H-3. The second layer is within a thin bed of coarse sand occuring from 105 to 106 cm, Section 141-862A-2H-1. This layer contains foraminifers and nonvesicular, angular, black volcanic glass fragments.

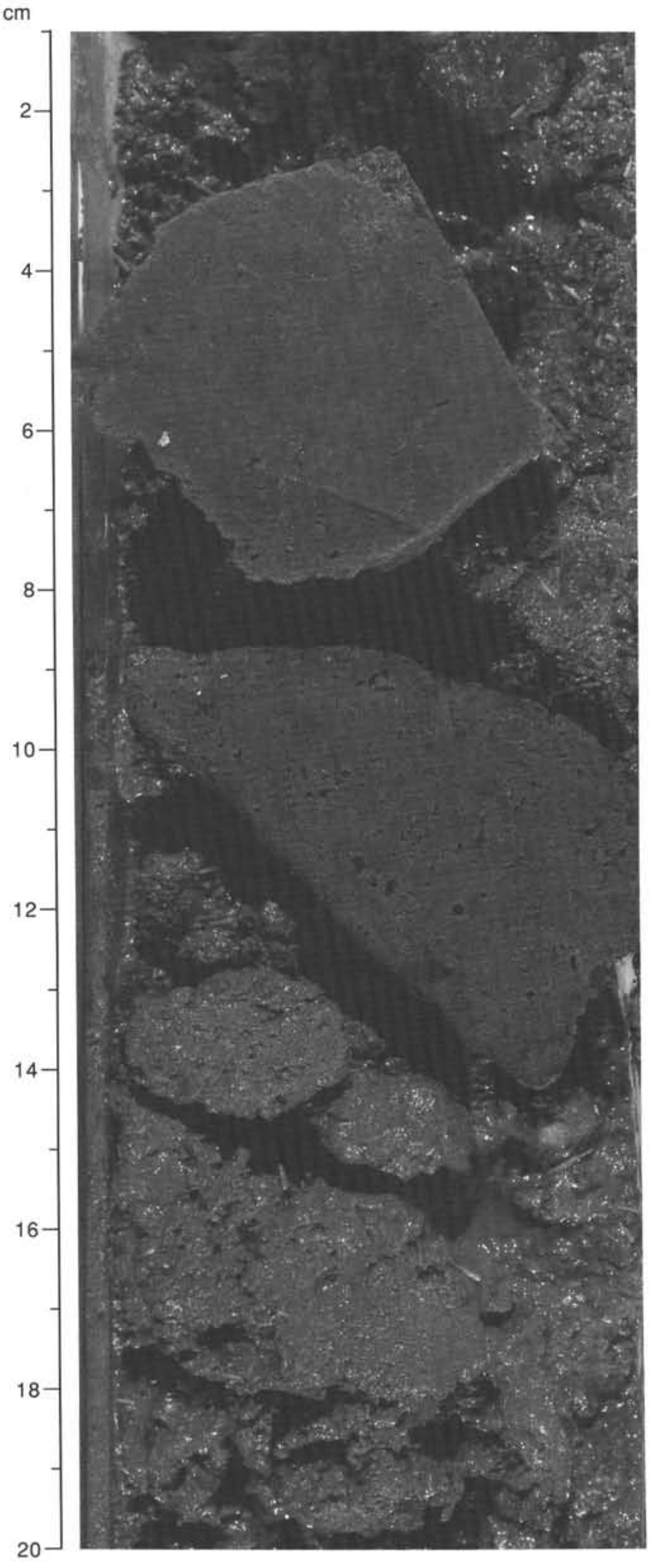

Figure 7. Core photograph of the top 20 cm of Hole 862A, with the angular to subangular vesicular rhyodacite clasts embedded in a pebbly silt with nannofossils and sea-urchin spines. The wash cores from the other holes contained very similar cobbles at the top.

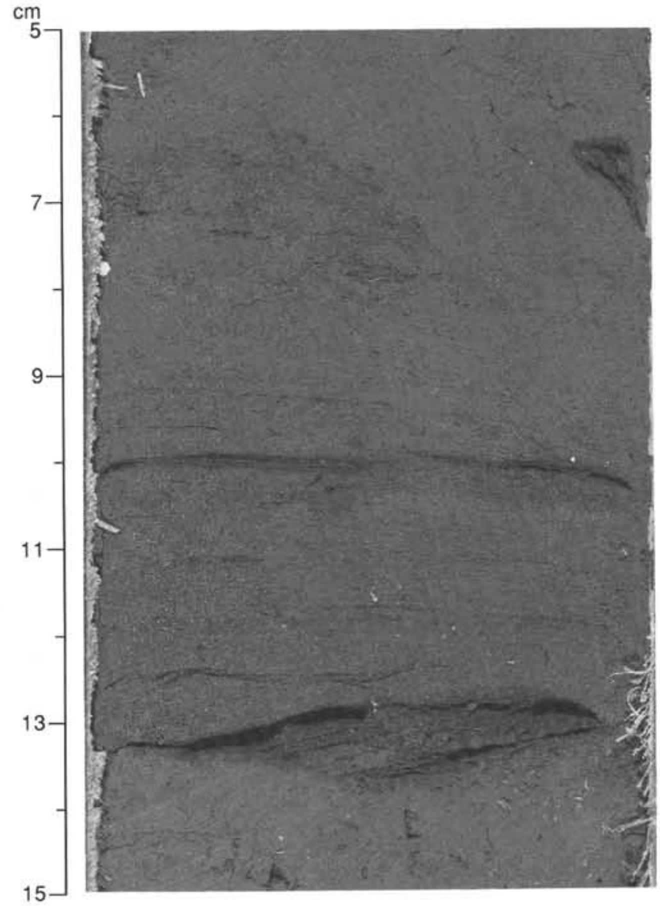

Figure 8. Core photograph of an interval within the middle of Subunit IA where a thin sand bed is found with cross-lamination. Bedding is almost horizontal.

The base of Subunit IA is placed at the first appearance of consolidated sedimentary strata.

Subunit IB (Core 141-862A-2H to Section 141-862A-3H-4 at 50 cm, Core 141-862B-2X to Section 141-862B-2X-CC, 28 cm; age: Quaternary and late Pliocene; depth: 6.0–21.0 mbsf)

Lithologic Subunit IB is composed of the consolidated marine strata seen in Holes 862A and 862B, but excludes those consolidated sedimentary strata at the base of Unit I that have indications of hydrothermal alteration and mineralization (Subunit IC). The consolidated marine sediments of this subunit are composed of mostly olive gray to dark greenish-gray claystone, silty claystone, sand, and sandstone. Intervals of sand and/or sandstone are generally less consolidated than the other lithologies. Overall, these lithologies are moderately interbedded with 1- to 20-cm intervals of planar lamination (Fig. 9), and less common, 1- to 3-cm, intervals of cross-lamination (Fig. 10). Some of the cross-laminations show low-angle reactivation surfaces and scour-fill structures.

Bedding in Subunit IB is variably dipping, and the thicker intervals of nonlaminated claystone and silty claystone are predominantly brecciated in association with normal faulting. In addition, a clastic dike of sand cuts horizontally-bedded sand between 2–6 cm in Section 141-862A-2H-5 (Fig. 11). In Hole 862B, Section 141-862B-2X-1, there are tilted sections that have been scoured and covered by less-tilted strata, suggesting syndepositional deformation (Fig. 12).

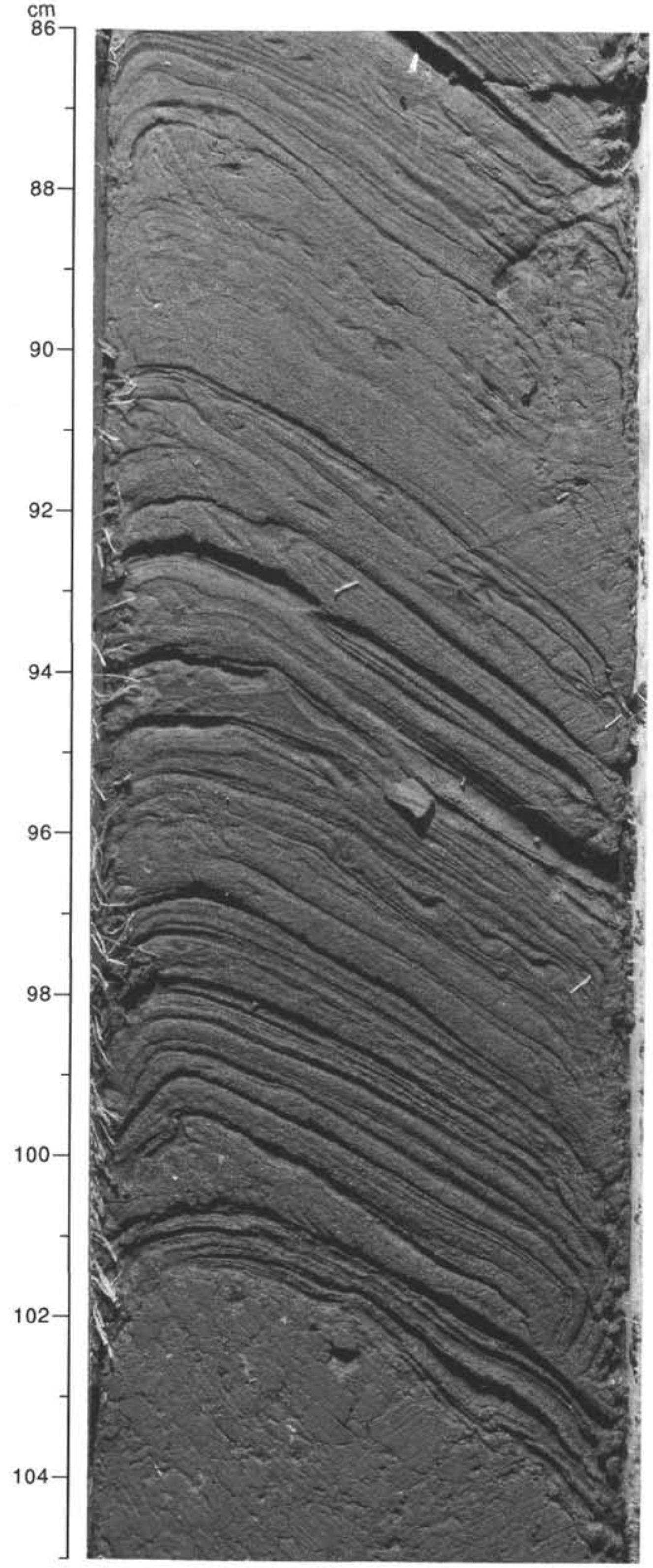

Figure 9. Core photograph of segment within Section 141-862A-3H-2 showing part of a 20-cm-thick zone of planar-laminated silty fine sand within Subunit IB. The sand overlies a clay breccia. A detachment 5–10 mm above the breccia has clear hanging-wall cutoffs. Between 85 and 95 cm are numerous isoclinal folds with axial surfaces parallel to bedding. The amount of structureless sand increases upward.

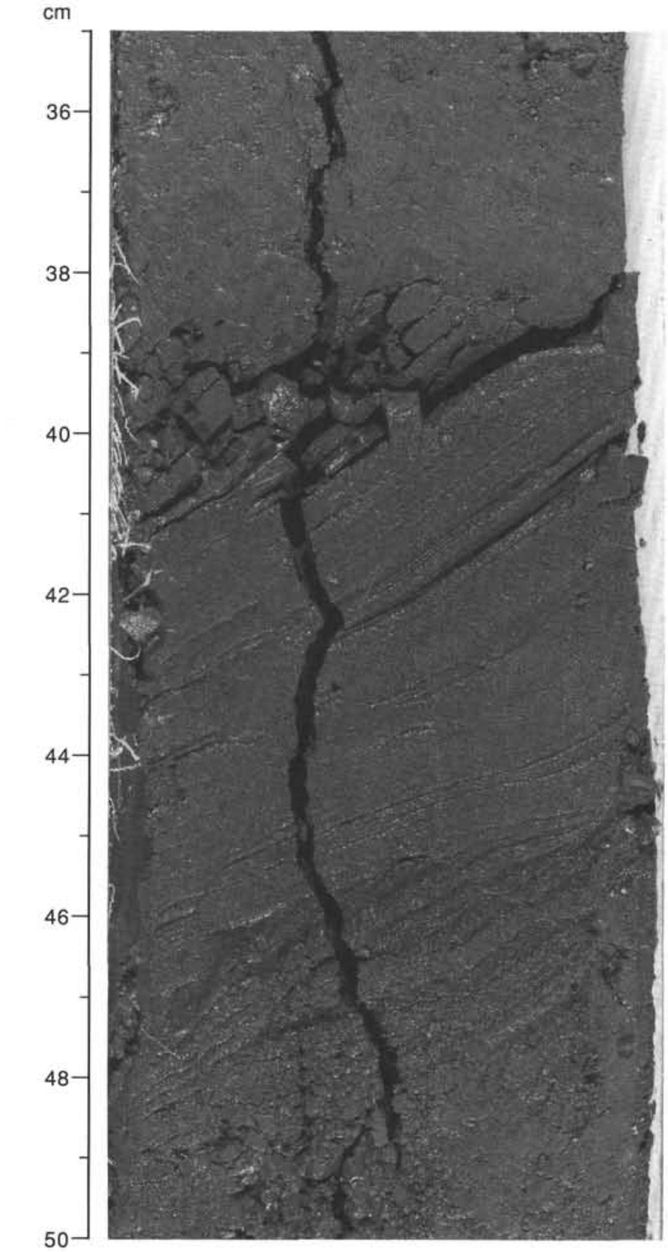

Figure 10. Core photograph showing 10-cm interval of cross-laminated silty fine sand with reactivation and scour-fill structures.

Within the recovered intervals of this subunit in Holes 862A and 862B there are 10 layers with dispersed coarse sand- to pebble-size black, angular, nonvesicular volcanic glass (Fig. 13).

Subunit IC (from 50 cm in Section 141-862A-3H-4 to 22 cm in Section 141-862A-4H-CC, and Sections 141-862B-2X-CC, 22–31 cm, and 141-862C-1W-1, 30–35 cm; age: late Pliocene; depth: 21– 22 mbsf)

This subunit comprises marine sedimentary strata recovered immediately above the volcanic rocks of Unit II, within which occur layers of sediment with brownish to yellowish pigments. The brownish and yellowish colors were first seen at 50 cm in Section 141-862A-3H-4, and continued to the end of recovery from Hole 862A (Fig. 14). At Hole 862B, brownish and yellowish sediment first appears at Section 141-862B-2X-CC, 25 cm, and

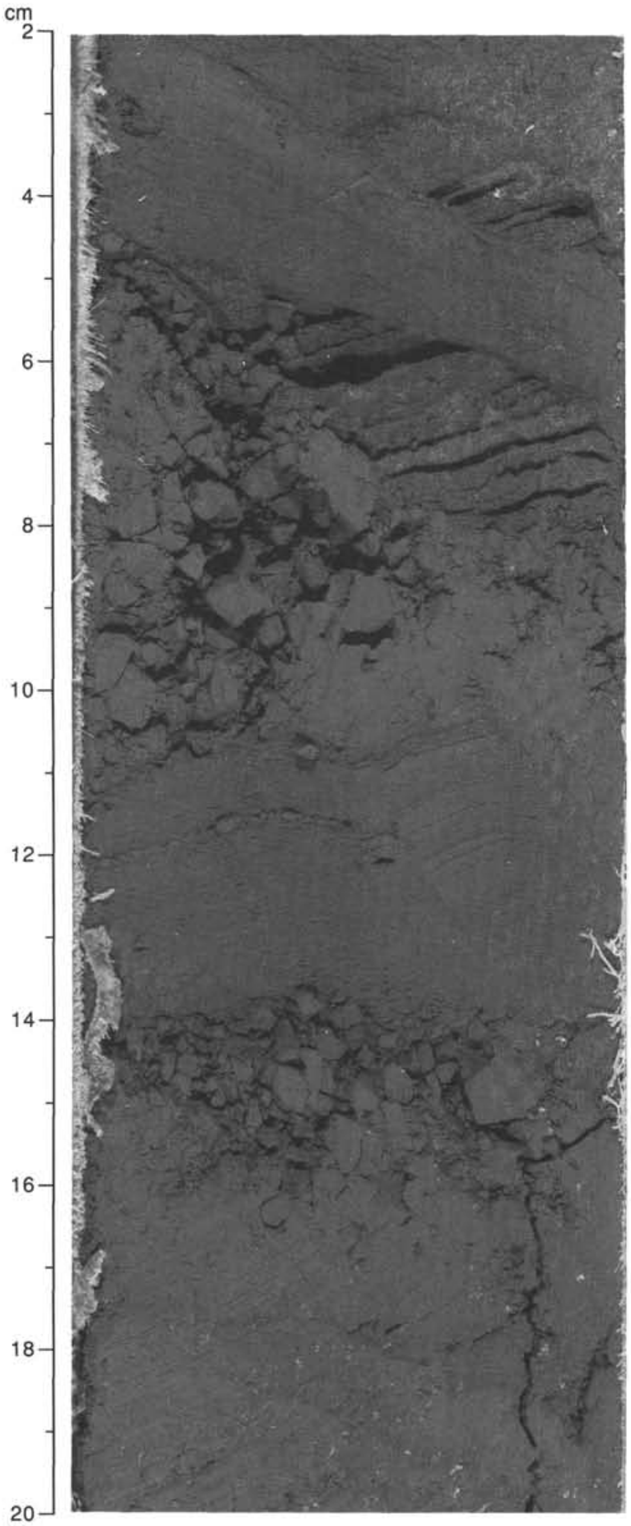

Figure 11. Core photograph of Subunit IB in Section 141-862A-2H-5, 2–20 cm, showing a clastic dike. Layers above and beneath are dipping and affected by faulting and brecciation (see Structural Geology section, this chapter).

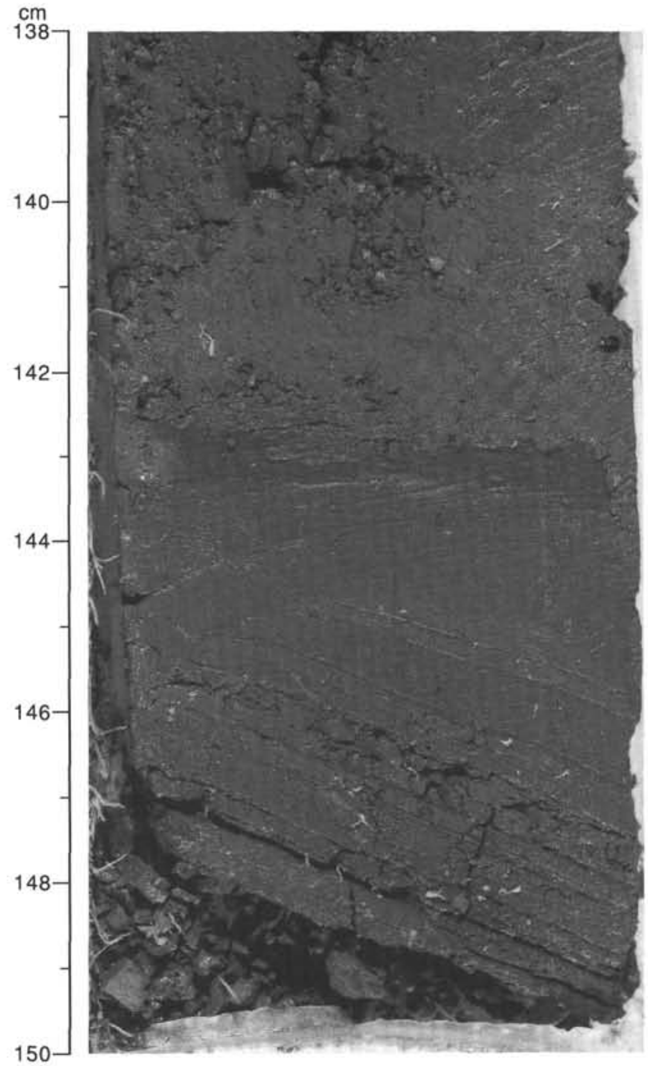

Figure 12. Core photograph of Section 141-862B-2X-1, with channel-fill of silty sand or sandy silt over a scoured base of moderately dipping, planar-laminated to thinly bedded silt.

extends only 5 cm or so above the basal contact of the sediment with the underlying basalt (Fig. 15). In Hole 862C, yellowish pigments appear, again in the short interval of sedimentary strata found in depositional contact with the fragment of glassy basalt in Section 141-862C-1W-1, at 32 cm. Thus, in all three holes distinctively pigmented sediment occurs in association with the observed or inferred contact zone of the marine sediments with the underlying volcanic rocks. These beds are informally referred to as the "ocher" beds in the discussions that follow. No yellowish or brownish pigments were seen elsewhere in Unit I.

At Hole 862A, the upper part of Subunit IC includes interbedded claystone and sandstone, overlying a lower matrix-supported conglomerate with very angular to very rounded pebble-size clasts. The conglomerate clasts range in size from 0.5 to 6 cm and include slightly consolidated claystones to silty claystones, sedimentary rocks, volcanogenic rocks, granodiorite, and black glass. This conglomerate is likely to represent the basal sedimentary lithology overlying the volcanic sequence.

Routine examination of the ocher beds recovered in Section 141-862C-1W-1 for microfossils yielded small concretions of copper sulfides (Fig. 16). In addition, an XRD-analysis of the

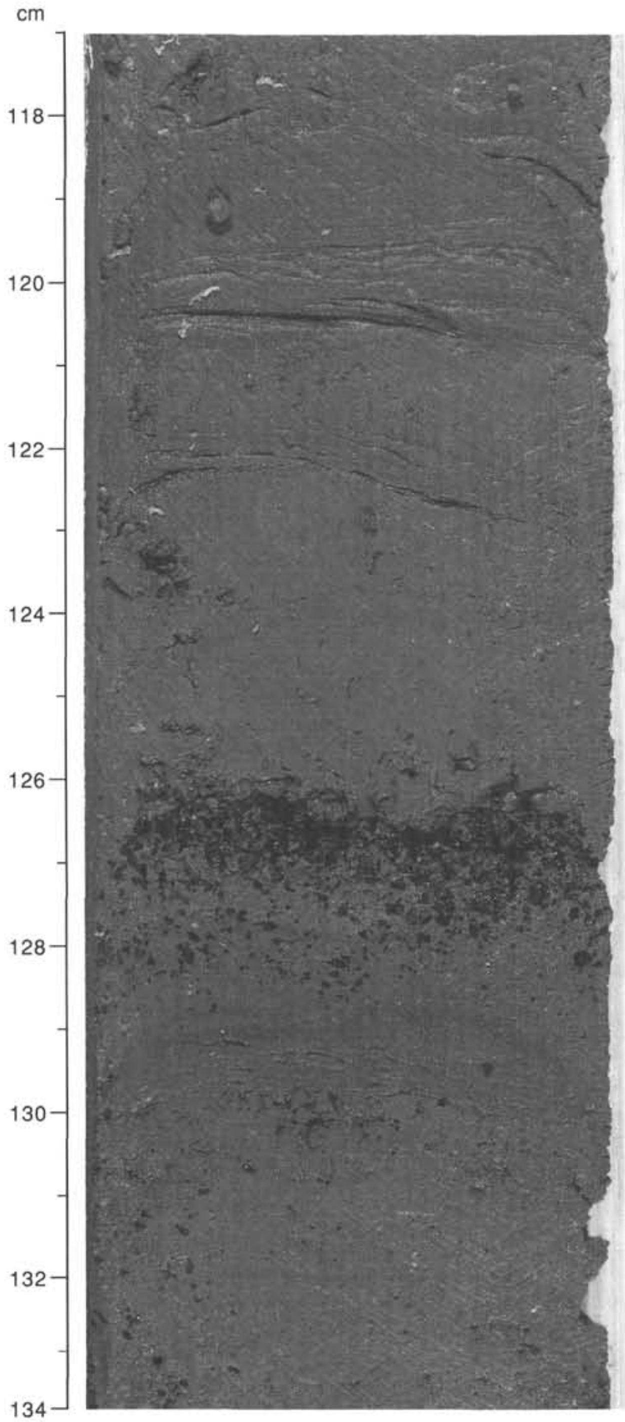

Figure 13. Core photograph of Section 141-862B-2X-2, 117–134 cm, within Subunit IB with a layer of black volcanic glass (tachylite). The angular clasts of black glass sit within a much finer, silty horizon. Glass horizons tend to have gradational bases, and more sharply defined tops. Thicknesses are typically 1–3 cm.

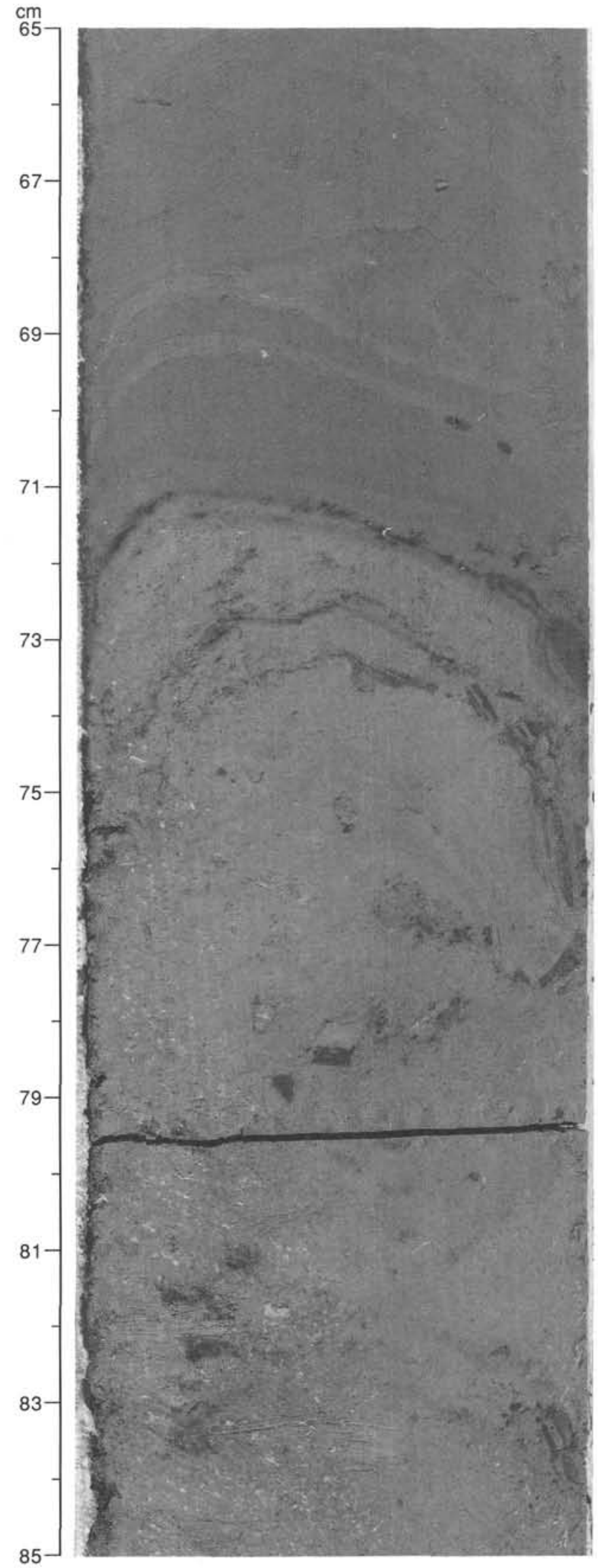

Figure 14. Core photograph of the top of brownish- to yellowish-gray silty clay beds that are found near the basal contact of Unit I with the volcanic subunits of Unit II.

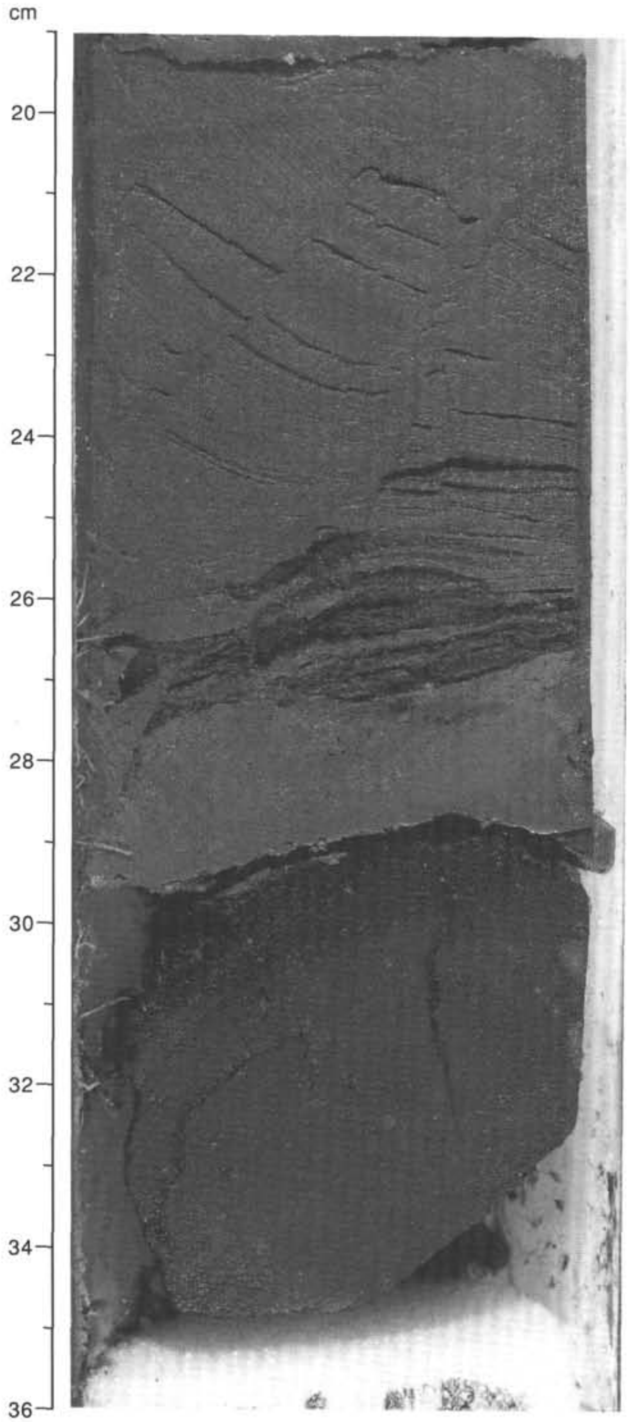

Figure 15. Core photograph of the contact of the marine sediments with the underlying glass rim of a basalt flow. The overlying "ocher" beds are enriched in copper sulfides and affected by arrays of normal faults.

clays in the transition from Subunit IB to Subunit IC was undertaken on board. The clays within the ocher beds, as well as within a presumed transition zone extending 0.5 m above them, show a major increase in the smectite/illite ratio compared to the ratio measured in the upper olive gray parts of Subunit IB. This change is consistent with a hydrothermally driven reaction of illite to smectite (see discussion of XRD results). Hydrothermal activity

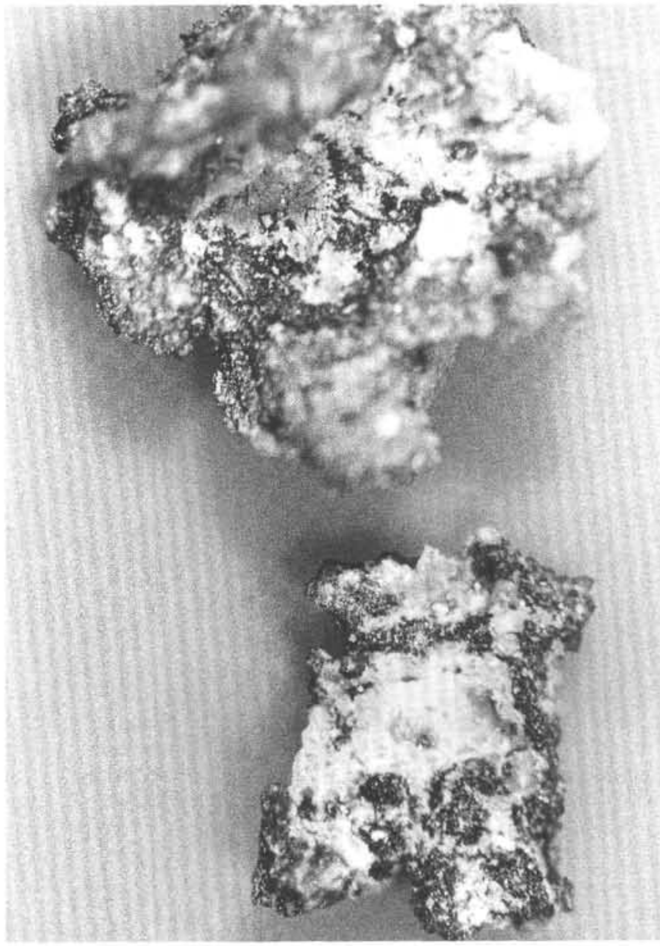

Figure 16. Photomicrograph of copper sulfate concretions from Core 141-862C-1W. Horizontal field of view is approximately 0.5 cm.

in the lower 4.25 m of the sedimentary sequence is also indicated by paleomagnetic evidence (see Paleomagnetism section, this chapter). The copper sulfides are believed to include (by visual identification) bornite, chalcopyrite, pyrite, and covellite. The first three of these are of hydrothermal origin, the last one is possibly a secondary replacement of one of the first three.

The basal matrix-supported conglomerate observed in Hole 862A contains the only layer with abundant volcanic glass within Subunit IC.

Unit II (from 35 cm in Section 141-862B-2X-CC through Core 141-862B-4X, from 37 cm in Section 141-862C-1W-1 through Core 141-862C-9B; age: late Pliocene; depth: 22.0–102.1 mbsf)

This unit is composed of the hard rock, dominantly volcanic, lithologies recovered under 22 mbsf. An indurated medium to coarse-grained calcareous metasandstone was found intercalated with the volcanic rocks in Section 141-862C-6R-1. Unit II is divided into subunits based on the observed changes in lithologies in each of the holes. Each of the holes also contained fragments of volcanic rocks in the upper few centimeters of the top cores, but these are not included as part of Unit II. Unit II hard rock lithologies are restricted to those rocks that were recovered stratigraphically beneath the ocher beds. The hard rock subunits of Unit II are further described in Igneous Petrology, below.

Mineralogic Compositions of Unit I Sediments

The shipboard analysis of the mineralogic composition of sediments is based on visual estimates of grain sizes and compositions obtained by inspection of the cores by hand lens and the microscopic studies of the smear slides that were prepared for representative lithologies in the cores. These visual estimates are verified, to a limited extent, by shipboard XRD analysis of selected horizons.

Smear Slides

Forty-four smear slides were made during the course of describing the dominant and minor lithologies present in Unit I. The variations of clay minerals to other detrital phases is shown in Figure 17. The variations in mafic minerals and glass are shown in Figure 18. Figure 17 shows that the sequence has two intervals of significant nonterrigenous mineralogy. The first is at a sub-bottom depth of approximately 2 m, the second at a sub-bottom depth of 17 to 20 m. The upper nonterrigenous layer is a nannofossil-rich zone at approximately 2.5 mbsf. Figure 18 shows that the lower zone of nondetrital sediment partly consists of glass. This zone corresponds to lapilli layers of black glass in Section 141-862B-2X-2. The clay fraction seen in Figure 17 also shows that the lower part of the hole, from approximately 15 to 22 mbsf, is increasingly clay-poor. However, a general upward-fining trend, discernable in the core descriptions (Cores 141-862A-1H, to -4H, see Visual Core Description section, this volume), is not clearly represented in the smear-slide database. Figure 18 also shows that the changes in the abundance of mafic minerals (including opaques, amphibole, accessory minerals, and pyroxene) have two interesting attributes. First, there is an apparent positive correlation between the abundances of volcanic glass and mafic minerals. Second, mafic minerals are generally much more abundant in the lower part of the sedimentary sequence. This increase largely reflects increases in the opaque phases, of which sulfides appear to be a significant part. There might be a relationship between the increased volcanic contributions and the presence of hydrothermal sulfides within these sediments. This conclusion is perhaps more valid for the basal zone where independent observations support the interpretation of increased abundance of copper sulfides.

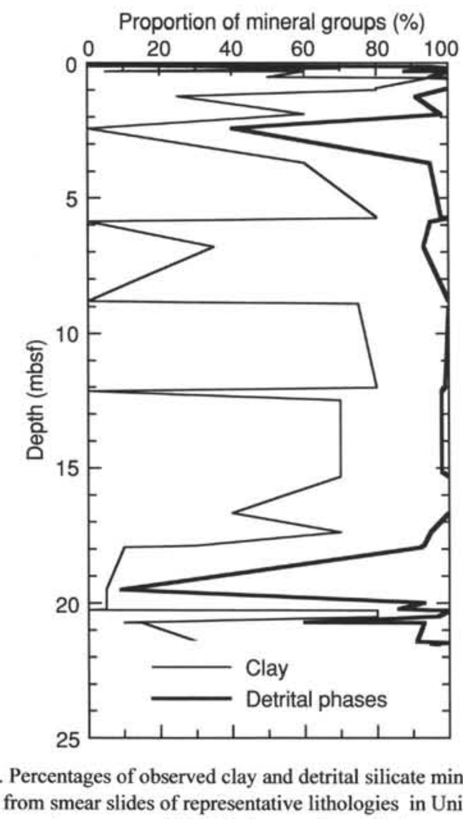

Figure 17. Percentages of observed clay and detrital silicate minerals visually estimated from smear slides of representative lithologies in Unit IA. A basal, clay-poor area is represented in this data, and two horizons of nondetrital lithologies appear at approximately 3 and 20 mbsf.

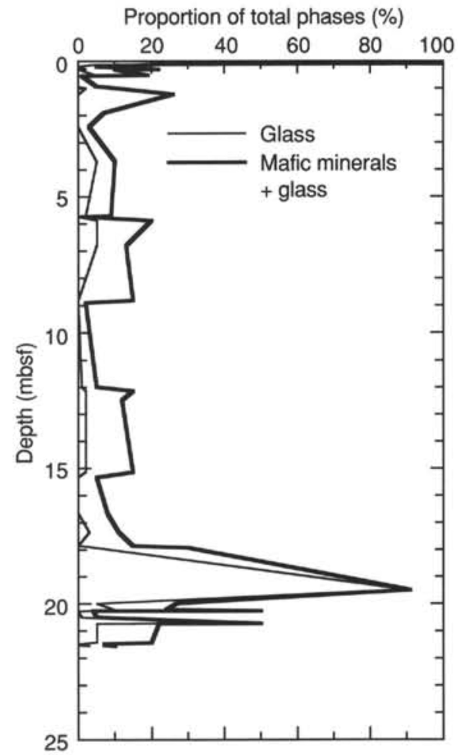

Figure 18. The percentages of mafic and opaque mineral phases and volcanic glass that were visually estimated from smear slides are shown. The percentage of mafic minerals (and opaques) is positively correlated to percentages of volcanic glass. The enrichment of opaques could be due to the generation of sulfide phases during effusive events.

XRD Analysis of Sediments

Six samples were selected from Hole 862A cores for X-ray diffraction analysis to better characterize the silt- and clay-size mineral phases. Bulk powders (three samples) and clay-size separates (three samples) were prepared using the *JOIDES Resolution's* Philips ADP 3520 X-ray diffractometer.

Bulk samples include the following:

141-862A-1H-3, 118–120 cm, gray sediment of Subunit IA;
141-862A-2H-3, 133–135 cm, gray sediment of Subunit IB; and
141-862A-3H-4, 97–99 cm, yellowish sediment of Subunit IC.

Based on the mineral composition of sediment analyzed from Hole 862A (Table 3), the dominant phase present in all of the bulk samples is quartz, and the secondary phase is feldspar. Hornblende is present in minor to trace amounts. An unidentified amorphous phase is also present in all samples. The clay minerals that appear to be present in

Table 3. Table of X-ray diffraction mineralogy of bulk sediments.

Core, section, interval (cm)	Depth (mbsf)	Nonclay mineral phases (100%)*				Phyllosilicates (100%)	
		Quartz	Feldspar	Hornbld.	Amorph.	Chlorite	Illite
141-862A-							
1H-3, 118–120	4.18	4	3	1	2	4	4
2H-3, 133–135	9.73	4	3	2	2	4	4
3H-4, 97–99	20.37	4	3	2	2	4	3

* Numbers indicate: 4. dominant, 3. secondary, 2. minor, and 1. trace phases.

these samples are chlorite and illite. These are present in roughly equal amounts, except in Sample 141-862A-3H-4, 97–99 cm, where illite is less abundant than chlorite. This sample possibly contains epidote (peak at 2.90Å).

Fine- fraction samples are as follows:

141-862A-1H-1, 114–116 cm, greenish-gray sediment, from Subunit IA;

141-862A-3H-4, 34–36 cm, gray sediment at base of Subunit IB, immediately above yellowish sediment of Subunit IC (transition zone?); and

141-862A-3H-4, 103–105 cm, yellowish sediment of Subunit IC.

Analysis of clay-mineral separates shows that the main part of the fine fraction removed from the bulk samples consists of illite, chlorite, smectite, and an admixture of quartz, feldspar, an amorphous phase, cristobalite, and amphibole-hornblende (Table 4).

The fine (clay) fraction from the greenish gray sediment of Subunit IA (Sample 141-862A-1H-1, 114–116 cm) contains a very small quantity of smectite (1%), much illite (71%), subordinate chlorite (28%) and a trace of quartz. Illite from this sample is a dioctachedral Fe-Al variety, a polytype modification of illite 2M1 (of muscovite type). The sample of the yellowish sediment of Subunit IC (141-862A-3H-4, 103–105 cm), and that of the gray sediment of Subunit IB (Sample 141-862A-3H-4, 34–36 cm) from the transition zone above Subunit IC are very similar in their mineralogies. These sediments contain smectite (18%–20%), illite (42%), and chlorite (38%–40%). Quartz and feldspar are approximately equal in amounts. Illite from the yellowish sediment, and from the gray transition zone, has an asymmetric peak at 10Å that disappears after saturation with ethylene glycol. Thus, this illite phase contains packets of a smectite-type clay mineral. It is very probable that the observed changes in smectite and illite abundances within Samples 141-862A-3H-4, 103–105 cm (yellowish sediment) and 141-862A-3H-4, 34–36 cm (gray sediment from transition zone) have a hydrothermal genesis.

Interpretation of Sedimentary Strata

Site 862 penetrated approximately 22 m of a sedimentary cover that overlies volcanic rocks. Except for black glass-rich layers and rock fragments enclosed in the uppermost sediments, the unit is nonvolcanic. The glass, however, by its nonvesicular character and coarse-sand to pebble sizes (in relation to hosting silts and clays), is of a "hydroclastic," or submarine pyroclastic, origin. The glass is similar to that recovered from the glass margins of the underlying volcanic fragments from Unit II. It most likely formed and was dispersed in a manner analogous to the violent spallation processes that operate on pillow flows as described by Fisher and Schmincke (1984). These spallation processes would disperse fragments only into sediment in close proximity to the vent. Thus, nearby active volcanic submarine eruptions must have persisted throughout the deposition of Unit I sediments to account for the ten observed glass-rich horizons.

The sediments are dominated by siliciclastic components. The exceptions are the volcanic glass-rich horizons, and the one hemipelagic horizon, mentioned earlier. Overall, these detrital terrigenous deposits are moderately (thinly to thickly) bedded, fine-grained deposits of clayey siltstone with subordinate clay and fine sand. Hemipelagic contributions to these deposits are more obvious in the upper part of the section.

The uppermost parts of the sequence (Subunit IA) contain graded intervals that are similar to the graded beds seen at Sites 859, 860, and 861. These intervals largely lack internal stratification, have very thin basal fine-sand layers, and are more microfossil-rich at their tops. They are interpreted to represent deposition from distal low-density turbidity currents and suspension fallout (see Lithostratigraphy section, Sites 859 and 860 chapters, this volume).

Hole 862A also contained numerous thin sandstone and sand layers with cross-laminated and scour-fill structures. Reactivation surfaces within the cross-laminated layers, the lack of surrounding graded intervals, and their thin and discrete occurrences would indicate, but not uniquely identify, these beds as contourites (Piper, 1978; Reading, 1978). Two mechanisms are available to generate the bottom currents required to form contourites. Along the west coast of South America, currents (e.g., the Humboldt Current) may have been forced to flow around, or over, a bathymetric obstruction like that of the Taitao Ridge. Resulting localized flow irregularities could then plausibly generate the 2 km/hr, or higher, currents thought necessary to form the migrating ripple or dune features that typify contourites. One could also postulate that volcanic eruptions may have generated displacements within the water column, or perhaps have produced thermally driven currents that could, in turn, also have produced the same bottom-current-related features.

Igneous Petrology

Coring at Site 862 recovered approximately 110 fragments of igneous rocks from all three holes. Hole 862A only contained two volcanic clasts at the top of the core, while Holes 862B and 862C recovered a series of igneous lithologies to sub-bottom depths of 42.9 and 102.1 m, respectively. The six pieces of igneous rocks recovered above the ocher beds (Subunit IC) are described below but are assigned to subunits of Unit I. The remaining hundred or so pieces of igneous rocks were recovered beneath Subunit IC from either Hole 862B or Hole 862C and are broken down into 20 subunits. Because correlation of units between holes is difficult, (due to the 100-m offset shown in Figure 5 and the poor recovery) a separate series of subunits has been established for each of the two holes. For this reason, and because of the possibility that core recovery in Unit II may not always have been in stratigraphic order (see below), the subunit division is informal.

In the description of these rocks, the approach was to first provide a visual assessment based on core descriptions with a hand lens. Subunits were defined at this stage without the aid of thin-section description or geochemical analysis. Thus, the boundaries between subunits reflect gross changes in the lithologic characteristics of rock fragments recovered in the cores. In most cases, however, boundaries placed between subunits are based on one of two criteria that we consider may reflect the appearance of a new in-situ geologic unit. These are either indications of a new cooling unit, (e.g., pieces with variolitic texture

Table 4. Table of X-ray diffraction mineralogy of sediment fines (<1 μm).

Core, section, interval (cm)	Depth (mbsf)	Smectite (%)	Illite (%)	Chlorite (%)	Cristobalite (%)	Amphibole (%)	Amorphous (%)	Quartz/Feldspar (rel. abundance)
141-862A-								
1H-1, 114–116	0.114	1	71	28	TR	TR	M	Qtz>>Feld
3H-4, 34–36	19.74	20	42	38	TR	TR	M	Qtz=Feld
3H-4, 103–105	20.43	18	42	40	TR	TR	M	Qtz=Feld

TR = trace amounts. M = minor amounts

under subophitic textures), or indications of a different composition (e.g., rhyolite under basalt). Wherever possible, rocks within a given systematic range of textures consistent with the variations expected in a single cooling unit were grouped into one subunit. Some of the fragments were small enough to become mixed within the core barrel, and thus some of the changes in texture or composition observed in these cores likely reflect this mixing. In addition, the low recovery suggests that the in-situ formations were intensely fractured and so may have become mixed to some extent prior to the individual pieces entering the core barrel. Thus, textural and compositional criteria used to define separate cooling units in the cores are likely to be wrong in detail.

Seven subunits were identified from the rock fragments recovered in Hole 862B, and 13 were identified from the fragments recovered from Hole 862C (Fig. 6). Rock fragments within each subunit are generally similar in composition and texture. The boundaries between the subunits mostly, but not invariably, reflect the existence of new cooling units or compositionally different flows. Due to the poor recovery over any given interval (1%–18%), the positions of subunit boundaries are only approximate. In both holes the changes in the subunits that were identified suggest in-situ variations of rock types over vertical intervals of about 2–6 m. These dimensions are reasonably consistent with those of pillowed flow units. Pillow breccias are also a possibility. However, there was no recovery of welded hyaloclastic fragments within Unit II, which are commonly found in association with pillow breccias. Thus, the recovered materials probably represent in-situ, but highly fractured, pillowed flow-units. None of the rocks contained holocrystalline textures, and all had at least some percentage of glassy to cryptocrystalline groundmass. In addition, none of the basaltic rocks had ophitic textures, which are commonly found within the centers of thick flow units, or dikes. Thus a thin, or pillowed, flow model is generally consistent with estimates of unit thicknesses and the observed textures.

Geochemistry of Site 862 Volcanic Rocks

In this section, XRF chemical data on 17 volcanic rocks recovered from Holes 862A, 862B, and 862C are presented. Duplicate runs were obtained for each sample. The 17 samples were chosen to be representative of the 20 subunits of Unit II, which forms the probable volcanic basement of the Taitao Ridge. The data are presented in Tables 5 and 6. Loss on ignition (LOI), expressed in weight percent, ranged from values generally less than 1% for the basaltic samples (SiO_2 wt% < 52%) and between 2.0% and 2.6% for the dacitic and rhyolitic samples. One sample (141-862C-1W, 56–61 cm) had an LOI of 6.22%, and is likely to have been influenced by the presence of secondary phases.

Overall, the geochemical data indicate that the silica contents of Unit II volcanic rocks are markedly bimodal. Of the 17 subunits analyzed, nine were basalts, four were dacites, and four were rhyolites. There is a marked gap from 52 to 66 wt% SiO_2. The basaltic samples, with SiO_2 values ranging from 48 to 52 wt%, have relatively high MgO contents (8.0–8.6 wt%) with K_2O values less than 0.5 wt%. Alkali contents suggest affinities to the tholeiites and subalkalic basalts. The basalts display positive correlations of Na_2O and K_2O with SiO_2 and negative correlations of CaO, Fe_2O_3, and MgO with SiO_2 (Fig. 19). The systematic variations observed in the chemical data suggest that the basaltic samples fall into two broadly-defined chemical groups representative of lavas related by relatively simple-crystal fractionation processes. Slight variations within each of these groups could easily represent variations in phenocryst percentages within the various samples. The rhyolites and dacites show a slight negative correlation of MgO, Fe_2O_3, and Al_2O with SiO_2, and positive correlation of K_2O and Na_2O with SiO_2. The chemical variations observed within the eight subunits of dacites and rhyolites suggest that two to four magma groups are represented.

BIOSTRATIGRAPHY

Introduction

The uppermost 1 m of Hole 862A contains mainly foraminifers and radiolarians; diatoms are insignificant and calcareous nannofossils are absent. Microfossils become rare below the top 1 m and therefore age determinations for the following downhole sequences were not possible on board the ship. However, shore-based investigations (C. Müller) of calcareous nannofossils gave additional age determinations.

Diatoms

All samples examined for diatoms at Site 862 were barren with the exception of Sample 141-862A-1H, 14–15 cm, in which a few specimens of *Coscinodiscus marginatus* and *Paralia sulcata* were observed. No age assessment is made based on these rare occurrences of non-age-diagnostic species.

Radiolarians

Abundant radiolarians are only found in the uppermost meter (Sample 141-862A-1H-1, 15–17 cm) of the sediments drilled at Site 862, below which is a barren zone extending to the base of lithologic Unit I (Fig. 20). No radiolarians were found in this zone, despite the examination of a further six samples in addition to regular core-catcher samples. A trace amount of radiolarians was also found in a metasedimentary layer encountered within the principally volcanic lithologic Unit II in Hole 862C (see below).

Sample 141-862A-1H-1, 15–17 cm, is placed in the *Anthocyrtidium angulare* (RN13) to *Buccinosphaera invaginata* (RN16) Zones of the Pleistocene to Holocene. This sample contains *Lamprocyrtis nigriniae* (one specimen) and *Theocorythium trachelium dianae* (two specimens) among more than 10 taxa, based on the analysis of three microslides. The assemblage includes a dozen tropical to subtropical fauna (e.g., *Heliodiscus asteriscus, Tetrapyle octacantha, Dictyocoryne profunda/Hymeniastrum euclidis*), indicating warm-water conditions.

In the same sample, 18 specimens of *Lamprocyrtis* cf. *heteroporos* are also found. The known range of *L. heteroporos* is from the top of the *Pterocanium prismatium* Zone (RN12) of the upper Pliocene to the *Stichocorys peregrina* Zone (RN11) of the lower Pliocene or possibly older (Sanfilippo et al., 1985). Several of them are nearly identical to illustration 3c (*L. heteroporos*) of Figure 29 in Sanfilippo et al. (1985), which initially prompted an age assignment (prior to the finding of the Quaternary taxa above) to the upper Pliocene. However, the following consideration casts a doubt on the Pliocene assignment. In an upper Pliocene sequence in the western equatorial Pacific (Kroenke et al., 1991) the author of this radiolarian section (K. Takahashi) saw specimens that were mostly similar to illustrations 3a and 3b (also *L. heteroporos*) of Figure 29 in Sanfilippo et al. (1985). This suggests that they are genuine forms of this species. Furthermore, all three specimens (a, b, c) illustrated by Sanfilippo et al. show a diameter of the abapical aperture of the terminal segment that is approximately equal to that of a lumbar-constriction between the second and third segments, and hence the terminal segment is cylindrical. At least several specimens in Sample 141-862A-1H-1, 15–17 cm, have an aperture diameter that is significantly greater than the lumbar constriction diameter, thus forming a conical third segment. For this morphological reason the population of this taxon is tentatively identified as *Lamprocyrtis* cf. *heteroporos* and distinguished from *L. heteroporos sensu stricto*. Although it cannot be totally dismissed, reworking is unlikely as such a relatively

Table 5. Major-element compositions of volcanic rocks from Site 862, Taitao Ridge, from shipboard X-ray fluorescence analysis.

Core, section, interval (cm)	Depth (mbsf)	Na_2O	MgO	MnO	TIO_2	K_2O	SIO_2	CaO	Fe_2O_3	Al_2O_3	P_2O_5	Total	LOI
141-862A-													
1H-1, 4–6	—	4.43	1.11	0.03	0.25	2.88	72.46	2.10	2.12	14.79	0.07	100.24	2.51
1H-1, 4–6	—	4.59	1.14	0.04	0.26	2.87	71.70	2.09	2.19	14.87	0.06	99.81	2.51
1H-1, 9–11	—	4.39	1.18	0.06	0.25	3.04	71.26	2.10	2.57	14.93	0.08	99.86	2.19
1H-1, 9–11	—	4.36	1.16	0.06	0.25	3.00	70.25	2.11	2.79	14.78	0.08	98.84	2.19
141-862B-													
1W-1, 7–10	—	4.63	1.12	0.04	0.24	2.89	71.40	2.07	2.12	14.89	0.07	99.47	2.35
1W-1, 7–10	—	4.55	1.14	0.04	0.26	2.86	70.57	2.06	2.19	14.68	0.07	98.42	2.35
1W-1, 33–40	—	4.79	1.54	0.04	0.44	2.36	69.47	2.95	3.00	15.61	0.10	100.30	1.43
1W-1, 33–40	—	4.65	1.51	0.04	0.43	2.32	68.28	2.91	3.08	15.41	0.07	98.70	1.43
3X-1, 95–100	28.05	2.80	8.42	0.13	0.99	0.13	49.40	11.80	8.70	16.75	0.07	99.19	0.14
3X-1, 95–100	28.05	2.69	8.31	0.13	0.98	0.13	48.99	11.71	8.71	16.58	0.07	98.30	0.14
4X-1, 8–18	36.58	4.56	1.10	0.04	0.24	2.96	71.26	2.03	2.18	14.71	0.07	99.15	2.27
4X-1, 8–18	36.58	4.61	1.11	0.04	0.25	2.95	71.38	2.05	2.20	14.78	0.07	99.44	2.27
4X-1, 21–28	36.71	3.18	8.08	0.12	1.14	0.55	51.43	9.87	8.34	16.38	0.13	99.22	0.90
4X-1, 21–28	36.71	3.16	8.02	0.12	1.13	0.55	51.76	9.84	8.25	16.27	0.13	99.23	0.90
4X-2, 124–130	38.4	3.14	8.45	0.13	1.14	0.55	51.39	9.76	8.43	16.17	0.12	99.28	0.96
4X-2, 124–130	38.4	3.28	8.41	0.12	1.14	0.56	51.23	9.70	8.43	16.02	0.13	99.02	0.96
141-862C-													
1W-1, 47–50	—	4.51	1.91	0.05	0.61	2.30	66.30	3.66	3.50	16.02	0.12	98.98	1.76
1W-1, 47–50	—	4.52	1.92	0.05	0.61	2.29	65.99	3.69	3.42	16.05	0.13	98.67	1.76
1W-1, 56–61	—	3.06	6.56	0.10	1.00	0.66	52.53	10.41	7.40	16.69	0.10	98.51	6.22
1W-1, 56–61	—	3.13	6.50	0.10	0.98	0.67	53.22	10.44	7.44	16.85	0.10	99.43	6.22
3R-1, 1–9	46.31	4.56	1.78	0.05	0.56	2.36	66.78	3.45	3.28	15.84	0.11	98.77	2.23
3R-1, 1–9	46.31	4.52	1.77	0.05	0.55	2.35	66.64	3.43	3.33	15.78	0.12	98.54	2.23
5R-1, 2–9	65.12	4.54	1.98	0.05	0.63	2.30	66.54	3.77	3.55	16.10	0.12	99.58	1.82
5R-1, 2–9	65.12	4.60	1.99	0.06	0.63	2.31	66.35	3.76	3.57	16.12	0.13	99.52	1.82
6R-1, 10–14	74.6	2.71	8.51	0.12	0.93	0.10	49.26	11.55	8.50	16.57	0.07	98.32	0.68
6R-1, 10–14	74.6	2.75	8.62	0.13	0.95	0.10	49.39	11.64	8.67	16.60	0.07	98.92	0.68
6R-1, 77–80	75.27	3.13	8.39	0.12	1.13	0.42	51.12	9.91	8.56	15.94	0.11	98.83	1.7
6R-1, 77–80	75.27	3.19	8.39	0.12	1.13	0.42	51.19	9.92	8.66	15.99	0.11	99.12	1.70
7R-1, 5–10	83.45	3.19	8.31	0.13	1.15	0.46	50.98	10.06	8.54	16.10	0.12	99.04	1.14
7R-1, 5–10	83.45	3.16	8.28	0.13	1.12	0.46	50.94	10.00	8.56	16.11	0.12	98.88	1.14
7R-1, 38–44	83.78	3.24	8.07	0.10	1.13	0.31	51.86	10.22	8.23	16.32	0.11	99.59	1.82
7R-1, 38–44	83.78	3.27	8.06	0.10	1.12	0.31	51.51	10.15	8.14	16.22	0.11	98.99	1.82
8R-1, 28–33	93.38	2.64	8.36	0.13	0.98	0.15	49.47	11.85	8.76	16.67	0.07	99.08	0.88
8R-1, 28–33	93.38	2.64	8.41	0.13	0.96	0.15	49.47	11.75	8.70	16.67	0.07	98.95	0.88

Table 6. Trace-element data for volcanic units of Site 862 from shipboard X-ray fluorescence analysis.

Core, section, interval (cm)	Depth (mbsf)	Nb	Zr	Y	Sr	Rb	Zn	Cu	Ni	Cr	V	TiO_2	Ce	Ba	A-Rh	A-Cr	A-V
141-862A-																	
1H-1, 4–6	0.04	7	188	19	115	104	22	6	0	0	22	0.31	37	416	10.29	111.86	142.97
1H-1, 9–11	0.09	7	186	19	118	102	24	9	4	0	26	0.32	36	407	10.56	112.08	143.20
141-862B-																	
1W-1, 7–10	0.07	7	186	19	113	103	24	9	0	1	16	0.30	37	414	10.13	110.06	140.69
1W-1, 33–40	0.33	7	188	20	144	52	22	4	3	3	42	0.49	34	386	10.73	113.18	143.54
4X-1, 8–18	36.58	7	179	18	107	100	21	7	0	3	19	0.29	34	394	9.83	107.15	136.98
4X-1, 21–28	36.71	3	102	26	136	9	54	50	185	327	192	1.21	10	56	14.01	123.79	152.61
4X-2, 124–130	38.40	3	103	27	134	10	53	52	205	355	198	1.24	13	62	14.30	126.01	155.28
141-862C-																	
1W-1, 56–61	0.56	3	96	25	130	12	48	56	206	380	194	1.10	15	75	14.11	128.64	159.61
3R-1, 1–9	46.31	7	184	21	157	82	29	20	3	5	58	0.58	31	356	10.92	113.89	143.83
5R-1, 2–9	65.12	7	179	21	165	76	31	14	6	5	67	0.64	30	333	11.00	113.94	143.57
6R-1, 10–14	74.60	1	58	24	89	2	51	69	199	387	205	1.09	5	7	14.68	129.49	160.77
6R-1, 77–84	75.27	3	96	27	128	6	52	53	208	351	194	1.21	11	33	14.01	123.08	151.69
7R-1, 5–10	83.45	3	95	27	126	7	52	53	197	351	203	1.22	13	42	14.03	123.39	152.06
7R-1, 38–44	83.78	3	95	26	133	4	50	52	202	342	199	1.20	9	43	13.79	122.48	151.00
8R-1, 28–33	93.38	1	58	24	89	3	53	69	182	382	213	1.09	4	0	14.67	128.59	159.65

large number of specimens with respect to the other radiolarian species are found. Foraminifer age (see below) conforms with the above Pleistocene assignment.

Sample 141-862C-6R-1, 37–39 cm, is a thin layer of lithified meta-sedimentary rock intercalated between volcanic rocks above and below. This sample contains several specimens of non-age-diagnostic radiolarians, indicating that the sedimentation occurred in a marine environment.

Planktonic foraminifers

Planktonic foraminifers are abundant and well preserved in the uppermost 25 cm of Hole 862A (Table 7). The soft green clay contains a subtropical assemblage of planktonic foraminifers in Samples 141-862A-1H-1, 14–15 cm, and 18–24 cm. *Beella digitata, Orbulina universa, Globigerina cariacoensis, Neogloboquadrina dutertrei* and *Truncorotalia truncatulinoides* are encountered. Below this interval down to Sample 141-862A-1H, 101–104 cm, rare abundances of *T. truncatulinoides* indicate a Pleistocene age. The absence of the above-mentioned subtropical taxa and the additional occurrence of *Globorotalia hirsuta, Globoconella inflata,* and *Neogloboquadrina pachyderma* in its dextral coiling direction indicate temperate paleotemperatures. Sample 141-862A-1H-CC contains rare specimens indicative for the Holocene to Pliocene of the Transitional Zone. Below this sample the sediments are mostly barren. Only in two samples of Core 141-862A-3H are small amounts of stratigraphically longer-rang-

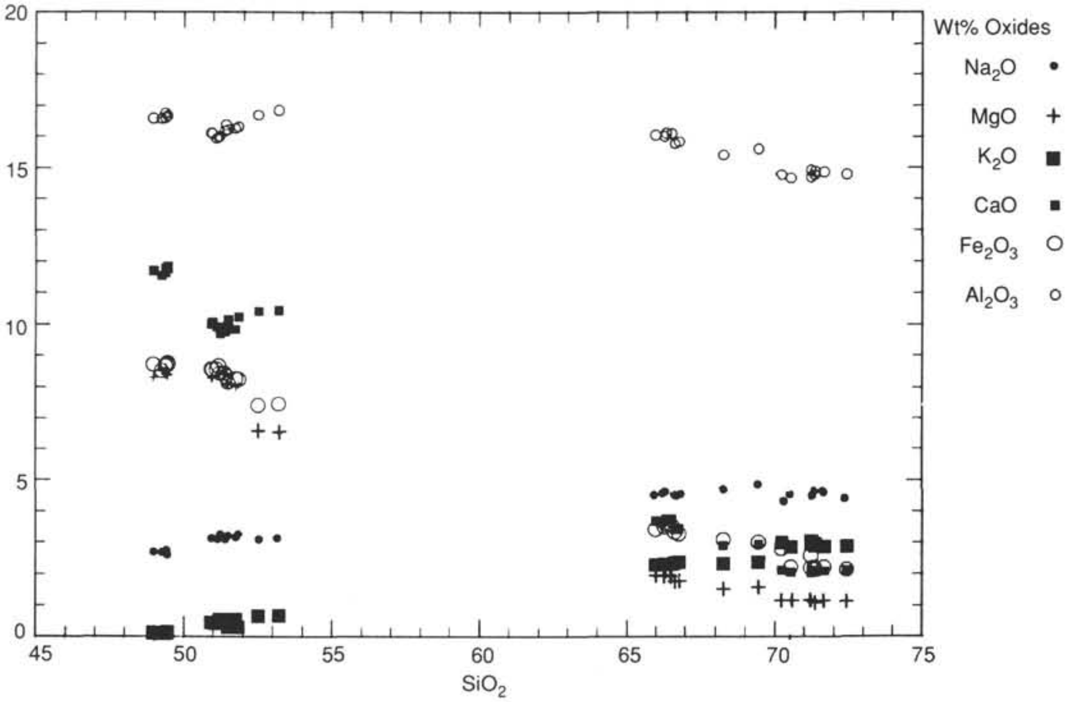

Figure 19. Harker variation diagram for Taitao Ridge volcanic rocks.

ing taxa observed. The occurrence of *N. pachyderma* sinestral in Samples 141-862A-3H-CC and 141-862C-2X-CC indicates cold paleoenvironments of Pleistocene to Pliocene age. Sample 141-862C-6R-1, 37–39 cm, which is lithified and required crushing for analysis, contains fragments of calcareous shells; the thin-section shows traces of *Quinqueloculina* sp. and sea-urchin spines, indicating a marine source for this layer (see Lithostratigraphy section, this chapter) within the upper part of the basaltic sequence in Hole 862C.

Benthic foraminifers

Benthic foraminifers are well represented in Hole 862A down to Sample 141-862A-1H-1, 18–24 cm. Below this sample they become rare in Hole 862A as well as in the observed samples from Holes 862B and 862C (Table 8). The Holocene depth distribution of these taxa indicates a lower to middle bathyal environment (van Morkhoven et al., 1986). *Rupertina stabilis,* observed in Samples 141-862A-1H, 14–15 cm, and 18–24 cm, is a world-wide distributed cold-water species, a sediment-feeder with special adaptions to flowing nutrient-carrying waters, distributed from the upper continental slope down to bathyal depths (Lutze and Altenbach, 1988).

Calcareous nannofossils

Twenty-two samples from Hole 862A were studied for calcareous nannoplankton, which are extremely rare. Core 141-862A-1H and Core 141-862A-2H are barren of autochthonous nannofossils. Only rare reworked species from older strata (Oligocene-lower Miocene) have been found. Sample 141-862A-3H-CC belongs most probably to the upper Pliocene (Zones NN16–NN18). Nannofossils are few, with the following species present: *Syracosphaera pulchra, Coccolithus pelagicus, Helicospharetra carteri, Cyclococcolithus leptoporus, C. macintyrei* (very rare), *Pseudoemiliania lacunosa,* and very small specimens of *Gephyrocapsa* sp. Core 141-862A-4H is barren of nannoplankton.

PALEOMAGNETISM

Introduction

Magnetic remanence measurements using the pass-through cryogenic magnetometer were made on archive-halves of the three APC cores from Hole 862A, representing the sediment sequence of lithologic Unit I (see Lithostratigraphy section, this chapter). Alternating field demagnetization (AF) on these sections was performed at 9, 12, and 15 mT, so that the direction of the characteristic remanent magnetization (ChRM) could be separated from the viscous remanence (VRM) and any other overprints present. Measurements were performed at intervals of 10 cm. Measurement of discrete specimens provided information about igneous material from Holes 862B and 862C, where pass-through magnetometer measurements were not performed. Magnetic susceptibility measurements on the multisensor track (MST) were performed routinely on whole-round sections.

Remanence and Susceptibility–Continuous Sediment Sections

Figure 21 shows the proportion of NRM remaining after 15-mT demagnetization for the sediment sequence of Hole 862A. Core 141-862A-2H (5.4–14.9 mbsf) has a consistently higher proportion of the original magnetization remaining after demagnetization than the cores above and below it. Patterns of more and less intense drilling-related overprinting alternating from core to core have been observed during previous legs and have been interpreted as resulting from the alternate use of a pair of core barrels, one strongly magnetized and the other more weakly magnetized (D. Schneider, pers. comm., 1992). Overprinting in Core 141-862A-2H was apparently less intense than in the cores above and below it, so that the low-coercivity component removed by 15-mT demagnetization made up a smaller proportion of the NRM in this core.

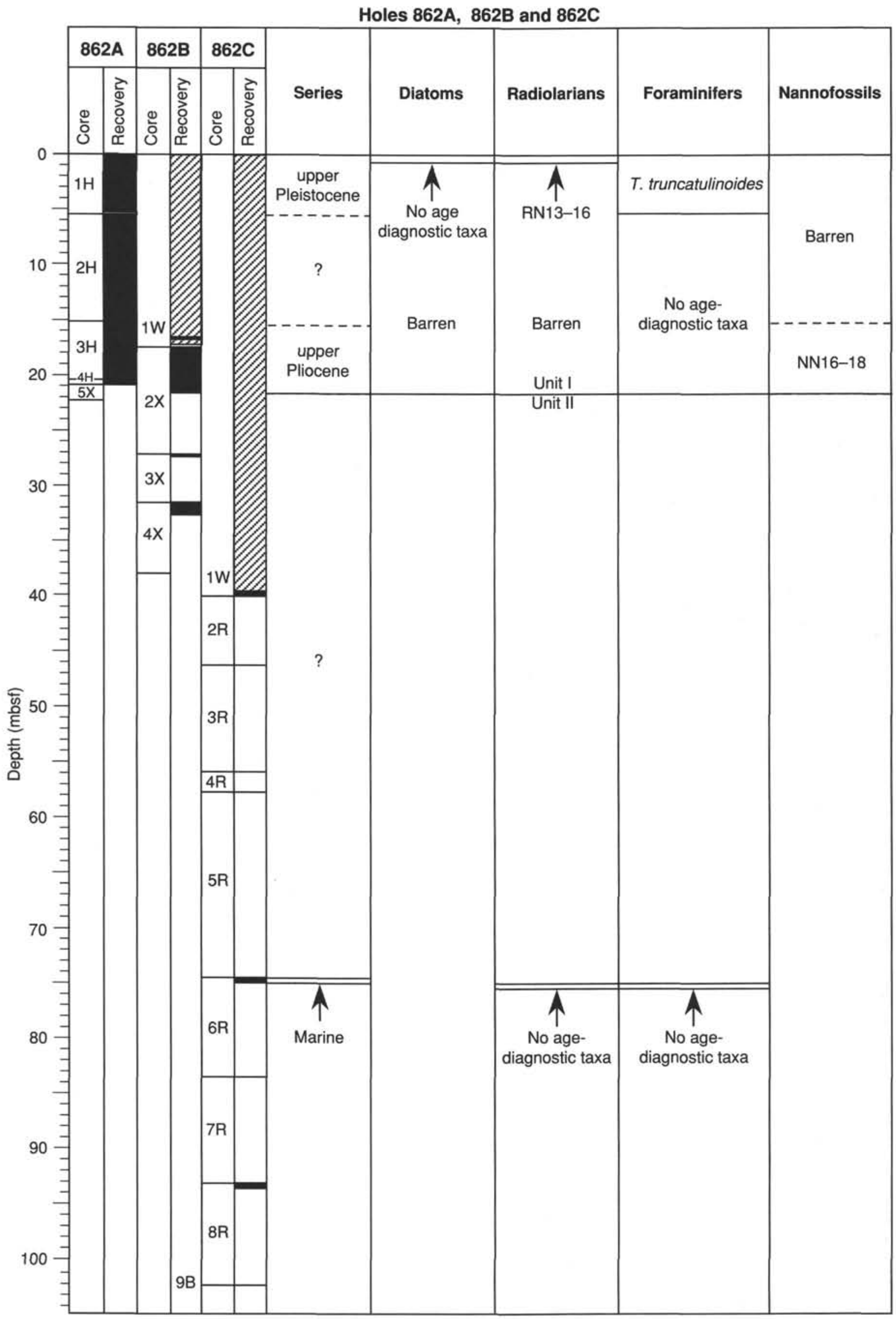

Figure 20. Summary of biostratigraphic age for the sediments recovered at Site 862.

The susceptibility record (Fig. 21) also shows a change between Cores 141-862A-1H and -2H, but this change is more gradational, and probably represents the lithologic variation from lithologic Subunit IA to IB, which occurs at about 6–7 mbsf. Susceptibility decreases sharply below 20 mbsf, corresponding to the alteration zone at the base of lithologic Unit I. Hydrothermal alteration has evidently removed or replaced about half of the magnetite in this zone.

The effects of core-barrel overprinting are also visible in the NRM inclination record (Fig. 22). Inclination over the interval of Core 141-862A-2H is about 5° shallower than in Cores 141-862A-1H and -3H, as a result of a weaker steeply inclined core-barrel component. Demagnetization increases the inclination contrast between Cores 141-862-2H and -3H, but the inclinations of Core 141-862A-1H and -2H are similar after demagnetization. Inclinations in the alteration zone at the bottom of Core 141-862A-3H remain steeply negative.

Demagnetized inclinations in Core 141-862A-2H average about –30°. The expected inclination of a primary magnetization at this latitude is ±65°, and recorded dips in this core average 17°. Hence, the demagnetized remanence in this core does not record the primary inclination, as removal of the observed bedding tilt cannot restore the observed inclination to either a normal or reversed magnetization. However, the demagnetized inclination record can be explained either as (1) the sum of a reversed primary magnetization and unremoved VRM plus or minus a core-barrel overprint or (2) a normal polarity primary magnetization that has suffered considerable inclination shallowing during sedimentation (King, 1955; Verosub, 1977) or sediment compaction (Anson and Kodama, 1987; Arason and Levi, 1990; Deamer and Kodama, 1990; Levi and Banerjee, 1990). Demagnetized inclinations in Core 141-862A-1H fall into two groups: those above 3 mbsf average around –20° to –30°, those below 3 mbsf average between –30° and –40°. Whether this division relates to differences in the extent of overprinting or to some other cause is not clear. Demagnetized inclinations over most of Core 141-862A-3H average around –50°. These could represent primary normal magnetizations, as dips in this core average about 34°. However, these inclinations could also result from more extensive normal overprinting of a reversed primary magnetization, an interpretation consistent with the demagnetization of discrete samples from this core (see below). The very steeply negative demagnetized inclinations in the alteration zone below 19.5 mbsf (lithologic Subunit IC) may imply the presence of an additional (hydrothermal?) overprint, or an increased sensitivity to acquisition of the drilling-induced overprint. Magnetic-sulfide-bearing sediments from ODP Leg 130 carry high-coercivity drilling-induced remanences (Musgrave et al., in press). Although the magnetic sulfide in the Leg 130 sediments was biogenic in origin (probably greigite), pyrrhotite may well behave in a similar fashion. Pyrrhotite has not been directly observed in lithologic Subunit IC samples, but it may accompany other sulfides observed in the hydrothermal alteration zone (see Lithostratigraphy section, this chapter).

Demagnetization of Discrete Sediment Samples

Demagnetization of discrete samples from Cores 141-862A-1H and -2H (Fig. 23) indicates that the inclinations after 15-mT demagnetization remain unchanged during further demagnetization to 50–70 mT. This suggests that the overprint has been completely removed, unless the overprint and primary magnetizations have similar AF-stability spectra. A simpler explanation may be that the primary magnetization is normally polarized, but its inclination has been shallowed. Little compaction would be expected in such a thin sequence, so any inclination shallowing that may be present must have occurred during deposition. Whichever explanation is correct, structural orientation with reference to the characteristic magnetization determined by AF-demagnetization will be misleading.

Discrete samples from Core 141-862A-3H (Fig. 24) display far more complex demagnetization paths, with evidence for multiple overprints of differing polarity. Some of these overprint components may have been acquired as partial thermoremanences during the hydrothermal activity that produced the alteration of the lower part of this core. Hydrothermal activity evidently persisted at least until after deposition of Sample 141-862A-3H-2, 134–136 cm, which is 4.25 m above the top of the igneous unit. Clay mineralogy (see Lithostratigraphy section, this chapter) and the presence of gasoline-range hydrocarbons (see Organic Geochemistry section, this chapter) also indicate continuing hydrothermal activity during deposition of the sedimentary sequence. The polarity of

Table 7. Occurrence, preservation, and estimated relative abundance of planktonic foraminifers in samples from Holes 862A through 862C.

Sample	Depth (mbsf)	Abundance	Preservation	*T. truncatulinoides*	*G. bulloides*	*G. cariacoensis*	*G. inflata*	*G. scitula*	*B. digitata*	*O. universa*	*N. pachyderma* D	*N. dutertrei*	*G. hirsuta*	*N. pachyderma* S	*G. crassaformis*	*G. crassula*	Paleotemperatures	Zone
141-862A																		
-1H-1, 14 cm	0.14	C	G	F	C	F	R	R	R	R	R	R					Subtropical	*Truncorotalia truncatulinoides*
-1H-1, 18 cm	0.18	C	G	R	R	C	F	R		F								
-1H-1, 62 cm	O.62	R	P	R	R			R			R						Warm to temperate	
-1H-1, 88 cm	0.88	R	P	R														
-1H-1, 101 cm	1.01	R	P	R	R		R				R		R					
-1H-CC	5.40	R	P		R		R				R						Cold to temperate	No age-diagnostic taxa
-2H-CC	14.90	B																
-3H-1, 38 cm	15.28	R	P								R							
-3H-4, 48 cm	19.88	B																
-3H-4, 85 cm	20.25	B																
-3H-4, 106 cm	20.46	B																
-3H-CC	20.60	R	P											C	R			
-4H-CC	21.10	B																
141-862B																		
-2X-CC	27.1	R	P											R			Cold	?
141-862C																		
-1W-1, 10 cm		R	P		R										R	R	Temperate	?
-1W-1, 32 cm		R	P	R											R			
-6R-1, 37 cm	83.77	B															—	—

Table 8. Occurrence, preservation, and estimated relative abundance of selected benthic foraminifers in samples from Holes 862A through 862C.

Sample	Depth (mbsf)	Abundance	Preservation	*Uvigerina peregrina*	*Planulina wuellerstorfi*	*Cibicidoides refulgens*	*Bulimina mexicana*	*Rupertina stabilis*	*Uvigerina proboscidea*	*Bulimina exilis*	*Melonis pompilioides*	Paleoenvironments
141-862A												
-1H-1, 14 cm	0.14	F	G	F	R	R	R	R				
-1H-1, 18 cm	0.18	F	G	R	R	R	R		R			
-1H-1, 62 cm	0.62	R	P		R				R			
-1H-1, 88 cm	0.88	R	P									
-1H-1, 101 cm	1.01	R	P									← Lower to middle bathyal →
-1H-CC	5.40	R	P									
-2H-CC	14.90	R	P									
-3H-1, 38 cm	15.28	B										
-3H-2, 60 cm	17.00	R	P									
-3H-4, 48 cm	19.88	B										
-3H-4, 85 cm	20.25	R	P	R								
-3H-4, 106 cm	20.46	B										
-3H-CC	20.60	B		R								
-4H-CC	21.10	B										
141-862B												
-2X-CC	27.1	R	P				R					
141-862C												
-1W-1, 10 cm		R	P	F							R	
-1W-1, 32 cm		R	P	F	R		R					
-6R-1, 37 cm	83.77	B										

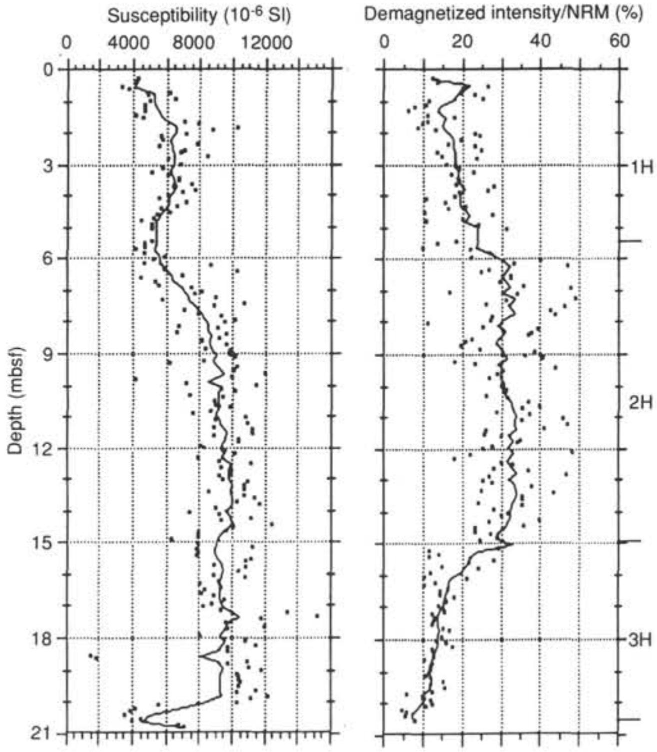

Figure 21. Magnetic susceptibility, and the ratio of intensity after 15-mT demagnetization to NRM, vs. sub-bottom depth for Hole 862A. Intervals spanned by each core are indicated on the right.

the primary magnetization in these samples is unclear. Sample 141-862A-3H-3, 91–93 cm, displays a long demagnetization trend to very low negative inclinations, implying that the primary magnetization has not been isolated even at the highest AF level applied (40 mT). In turn, this suggests that the primary magnetization in this core may be reversed. As in the upper two cores from this hole, structural orientation from the characteristic magnetization determined by AF demagnetization is not possible in this core because of the failure to clearly isolate the primary magnetization.

Summary of Sediment Magnetization

The sediments have been overprinted, both by VRM and by a core-barrel magnetization, which was stronger in Core 141-862A-2H than in the other two cores. Primary magnetization polarity is difficult to determine; it may be reversed in Core 141-862A-3H, but the primary magnetization of the upper two cores appears to be normal, in which case severe inclination shallowing has occurred. Multiple overprints have been acquired by the sediments in Core 141-862A-3H, some of which are probably partial thermal remanences due to hydrothermal activity.

Discrete Igneous Samples

In Table 9 we compare NRM intensity and median destructive field (MDF) of 11 samples of igneous rocks from Holes 862B and 862C, divided into two categories: plagioclase-pyroxene-olivine-phyric basalts and rhyolites/dacites. Coercivities of the basalts are generally higher than those of the rhyolites and dacites, although the spread is broad.

STRUCTURAL GEOLOGY

Summary

At Site 862 two holes, 862A and 862B, yielded detailed structural sections through the thin sedimentary cover of the Taitao Ridge. No structures were observed in the underlying basement/basement talus. The structure of the sediments is dominated by a set of steep normal faults, associated changes in the dip of bedding, and the development of intraformational breccias.

Hole 862A has an apparent 100% recovery without significant drilling disturbance to 21.1 mbsf, and can be subdivided into four related structural domains. Between 0.3 and 14.9 mbsf is a domain dominated by normal faults with shallow to moderately dipping bedding and development of breccia in clay lithologies. The first major normal fault is observed at 2 mbsf. Clay breccias are the major lithology between 14.9 and 18.78 mbsf. These are interlayered with sands in a domain having no normal faults. Between 18.78 and 19.7 mbsf, normal faults are common and bedding dips steeply. The normal faults flatten to a detachment at 19.7 mbsf above a domain 20 to 80 cm thick of normally faulted, flat-bedded sediments overlying the basement interface. Much of the basement material is rubbly and may represent talus overlying basement; evidence for penetration of in-situ basement is discussed in the Igneous Petrology section, this chapter.

Hole 862B is sited 10 m southeast of Hole 862A and the mudline in Hole 862B is 6.5 m above that in Hole 862A. Deformed sediments were recovered from 17.5 mbsf to the basement interface at 21.5 mbsf. Material similar to the brecciated domain in Hole 862A was recovered between 17.5 and 21.2 mbsf that overlies a thin flat-bedded domain immediately above the basement interface.

Detailed structural data for Holes 862A and 862B are presented in Table 10. Bedding and fault orientations are plotted on stereonets in Figure 25. Neither multishot nor Tensor data are available for Hole 862A, so rotation of data into the geographical reference frame has not yet been possible. However, normal faults have a consistent orientation in Core 141-862A-2H and an equally consistent orientation in Core 141-862A-3H. Thus, the data for these two cores can be rotated into the same reference frame by

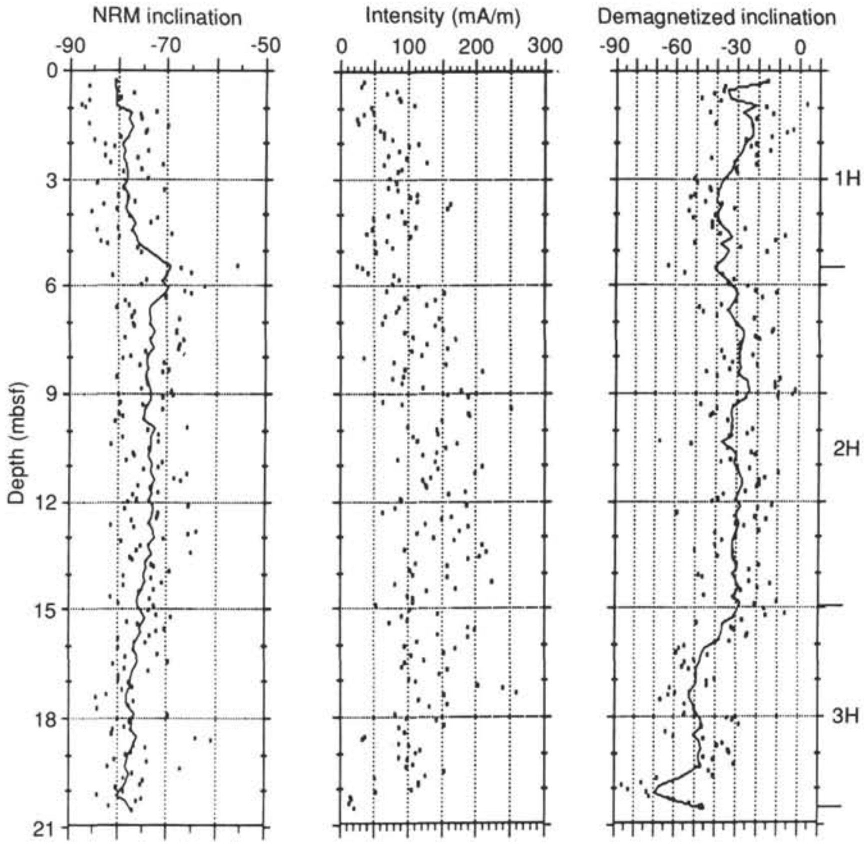

Figure 22. NRM inclination and intensity, and inclination after 15 mT demagnetization, vs. sub-bottom depth for Hole 862A. Cored intervals are indicated on the right.

assuming that the mean orientation of the dominant set of normal faults in each of the two cores is the same. The best-fit great circle to the poles to normal faults in Core 141-862A-2H has a strike of 252° in the core reference frame. The best-fit great circle to the poles to normal faults in Core 141-862A-3H has a strike of 079° in the core reference frame. Bedding and normal fault data from Core 141-862A-3H have been rotated 173° counterclockwise, around a vertical axis, to bring them into the reference frame of Core 141-862A-2H (Fig. 25). The only measurement of the orientation of a major normal fault in Core 141-862A-1H has a strike within 9° of the mean strike of normal faults in Core 141-862A-2H. Bedding data from Core 141-862A-1H thus are included in these plots without rotation. The poles to rotated bedding have a good great-circle distribution, with a bedding plane intersection of 02° toward 194° in the reference frame of Core 141-862A-2H. The poles to rotated normal faults have a moderate great-circle distribution with a fault intersection of 17° toward 162° in the reference frame of Core 141-862A-2H.

Upper Normal-Fault Domain

This domain underlies 30 cm of poorly consolidated sediment and is represented in Sections 141-862A-1H-1, 30 cm, through -2H-CC (0.3-14.9 mbsf). The highest significant normal fault is observed at 2.0 mbsf. This domain is best exposed in Core 141-862A-2H. The strike of both bedding and normal faults is approximately N-S (in the core reference frame of Core 141-862A-2H), and observed apparent dips approximate to true dips. The majority of faults dip 50°–75° to the east (Fig. 26). A few faults with a conjugate orientation dip 50°–80° to the west (Fig. 27). Exposed fault lengths vary from a few millimeters to 15 cm (the latter are faults that extend to the core liner on both the east and west sides). In all but three faults, separations are normal where they could be established. Normal separations vary between 1 mm and > 15 cm. The three observed reverse separations are less than 3 mm. Single faults and nested arrays in which branching occurs are both observed. Faults appear as fine dark lines, sometimes attaining a thickness of 0.5 mm. One set of normal faults is cut by a shallow-angle fault with unknown separation (Fig. 26).

Bedding dips 0°–40°, generally to the west. Where steep dips are observed they are commonly in the hanging wall of a normal fault. The zone of faulting is associated with intraformational breccias a few centimeters to 35 cm thick. Breccias form in clayey lithologies and comprise angular fragments of that lithology from submillimeter to 20 mm in size. Breccias are typically developed in the hanging-wall regions of arrays of normal faults. Some normal faults offset breccia (Fig. 28), whereas others detach in breccia zones. Faults are not observed in the majority of breccias. Many breccias have sharp upper contacts with sand. The fractures defining breccia clasts are sub-perpendicular to and abut against the sand contact (Fig. 28).

Sand layers that undoubtedly represent sediment layers are well laminated. Veins of structureless sand, 1–5 cm thick with sharp margins, have intruded into the sediments (Fig. 11). Some normal faults detach in 2-to 5-cm-thick structureless sand layers that do not have intrusive contacts with sedimentary layers.

Section 141-862-2H-4, 50–114 cm (Figs. 29 and 30), illustrates many of the structures, observed in isolation elsewhere, in a coherent section where inter-relationships are clearer. In the discussion below, letters cross reference to features highlighted in Figure 30, and all directional references are in the core reference frame. At the base of this interval is a 2- to 3-cm structureless sand unit. The upper contact of the sand (A) is cut by normal faults

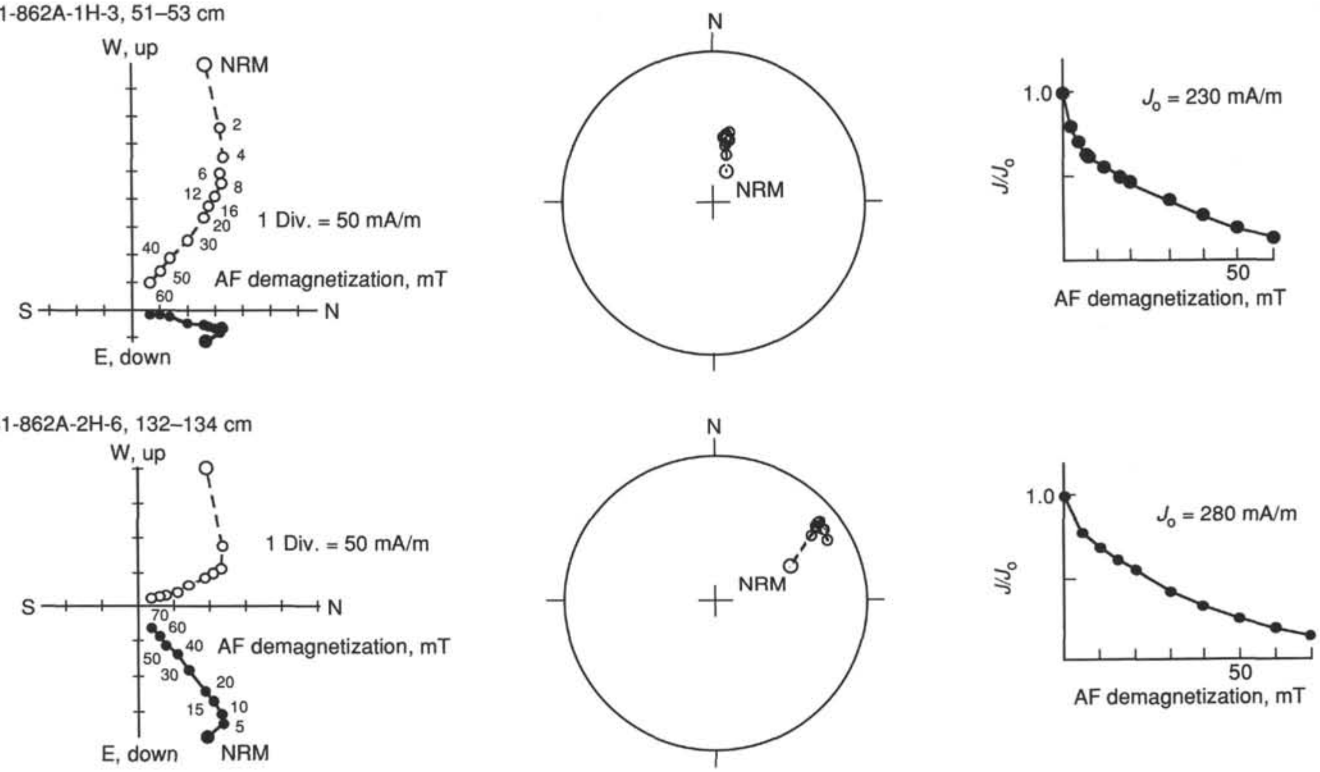

Figure 23. AF demagnetization of discrete sediment samples from Cores 141-862A-1H and -2H. Zijderveld plots: open symbols on vertical plane. Stereonet: open symbols are in upper hemisphere.

that do not penetrate the lower contact. The faults have separations of 1 to 7 mm and the separation in the easternmost normal fault (B) must be greater than 9 cm (the length of fault observed) because it juxtaposes two different lithologies (bedded and unbedded clays). The hanging-wall lithology is bedded. Bedding surfaces are flat-lying and have an irregular morphology on a submillimeter scale. Some bedding surfaces are more planar and are defined by 0.5-mm-thick dark lines with locally thicker segments (C). The easternmost normal fault is offset along these bedding surfaces, with top-to-the-west separations of 1 to 8 mm (D). The bedding surfaces are shallowly west-dipping adjacent to the easternmost fault and shallowly east-dipping next to the core liner. Three to four centimeters east of the fault is the start of a transitional boundary from bedded material to intraformational breccia (E). At the boundary, bedding planes are still observed, together with fractures in many orientations. Five to ten millimeters farther to the east the bedding surfaces are lost, and a breccia comprising submillimeter to 10-mm-sized angular fragments is observed. Ten to twenty millimeters farther east, the breccia is entirely fine-grained. The fine breccia has sharp upper/easterly normal fault contacts (F) with coarser breccia overlain by finer breccia and thin, finely laminated sands that dip shallowly to the west. Fine breccia is also present as interlayers between sandy laminations (G). The clay-sand contact is not repeated west of fault F, which must have more than 5 cm separation. Clay overlies the fine sands and this contact is cut by an array of normal faults that persist for 15 cm up the core. Above this, a coarse breccia has a sharp contact against a normal fault and continues with 1-cm thickness along this fault (H). The breccia is inhomogeneous. In the west, the breccia comprises submillimeter to 15-mm angular clasts. Overall these fine to the east, where all clasts are submillimeter in size. The breccia has a sharp, irregular contact with sand (I). The contact dips steeply to the east. Bedding laminations in the sand dip less steeply to the east and are truncated at the contact. The lowermost bedding lamination (J) is truncated both to the east and the west. Bedding within the sand flattens off upward over 10 to 15 cm, corresponding to a fining upward to clayey silt.

The contact of the upper normal-fault domain with the breccia domain lies between Cores 141-862A-2H and -3H. Given the imprecision in measurement of core advance, it is possible that the contact of the upper normal-fault and breccia domains was not recovered.

Breccia Domain

In Hole 862A exposure of this domain is restricted to Core 141-862A-3H. All orientations are quoted in the reference frame of Core 141-862A-3H. The strike of both bedding and normal faults is approximately north-south (in the core reference frame) and observed apparent dips approximate to true dips. Sections 141-862A-3H-1 through -3H-3, 88 cm, are characterized by interlayers of angular intraformational breccia and sand. Bedding dips moderately to the east. Sixty to seventy percent of this domain is breccia in units of 20 to 40 cm thick. Breccias are developed in silty clay layers and comprise submillimeter to 30-mm angular clasts. The base of the domain is a transition, over an interval of 11 cm, from well-bedded clay up into breccia (Section 141-862A-3H-3, 80 90 cm). Poorly preserved bedding is observed in some of the breccias, more so toward the base of this domain. Some clays form the upper part of fining-upward sequences. In these instances brecciation becomes better developed in the finer sediment.

Sand horizons 1 to 30 cm thick separate the clay breccias. Many of the sands have good bedding laminations and grade upward. In Section 141-862A-3H-2, 77 107 cm, detachments can be identified in the base of a thick laminated sand (Fig. 9). No unambiguous overall sense of displacement can be established.

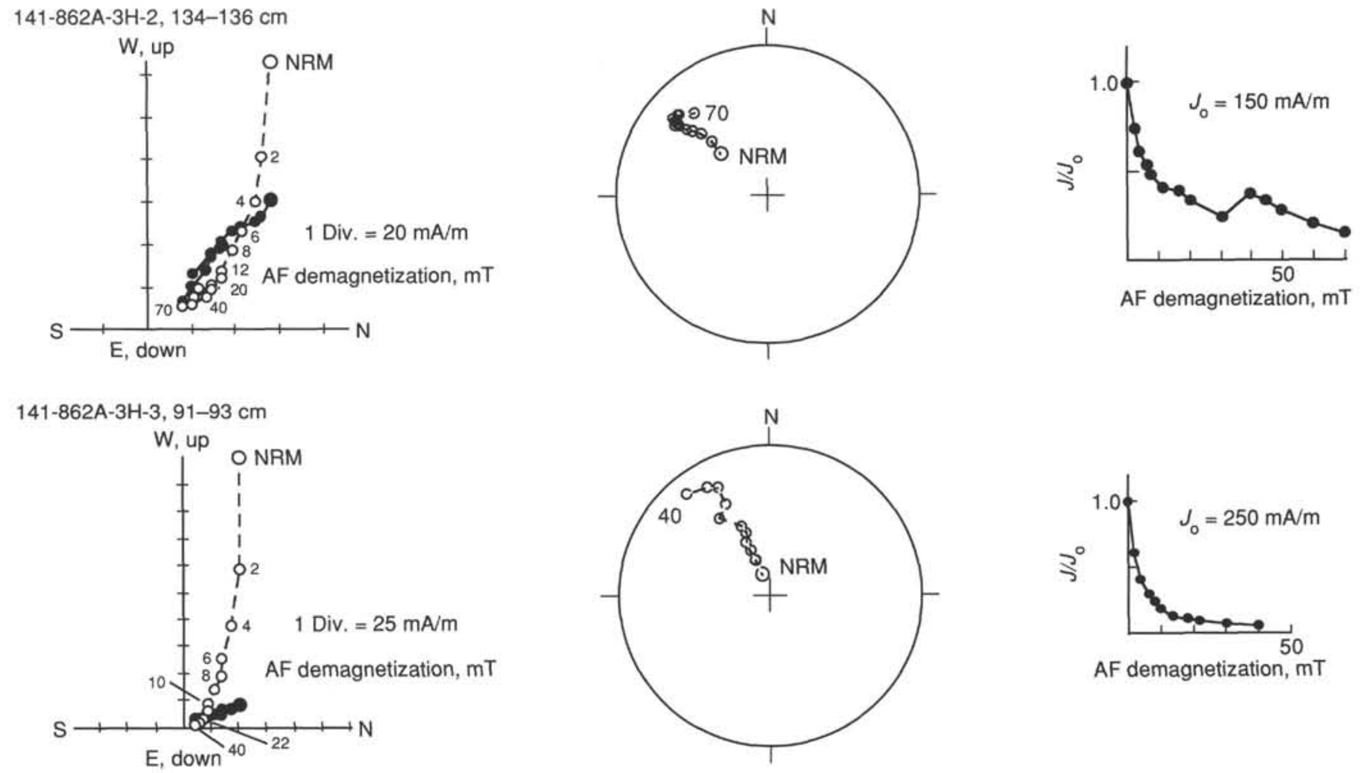

Figure 24. AF demagnetization of discrete sediment samples from Core 141-862A-3H. Zijderveld plots and stereonets as for Figure 23.

Table 9. Magnetic intensity and median destructive field of igneous rocks at Site 862.

Core, section, interval (cm)	Intensity (mA/m)	Median destructive field (mT)	Rock
141-862B-			
1W-1, 9–10	433	4	Rhyolite
1W-1, 36–38	1221	14	Dacite
3X-1, 3–5	192	11	Basalt
3X-1, 97–99	1152	95	Basalt
4X-1, 12–14	759	4	Rhyolite
4X-1, 22–24	12502	8	Basalt
4X-2, 127–129	9219	20	Basalt
141-862C-			
1W-1, 48–50	92	6	Dacite
5R-1, 5–7	321	6	Dacite
7R-1, 7-9	2150	26	Basalt
8R-1, 28–30	2300	53	Basalt

Higher up in this interval, bedding laminae define complex isoclinal recumbent fold structures. The sands in the cores of these folds are generally structureless. In Section 141-862A-3H-1, 92 103 cm, thin (2 5 mm) silty clays are interlayered with sand in the base of a sand unit. The silty clay is boudinaged and brecciated in a brittle manner and clay fragments are strung out along bedding laminae in the sand (Fig. 31). The basal 25 mm of this sand is laminated, but the sand passes rapidly upward into 60 mm of structureless sand. The structureless sand has a sharp upper contact with breccia, where breccia fragments spall off into the sand. Most sand layers show similar sequences of laminated bases becoming structureless higher up.

No normal faults are observed in the breccia domain but two linked reverse faults, dipping steeply to the west, are present in Section 141-862A-3H-1, 100 120 cm (Fig. 31). These cut the basal contact of sand on breccia with separations of 25 and 2 mm.

Sections 141-862B-2X-1 to -2X-CC, 4 cm, comprise a similar sequence of breccias and sands. There is more breccia (75% 85%) in Hole 862B although it is possible that some incipient breccias became more fragmented in the rotary action of XCB drilling.

Lower Normal-Fault Domain

This domain is restricted to Core 141-862A-3H. All orientations are quoted in the reference frame of Core 141-862A-3H. The strike of both bedding and normal faults is approximately north-south and observed apparent dips approximate to true dips. Sections 141-862A-3H-3, 88 cm, through -3H-4, 43 cm, comprise well-bedded silty clays and silts with no development of breccia. Bedding, defined by layers of coarser material including black glass fragments, dips 40° to 50° to the east and is cut by a set of normal faults dipping 40° to 55° to the west with no conjugate orientations. Faults are visible as submillimeter dark lines with separations of 1 10 mm. Many of the faults are offset along surfaces parallel to bedding, with top-to-the-east separations of 1 5 mm (Fig. 32). In Interval 141-862A-3H-3, 134 138 cm, an irregularly margined burrow 5 to 10 mm thick cuts through three bedding surfaces. The same burrow is offset along a bedding-parallel surface with 10-mm top-to-the-east separation (Fig. 33). A network of dark lines spaced 5 20 mm overlies this surface for 15 cm. At least one of these offsets the burrow.

At the base of this domain, over a 25-cm interval (141-862A-3H-4, 27 42 cm), normal faults become more intensely developed, with spacing becoming a few millimeters (Fig. 34). Over the same interval, the faults become shallower and more anastomosing. The lowermost contact is interpreted as a flat detachment over the basement interface domain.

Basement-Interface Domain

In Section 141-862B-2X-CC, 4 29 cm, relatively flat-bedded sediments overlie a sharp contact with chilled igneous rock. For

10 cm immediately above the basement interface, sediments are cut by steep normal faults with a 10- to 20-mm separation (Fig. 34). The sediment immediately above the igneous material is discolored yellow for 3 cm. The color boundary appears to pass through the faults with little or no offset.

A similar discolored horizon occurs in Section 141-862A-3H-4, 90–120 cm, suggesting that this is close to the basement contact, and the next core (Core 141-862A-4H) comprises basement cobbles in a fine matrix. Section 141-862A-3H-4, 42–120 cm, is characterized by flat bedding with a possible recumbent fold structure. A steep normal fault is present in the bottom 10 cm of this interval.

A Model for the Structure of Site 862

Geometry

Observations in the lower normal-fault domain suggest that normal faults shallow out to a detachment at 19.7 mbsf, and on a scale larger than that observed in the core are listric. Listric normal faults commonly give rise to hanging wall roll-over anticlines (Hamblin, 1965). The downward increase in the dip of bedding toward the detachment, coupled with the steeper bedding in the hanging walls of small-scale normal faults, suggests that steepening of bedding relates to roll-over on listric normal faults. For this simple geometry the inferred axis of folding should correspond to the fault intersection line. The bedding fold axis is 30° clockwise of the fault intersection (Fig. 25). Faults and fault arrays normally have displacement gradients (Walsh and Watterson, 1988) and the mismatch of fold and intersection axes may be explained by an increase in normal displacements to the northwest in the core reference frame.

The offsets of faults along bedding planes have a geometry consistent with a domino model (Burchfield and Davies, 1972) as illustrated in Figure 35. In this model a component of extension is taken up by bulk simple shear between normal faults. Blocks within the segments, in this case planes bound by bedding surfaces, rotate independently, requiring relative displacements along the bedding surfaces. In Site 862 it is usually the fault below the bedded hanging wall which is offset, indicating that this fault must have ceased operation at the time of domino rotation.

Brecciation requires dilation (Brace et al., 1966; Raleigh and Marone, 1986). In Section 141-862A-2H, 85-99 cm, breccia is developed above bedding surfaces that have slipped (D in Fig. 30) and in the footwall to a normal fault (F in Fig. 30). Dilation is a consequence of the domino model presented above. As bedding-plane slip offsets the bounding fault below a segment undergoing domino slip in a compressive sense, dilation is constrained to the region between the bedded unit and the upper bounding fault (Fig. 35). Many of the observed breccias are consistent with development in the structural environment outlined above. Breccia is constrained to one other environment: in Section 141-862A-2H, 65–78 cm, breccia is developed in the hanging wall of a normal fault with larger displacement than neighboring faults (H in Fig. 30).

Mechanisms

In the breccia domain, clays are brecciated whereas sands are not. In the upper normal-fault domain this disparity in behavior is observed on a small scale (G in Fig. 30). Some sand-on-clay contacts appear initially as erosive (e.g., Fig. 28) but it is highly unlikely that the clay became sufficiently lithified at the sediment-water interface for brecciation prior to sand deposition. It is more likely that the sands and clays have responded in different ways to deformation. There are detachments and fold structures in the sand and the lack of mesoscopically brittle behavior suggests deformation by particulate flow (Borradaile, 1981), in contrast to the clays, which fracture. In this case the sand-clay interface is likely to be a horizon of low shear strength, explaining the development of fractures subperpendicular to the interface and the apparent erosive contacts. This process is taken to an extreme in thin clays in sand which undergo boudinage and then behave as independent particles.

Within the clays there is a contrast in deformation behavior allowing slip on bedding-parallel surfaces under compression at the same time as brecciation during dilation.

Structureless sand is commonly observed and the spalling of clay breccia particles into this sand suggests that sand beds have acted as fluidized beds. Fluidization of the sand beds in the brecciated domain provides a way of accommodating the brecciation, and the detachment of some normal faults, and provides a potential source for the sand intrusions observed in the upper normal-fault domain.

Driving Forces and Environment of Deformation

A scale model for the structure of Site 862 (Fig. 36) has been developed by extrapolating the small-scale observations, particularly those from Section 141-862A-2H-4, 50–114 cm, to the large scale. The structural environments of each domain in Hole 862A, within a set of normal faults on a scale larger than those observed in core, has been assessed from the core-scale analogs. In the model it is proposed that Hole 862A provides a section through two fault blocks that detach just above the basement interface. The lower normal-fault domain is close to the lower bounding fault of the lower fault block and is characterized by domino-type structures. The upward transition into the breccia domain reflects movement closer to the upper bounding fault and a dilational environment. Brecciation and domino slip are accommodated on fluidized sands, some of which intrude upward. The upper normal-fault domain is part of the upper fault-block. Flatter bedding in the upper normal-fault domain relates to its higher level relative to the main detachment and the presence of some conjugate structures. Complex deformation does not continue up to the surface. This probably relates to the reduced quantity of sand in this domain.

Deformation post-dates lithification suggesting that the full sedimentary sequence observed was deposited before deformation related to the normal fault initiated. Alteration to ocher at the bottom of Holes 862A and 862B post-dates normal faulting.

There are no multishot or Tensor data to constrain the geographical orientation of the model and shipboard paleomagnetic results are too complex to orient the cores. Two morphotectonic features are present in the region of Site 862, giving two possible driving mechanisms and orientations for the structure of the site:

1. The structures developed in situ at Site 862. Site 862 is situated on a steep west-southwest-trending slope. The seafloor slopes 30° among Holes 862A, 862B, and 862C. It is possible that the normal-fault set that dominates the structure trends west-southwest and dips to the northwest in response to the driving force for extension provided by the topographic slope (Elliot, 1976). In this case, bedding would dip predominantly into the slope (i.e., to the southeast) and fault displacements and extension would increase to the west.
2. The sediments were deposited on the flanks of the Taitao Ridge and the structure developed as extension in response to spreading of the underlying oceanic basement. Sediment cover and oceanic basement was then tectonically translated, possibly with rotation, to Site 862. In this case, the normal faults would have formed in an approximately north-south orientation.

These options may be testable with better paleomagnetic data available from post-cruise studies using thermal demagnetization.

Table 10. Tabulation of detailed structural data on a section-by-section basis for Holes 862A and 862B.

Core, section, interval (cm)	Depth (mbsf)	X-ref. hand sheets	ID	Identifier	Core face orientation: App. dip	Core face orientation: Direction	Corrected core ref. frame: Strike	Corrected core ref. frame: Dip	Corrected core ref. frame: Dir.	Comments
141-862A-										
1H-1, 54–57	0.54	1	B	Bedding	17	90	27	19	E	
1H-1, 66–67	0.66	2	B	Bedding	12	90	45	17	E	
1H-1, 81–83	0.81	3	B	Bedding	21	90	34	24	E	
1H-1, 91–93	0.91	4	B	Bedding	20	90	24	22	E	
1H-2, 43–45	1.93	5	B	Bedding	6	90	342	6	E	
1H-2, 56–56	2.06	6	B	Bedding	3	90	67	8	S	
1H-2, 54–74	2.04	6A	F	Fault	80	90	347	80	E	
1H-2, 82–84	2.32	7	B	Bedding	9	90	18	9	E	
1H-2, 103–104	2.53	8	B	Bedding	11	90	15	11	E	
1H-2, 128–129	2.78	9	B	Bedding	8	90	45	11	E	
1H-3, 4–4	3.04	10	B	Bedding	7	90	52	11	E	
1H-3, 43–44	3.43	11	B	Bedding	8	90	20	9	E	
1H-3, 123–125	4.23	12	B	Bedding	2	270	256	8	N	
1H-3, 138–141	4.38	13	B	Bedding	20	90	47	28	S	
1H-4, 43–44	4.93	14	B	Bedding	6	90	27	7	E	
1H-CC	5.1	NIL								
2H-1, 134–134	6.74	1	B	Bedding	15	90	353	15	E	
2H-2, 20–24	7.1	2	B	Bedding	4	90	56	7	S	
2H-2, 57–60	7.47	3	B	Bedding	2	270	124	4	S	
2H-3, 35–35	8.75	4	Ft	Fault	11	90	54	18	S	
2H-3, 35–37	8.75	4	Ft	Fault	24	90	33	28	E	
2H-3, 40–47	8.8	5	Ft	Fault	58	90	17	59	E	
2H-3, 52–54	8.92	6	B	Bedding	20	270	175	40	W	
2H-3, 135–148	9.75	7	B	Bedding	11	270	195	11	W	
2H-4, 20–24	10.05	8	Ft	Fault	49	270	187	49	W	
2H-4, 24–31	10.04	8	Ft	Fault	55	90	8	55	E	
2H-4, 130–135	11.15	9	Ft	Fault	70	90	347	76	E	
2H-4, 133–134	11.18	9	B	Bedding	76	90	186	35	W	
2H-5, 2–5	11.37	10	Ft	Fault	30	90	345	31	E	
2H-5, 12–15	11.47	11	B	Bedding	18	270	208	20	W	
2H-5, 12–15	11.47	11	Ft	Fault	61	90	346	62	E	
2H-5, 78–90	12.13	12	Ft	Fault	70	90	326	73	E	
2H-5, 107–110	12.42	13	Ft	Fault	77	90	345	77	E	
2H-5, 112–116	12.47	13	B	Bedding	15	90	310	23	N	
2H-6, 19–19	13.04	14	B	Bedding	7	270	215	9	W	
2H-6, 102–102	13.87	15	B	Bedding	12	270	198	13	W	
2H-6, 102–110	13.87	15	Ft	Fault	76	270	312	80	W	
2H-7, 3–4	14.38	16	B	Bedding	13	270	159	14	W	
2H-7, 3–7	14.38	16	Ft	Fault	73	90	1	75	E	
2H-7, 50–55	14.85	17	Ft	Fault	40	90	356	40	E	
2H-7, 54–54	14.89	17	B	Bedding	10	270	163	10	W	
2H-CC	14.9									
3H-1, 23–27	15.13	1	B	Bedding	58	90	331	61	E	
3H-1, 57–63	15.47	2	B	Bedding	47	90	11	48	E	
3H-1, 98–100	15.88	3	B	Bedding	20	90	36	24	E	
3H-1, 98–104	15.88	3	Ft	Fault	57	90	347	58	E	Reverse fault
3H-1, 119–122	16.09	4	B	Bedding	31	90	27	34	E	
3H-1, 124–127	16.14	5	B	Bedding	31	90	27	34	E	
3H-2, 23–26	16.63	6	B	Bedding	27	90	33	31	E	
3H-2, 70–75	17.1	7	Ft	Fault	46	270	144	52	W	
3H-2, 80–80	17.2	8	B	Bedding	26	90	35	31	E	With small recumbent folds
3H-2, 112–117	17.52	9	Ft	Fault	69	270	189	69	W	
3H-2, 137–140	17.77	10	B	Bedding	16	90	34	19	E	

ORGANIC GEOCHEMISTRY

Shipboard organic geochemical analyses of sediments from Holes 862A and 862B included measurements of volatile hydrocarbon and nonhydrocarbon gases, organic-matter fluorescence estimation, total hexane soluble lipid/bitumen analysis, and Rock-Eval analysis. The instrumentation, operating conditions, and procedures are summarized in the Explanatory Notes chapter (this volume).

Volatile Gases from Sediments

Volatile gases (hydrocarbons, CO_2, H_2S, N_2, O_2) released by the sediments recovered at Site 862 were continuously measured by gas chromatography as part of the shipboard safety and pollution monitoring program. We used the headspace technique, in which a sediment plug is heated in a sealed vial to drive off gases (Emeis and Kvenvolden, 1986). The results are listed in Table 11. No volatile hydrocarbon gases were detected except for methane in concentrations of 5 ppm at 17.8 mbsf. Compared with a laboratory background of 2 ppm, the sedimentary methane concentrations are minor. No ethane or higher hydrocarbons, nor H_2S were detected. One vacutainer sample taken from a gas pocket from a core (Sample 141-862A-3H-4, 20–21 cm) showed no hydrocarbons (Table 11). Carbon dioxide was present at concentrations up to 894 ppm in gases desorbed from the sediments by the headspace method (Table 11).

The overall low methane contents in the sediments suggests that the conditions were not favorable for methanogenesis. Methanogenic bacteria are generally active after complete sulfate depletion by sulfate-reducing bacteria (Claypool and Kaplan, 1974). The sulfate content in interstitial waters is relatively high throughout Hole 862A (see Inorganic Geochemistry section, this chapter). Therefore, methanogenesis via CO_2 reduction, the major process by which microbial methane is produced in deep-sea sediments, was probably not possible. No compositional evidence of the presence of thermogenic hydrocarbon gases was detected. When the absence of thermogenic gases is considered in conjunction with the thermal maturational indications given by the bitu-

Table 10 (continued).

Core, section, interval (cm)	Depth (mbsf)	X-ref. hand sheets	ID	Identifier	Core face orientation App. dip	Direction	Corrected core ref. frame Strike	Dip	Dir.	Comments
141-862A-(cont)										
3H-3, 10–12	17.9	11	B	Bedding	30	90	20	32	E	
3H-3, 21–25	18.01	12	B	Bedding	40	90	353	40	E	
3H-3, 50–50	18.3	13	B	Bedding	5	90	39	6	E	
3H-3, 84–103	18.64	14	Ft	Fault	74	270	184	74	W	
3H-3, 100–103	18.8	15	B	Bedding	41	90	2	41	E	
3H-3, 112–116	18.92	16	Ft	Fault	52	270	207	55	W	
3H-3, 113–116	18.93	16	B	Bedding	52	270	18	53	E	
3H-3, 125–128	19.08	17	Ft	Fault	22	270	187	22	W	
3H-3, 134–138	19.14	18	Ft	Fault	33	270	200	35	W	
3H-3, 138–146	19.18	19	B	Bedding	43	90	28	46	E	Bedding slip fault
3H-4, 3–7	19.33	20	B	Bedding	43	90	357	43	E	Bedding slip fault
3H-4, 9–12	19.39	21	Ft	Fault	29	270	253	62	N	
3H-4, 24–27	19.54	22	B	Bedding	35	90	7	35	E	
3H-4, 37–40	19.67	23	B	Bedding	29	270	217	35	W	
3H-4, 47–49	19.77	24	B	Bedding	10	270	202	11	W	
3H-4, 50–51	19.8	25	B	Bedding	20	270	213	23	W	
3H-4, 52–54	19.82	26	B	Bedding	15	270	198	16	W	
3H-4, 59–61	19.89	27	B	Bedding	40	90	11	40	E	Right
3H-4, 59–61	19.89	27	B	Bedding	32	270	188	32	W	Left
3H-4, 70–74	20	28	B	Bedding	62	90	352	62	E	Right
3H-4, 70–74	20	28	B	Bedding	33	270	197	34	W	Left
3H-4, 82–83	20.12	29	B	Bedding	24	90	26	26	E	Right
3H-4, 82–83	20.12	29	B	Bedding	24	270	198	25	W	Left
3H-4, 93–95	20.23	30	B	Bedding	35	90	356	35	E	Right
3H-4, 93–95	20.23	30	B	Bedding	47	270	187	47	W	Left
3H-4, 100–103	20.3	31	B	Bedding	14	90	26	16	E	
3H-4, 109–120	20.39	32	Ft	Fault	54	270	193	55	W	
3H-4, 111–113	20.41	33	B	Bedding	12	90	346	12	E	
4H-1	20.6	NIL								
4H-CC	20.9	NIL								Conglomerate
141-862B-										
2X-1, 16–18	17.66	1	B	Bedding	26	90	40	32	E	
2X-1, 28–28	17.78	2	B	Bedding	0	90	270	6	N	
2X-1, 38–47	17.88	3	B	Bedding	36	270	177	36	W	Part of cross laminae
2X-1, 38–47	17.88	3	B	Bedding	20	270	175	20	W	Part of cross laminae
2X-1, 38–47	17.88	3	Ft	Fault	43	90	346	44	E	
2X-1, 38–47	17.88	3	Ft	Fault	56	270	183	56	W	
2X-1, 69–71	18.19	4	B	Bedding	35	270	177	35	W	
2X-1, 143–146	18.93	5	B	Bedding	9	270	151	10	W	Part of cross laminae
2X-1, 144–150	18.94	5	B	Bedding	23	90	41	29	E	Part of cross laminae
2X-2, 37–38	19.37	6	B	Bedding	31	270	164	32	W	
2X-2, 85–87	19.85	7	B	Bedding	15	90	56	27	S	
2X-2, 120–121	20.2	8	B	Bedding	2	270	117	4	S	
2X-2, 127–130	20.27	9	B	Bedding	3	90	53	5	S	
2X-2, 135–138	20.35	10	B	Bedding	18	270	152	20	W	
2X-3, 26–27	20.76	11	Ft	Fault	78	90	25	79	E	
2X-CC, 20–20	22.2	12	Ft	Fault	2	270	334	10	N	Bedding slip fault?
2X-CC, 21–24	22.21	13	Ft	Fault	63	270	170	63	W	
2X-CC, 23–24	22.23	14	B	Bedding	25	90	330	28	E	
2X-CC, 27–27	22.27	15	B	Bedding	12	270	230	18	N	
2X-CC, 28–28	22.28	15	B	Bedding	12	270	335	14	E	
2X-CC, 27–29	22.27	16	Ft	Fault	43	270	8	43	E	
2X-CC, 30–31	22.3	17	B	Bedding	22	270	18	24	W	

men extracts (see below), it suggests that gaseous thermogenic hydrocarbon generation has ceased and that thermogenic gases have escaped or have been washed out of the shallow sedimentary layer.

Fluorescence

The extract color was pale yellow throughout this site. The fluorescence of the extracts was blue-white and showed little variation with depth. The concentrations of extractable organic matter were low, based on the color of the extent, fluorescence intensities, and relative intensities of chromatograms of extractable organic matter (see below). White (or blue-white fluorescence) has been associated with mature and overmature bitumen enriched in polynuclear aromatic hydrocarbons (PAH), (Shipboard Scientific Party, 1982).

Bitumen Analyses and Organic Matter Characterization

The hexane extracts (500 µL) of the samples from the fluorescence assessment were concentrated under a stream of helium to about 10–40 µL. These concentrates were analyzed by high-resolution gas chromatography, and examples of traces are shown in Figure 37. The dominant compound series in the total extracts are hydrocarbons ranging from n-C_{15} to n-C_{35} with minor amounts of pristane ($C_{19}H_{40}$) and phytane ($C_{20}H_{42}$), identifiable on board the ship as the major isoprenoid alkanes.

The value of the carbon preference index (CPI) decreases with geothermal maturation approaching values of CPI ≈ 1 for crude oils and mature organic matter. For the samples of Site 862 the CPI has to be calculated for the range C_{26}-C_{35}, because in some samples n-C_{25} coelutes with a contaminant that is more abundant in samples taken from split cores and is therefore most likely associated with plastic-derived contaminants originating from core-liner fragments incorporated during core splitting. For Site 862 the organic matter extracted from the sediments has an overall low CPI value, which indicates a high degree of geothermal maturity. Relatively low CPI values ($1.0 < CPI < 2.0$) occur at 2.9 and 19.9 mbsf, and very low values ($CPI \leq 1.0$) occur in other samples (Table 12).

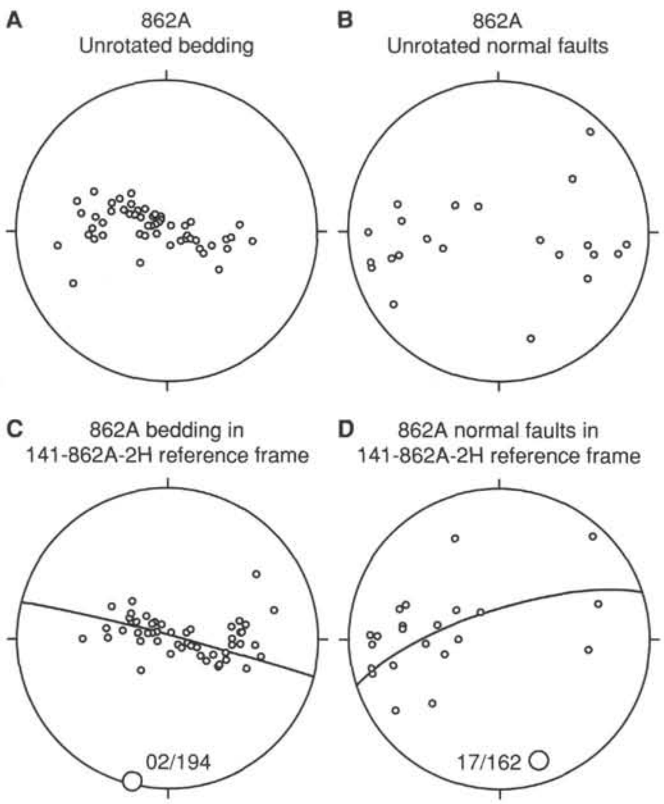

Figure 25. **A.** Stereographic projection of poles to bedding in Hole 862A. Uncorrected data in the core reference frame. **B.** Stereographic projection of poles to normal faults in Hole 862A. Uncorrected data in the core reference frame. **C.** Stereographic projection of poles to bedding in Hole 862A. Corrected data in the reference frame of Core 141-862A-2H. Great circle shows best fit to these poles. Larger open circle is the pole to the best-fit plane: the mean bedding intersection/ fold axis. **D.** Stereographic projection of poles to normal faults in Hole 862A. Corrected data in the reference frame of Core 141-862A-2H. Great circle shows best fit to these poles. Larger open circle is the pole to the best-fit plane: the mean normal-fault intersection.

The contribution of bitumen of marine origin, derived from alteration of microbial lipids (carbon-atom range $<C_{24}$; maxima about C_{20}) is predominant in most samples, whereas the organic matter from the uppermost sample at 2.0 mbsf has a predominantly terrigenous origin.

No significant depth-related trend was observed in the isoprenoid-to-normal hydrocarbon ratios (Pr/n-C_{17} and Ph/n-C_{18}), nor in the pristane to phytane ratios (Pr/Ph) (Table 12). Whereas pristane-to-phytane ratios are highly formation-dependent (Farrington et al., 1988), they have been reported to be an indicator responding to maturation (Simoneit et al., 1981), as well as an indicator of anoxic conditions of sedimentation (Didyk et al., 1978).

High concentrations of hydrocarbons in the natural-gasoline carbon-atom range (C_9 to C_{12}) were observed in a sample at 19.4 mbsf on the tailing side of the solvent elution peak when contrasted with the solvent extraction blank (Fig. 37B). The presence of gasoline-range hydrocarbons is indicative of an increased thermal stress and generation of thermogenic hydrocarbons. These thermogenic hydrocarbons could be generated by a high temperature energy source (Simoneit et al., 1981) and/or by action of hydrothermal fluids upon immature sedimentary organic matter (Didyk and Simoneit, 1989).

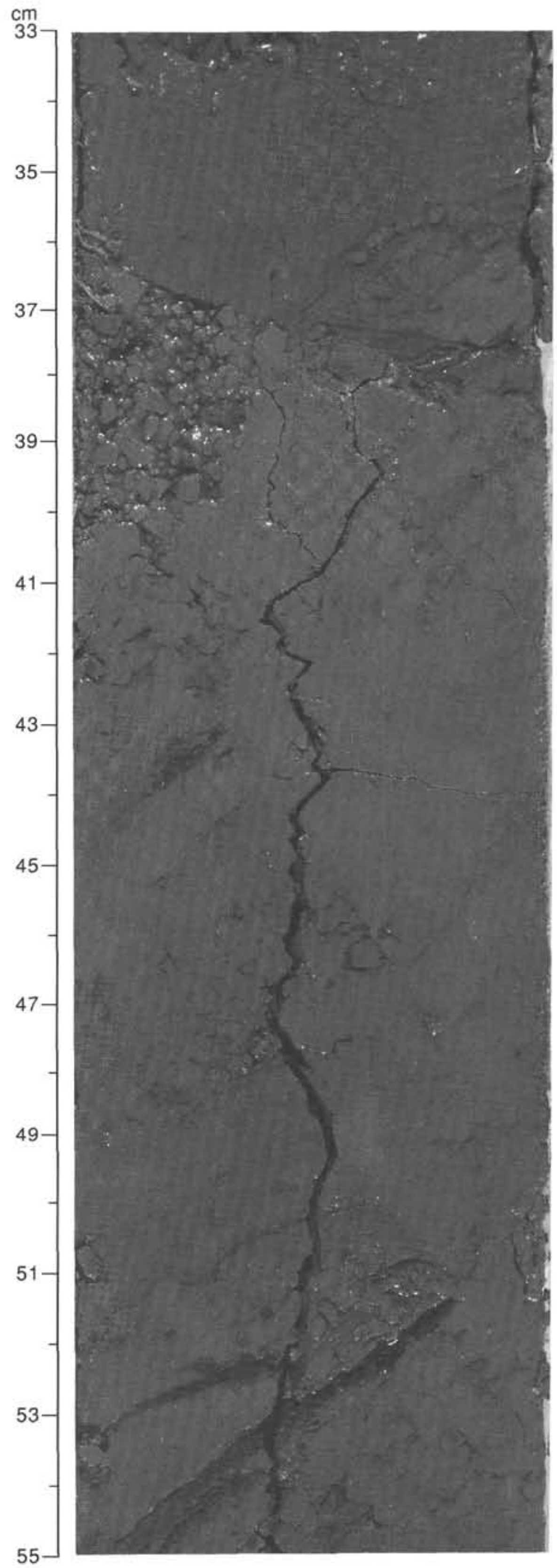

Figure 26. Core photograph, Section 141-862A-2H-3, 33–55 cm. Three normal faults cutting sand laminations and partially brecciated clay extend from top left to bottom right between 37 and 52 cm. These are truncated by a shallow fault at 36 to 37.5 cm. Bedding is steep and dips in the opposite direction to the faults.

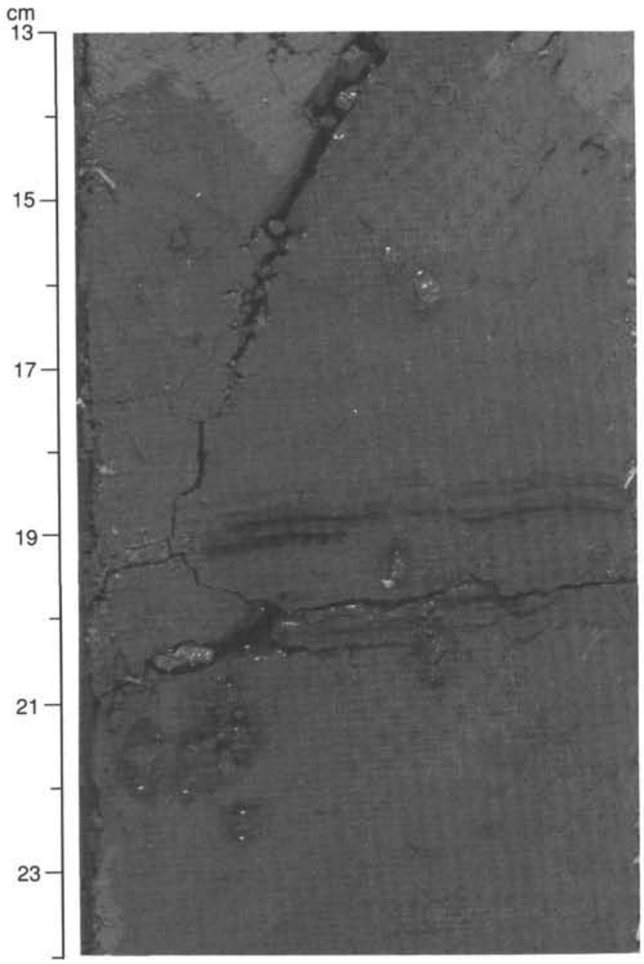

Figure 27. Core photograph, Section 141-862A-2H-6, 13–24 cm. Conjugate normal faults cutting sandy laminations (18–20.5 cm) at the base of a fining-upward sequence. Incipient brecciation develops as the sand fines to silt and clay (13–17 cm).

Organic Content and Type of Organic Matter

The content of total organic carbon (TOC) in the sediments was measured by means of the Rock-Eval pyrolysis technique (Espitalié et al., 1977). TOC values were found to be relatively low, ranging from 0.01% to 0.25% (Table 13) and to decrease with sub-bottom depth (Fig. 38). The decrease of TOC and the organic bitumen extracted from the cores suggest that decomposition of organic matter has occurred in the sediments.

In the case of low TOC such as at Site 862, both the organic-type parameters (hydrogen and oxygen indexes) and maturity parameter (T_{max}) of the Rock-Eval have little meaning due to the low accuracy of the instrument. Therefore, further analysis of the kerogen isolates will be needed to clarify the type and maturity of organic matter.

Conclusions

Only trace amounts of methane were observed, no ethane or higher hydrocarbons (C_3 to C_6) were detected. The contents of organic matter in the sediments were relatively low. The compositions of extracted bitumen and the presence of gasoline-range hydrocarbons suggest a high level of maturation of the organic matter present in the sediments.

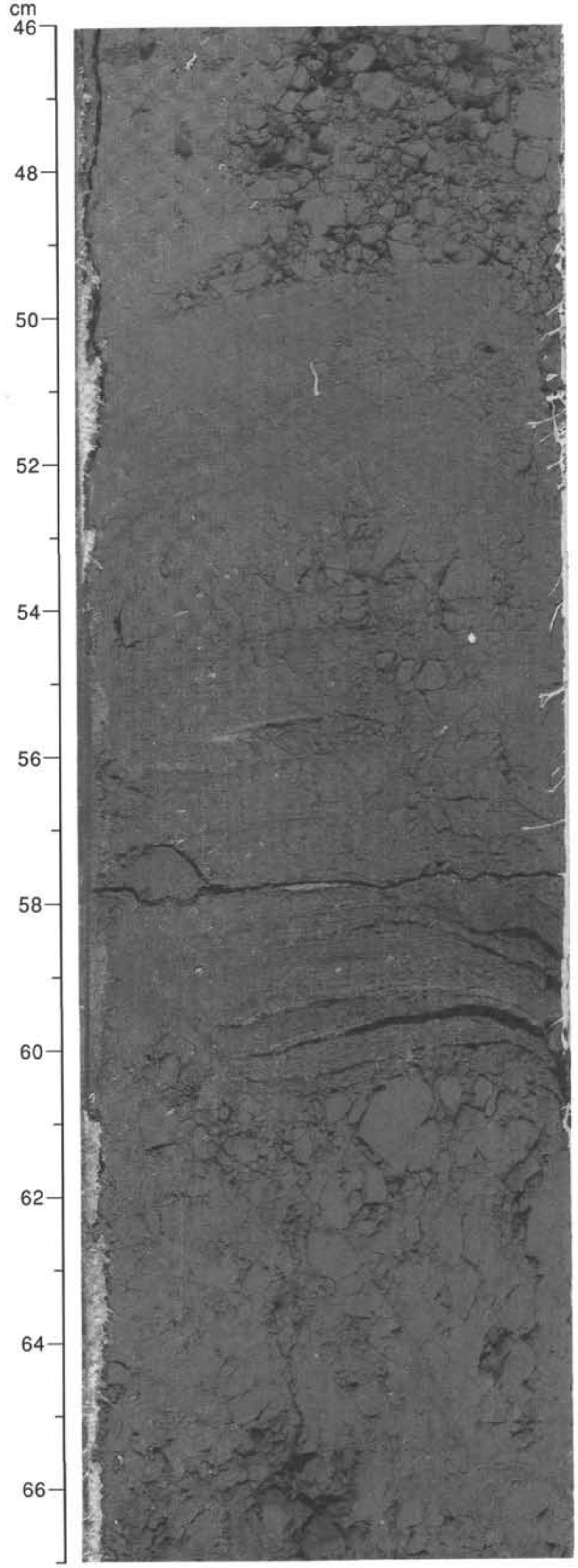

Figure 28. Core photograph, Section 141-862A-2H-2, 46–67 cm. Two normal faults dipping from left to right cut breccia and the contact of breccia and sand at 60–61 cm. The faults link at 65 cm and continue to the bottom right of the figure. Fractures in the breccia abut the sand/breccia contact at 60–61 cm.

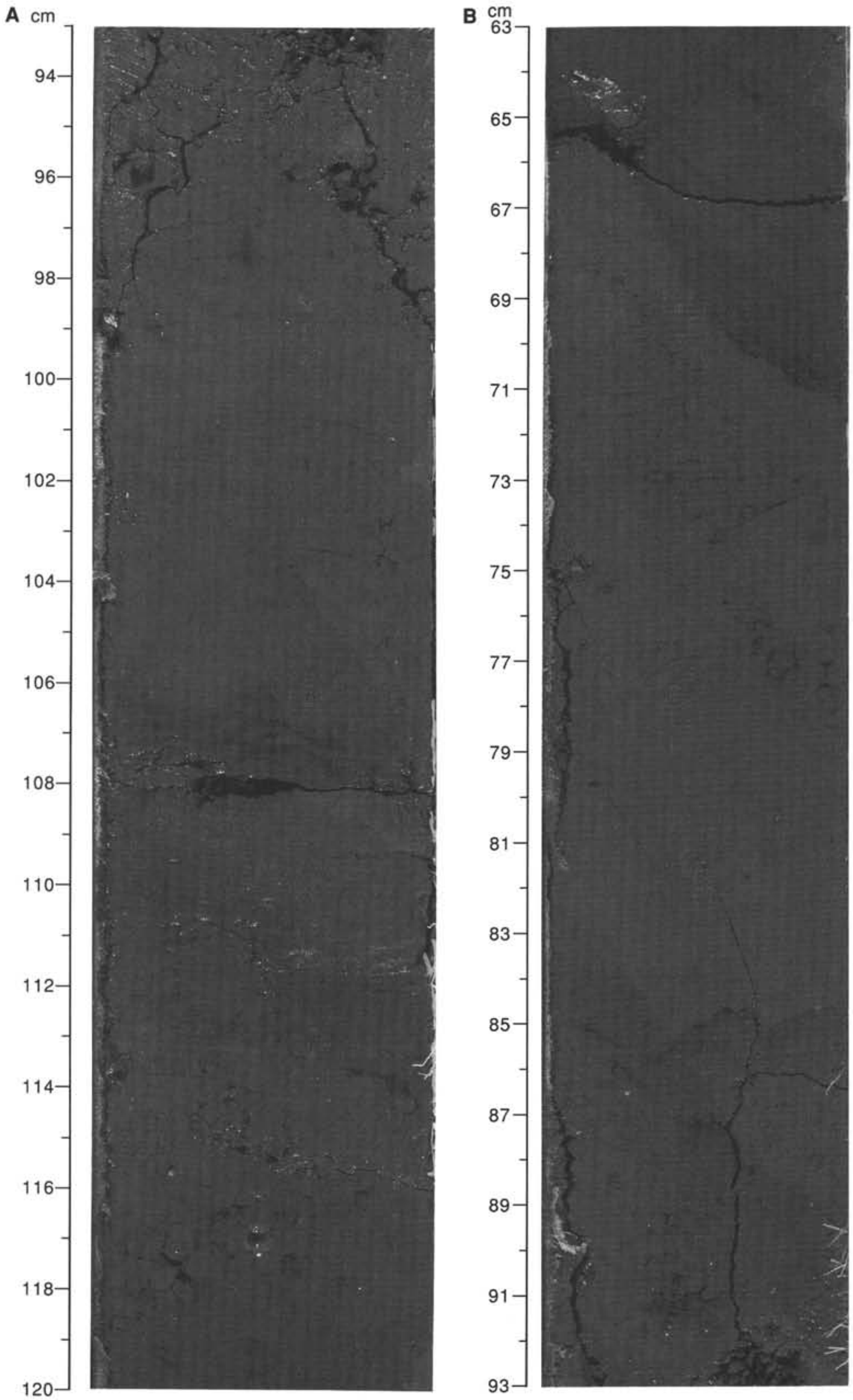

Figure 29. Core photographs. **A.** Section 141-862A-2H-5, 93–120 cm. **B.** Section 141-862A-2H-5, 63–93 cm. Intervals showing many structural features of the upper normal-fault domain. Refer to Figure 30 and the text for discussion.

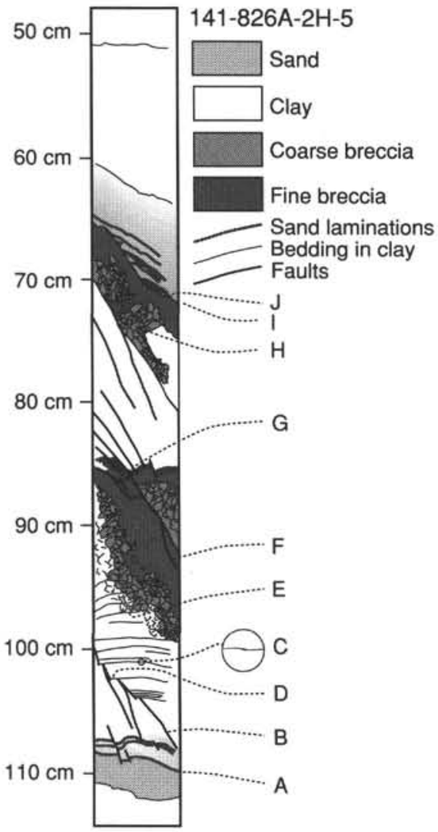

Figure 30. Section 141-862-2H-5, 48–115 cm. Line drawing of structures and lithologies shown in Figure 29. Letters refer to discussion in text.

INORGANIC GEOCHEMISTRY

The purpose of the fluid geochemistry program at Site 862, located near the crest of the Taitao Ridge, was to determine if alteration reactions in the igneous oceanic crust could be traced in the pore-fluid composition of the overlying thin sediment cover. Fluids were obtained from squeezing whole rounds in three APC cores, which correspond to the entire sediment sequence. The samples were analyzed for sodium, calcium, magnesium, potassium, ammonia, chloride, alkalinity, boron, and fluoride. These data are presented in Table 14.

Seawater sulfate levels as well as low alkalinity and ammonium values are consistent with little diagenesis of organic matter. The major-element concentrations are similar to seawater values, indicating that there is no contemporary alteration of the basalts. The formation of palagonite during the first stage of ocean crust alteration results in calcium release and magnesium uptake, none of which were observed in the pore fluids of Site 862.

PHYSICAL PROPERTIES

General

Routine laboratory procedures, which are described in the Explanatory Notes of this volume, were followed when measuring the physical properties of the thin sedimentary section drilled at Site 862. Basement rock was reached at a sub-bottom depth of about 22 mbsf; thus, only four sediment cores were available for study—three at Hole 862A and one at Hole 862B. Physical properties data were gathered from discrete samples and from the core-scanning sensors of the gamma-ray attenuation porosity

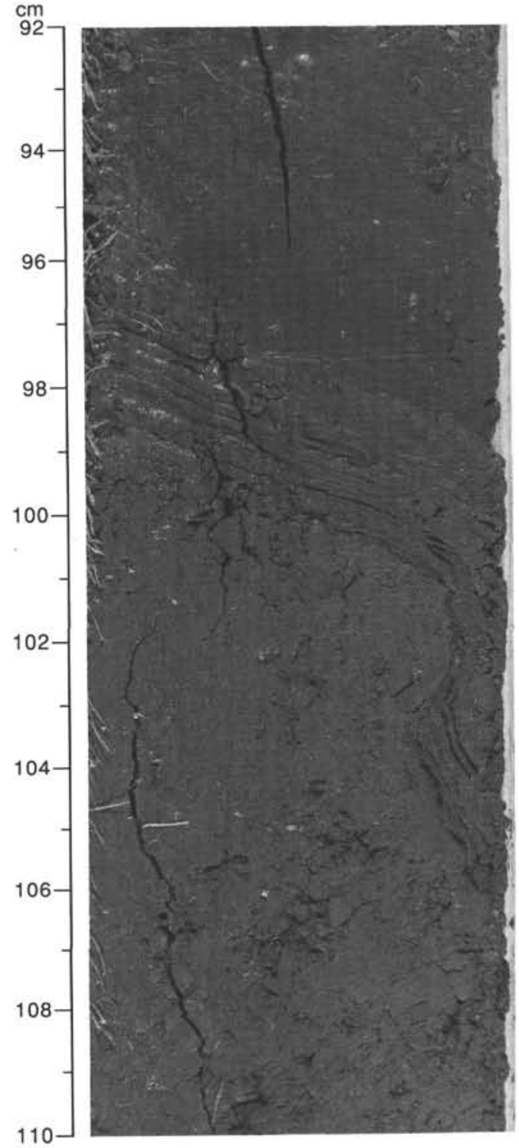

Figure 31. Core photograph, Section 141-862A-3H-1, 92–110 cm. Contact of breccia and sand at 98–100 cm. The sand is laminated at the contact, but becomes structureless upward. The upper contact of sand with breccia is just visible at 92 cm. Here, individual fragments of the upper breccia spall off into the structureless sand. In the laminated sand there are some thin clay layers that have brecciated to such an extent that individual clay particles are supported entirely in a sand matrix. The sand-breccia contact and sand laminae are offset by two reverse faults (right hand side 102–105 cm). The faults cut the breccia steeply.

evaluator (GRAPE) and *P*-wave acoustic logger (PWL). At Hole 862A, only the three uppermost APC cores were examined; the fourth core, an XCB recovery, was short (0.5 m) and composed of a disrupted mass of gravelly igneous material unsuited to the determination of in-situ physical properties. No discrete samples were measured for acoustic velocity with either the Hamilton Frame or the digital sound velocimeters.

Physical properties of the sedimentary sequence penetrated at Site 862 are described below under the headings of (1) index properties, including group porosity, water content, grain density,

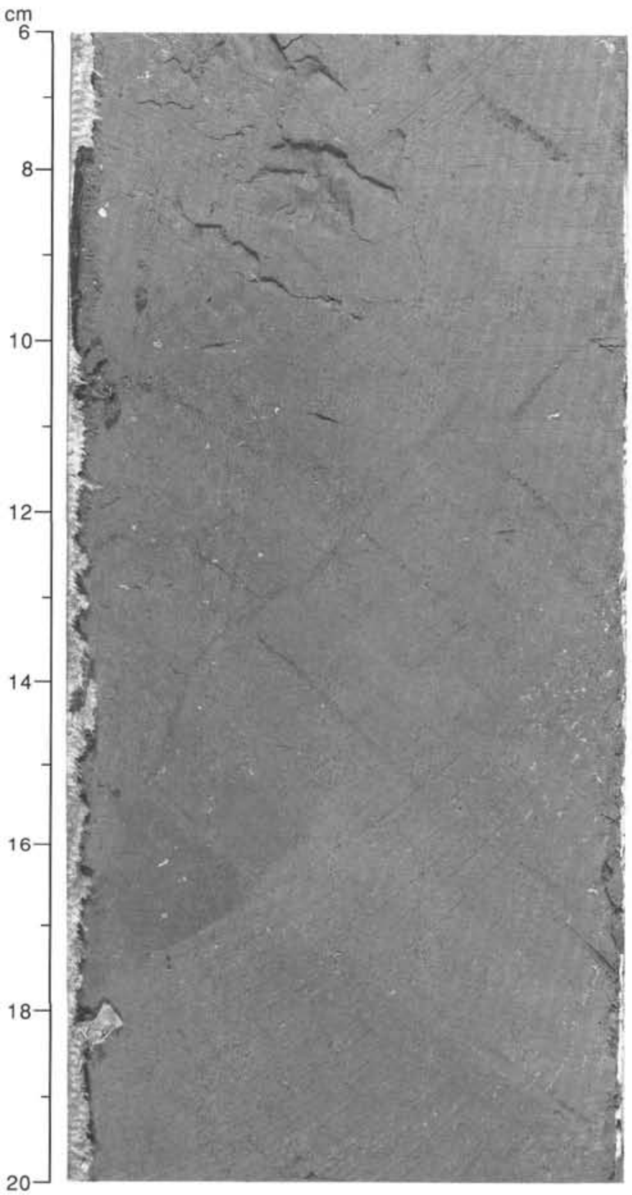

Figure 32. Core photograph, Section 141-862A-3H-4, 6–20 cm, lower normal-fault domain. A normal fault, seen as 0.5- to 1-mm-wide dark lines, dips from top right to bottom left between 10 and 15 cm. Bedding is defined by coarser layers and dips the opposite way to the fault. Separation across the fault is 18 mm. The fault is offset by surfaces parallel to bedding with normal separations of 1 to 5 mm.

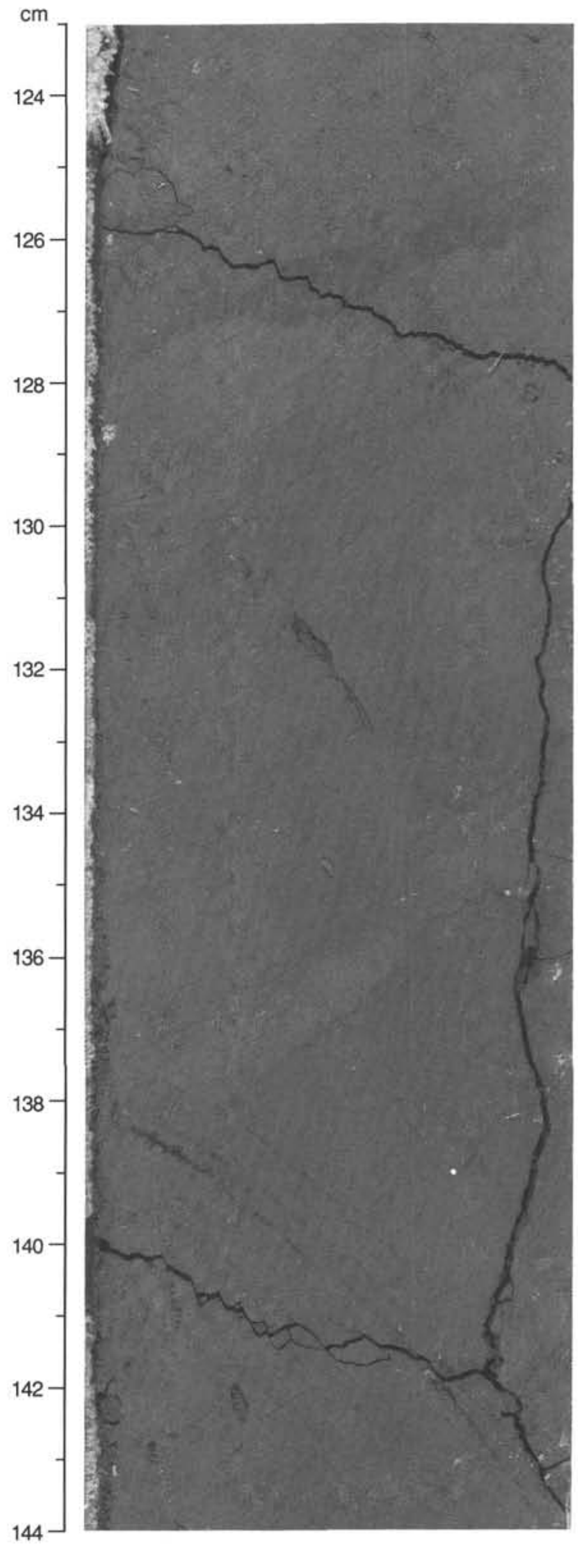

Figure 33. Core photograph, Section 141-862A-3H-3, 123–144 cm, lower normal-fault domain. A burrow, marked by a 1-cm-wide pale band with irregular dark rims, dips from top right to bottom left between 134 and 138 cm. The burrow cuts through a bedding surface at 135 cm, but is itself cut and offset by a bedding surface at 138 cm. The burrow reappears close to the left core-liner on the underside of the bedding surface and cuts two more bedding surfaces. The burrow is offset by a steep dark line at 136 cm. A dark irregular feature at 125–128 cm is probably another burrow.

and bulk density, (2) PWL information about acoustic velocity (V_p), and (3) thermal conductivity. GRAPE measurements of bulk density are included with the presentation of discrete-sample index data.

Index Properties

Index properties of selected and routine samples from Site 862 are listed in Table 15. The vertical distribution of porosity and water content, and grain and bulk sediment densities, are displayed in Figures 39 and 40, respectively.

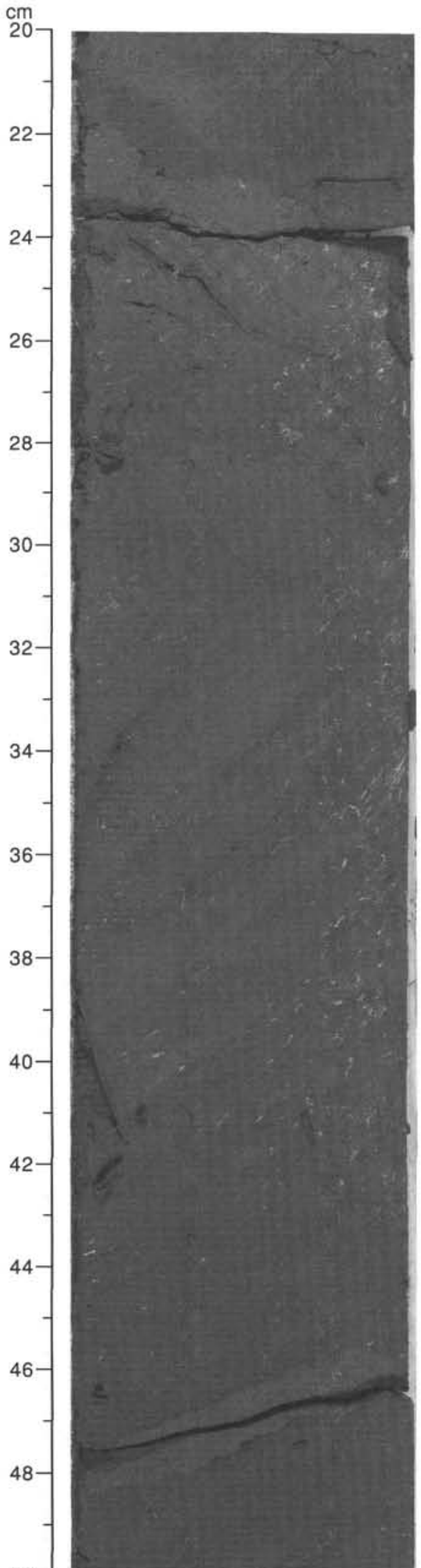

Figure 34. Core photograph, Section 141-862A-3H-4, 20–50 cm. The detachment at the base of the lower normal-fault domain. In the upper part of this interval (27–31 cm), bedding dips from top left to bottom right and is cut by normal faults dipping the opposite direction. Below this the faults become more closely spaced, begin to anastomose, and become shallower down to a flat detachment at 42 cm.

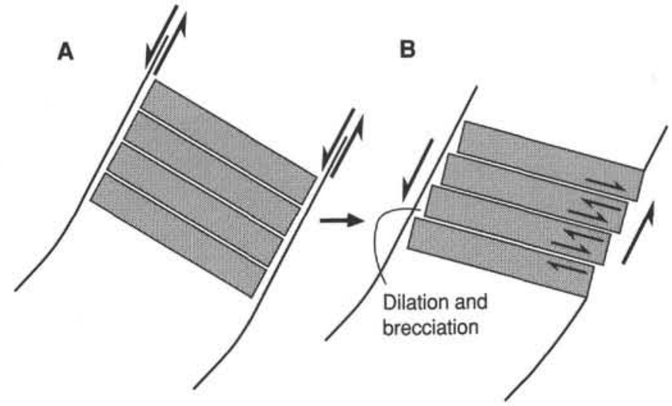

Figure 35. Domino model for the development of offsets of normal faults along bedding-parallel surfaces and dilational zones of brecciation.

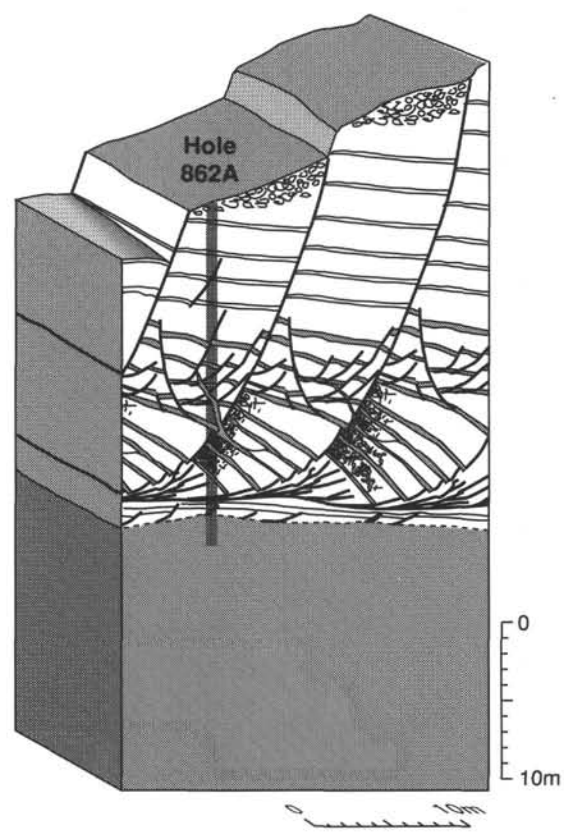

Figure 36. Scale model for the structure of Site 862.

Porosity and water content jointly show virtually no systematic downsection change. Sandy layers are conspicuously low in pore volume and water content. Near the base of the sedimentary section at about 19 mbsf, an ocher-colored clay, evidently altered by circulating hydrothermal fluids, is relatively fluid-rich and porous.

Analyses of discrete sediment samples detect no systematic change in the bulk sediment (wet) and grain density with sub-bottom depth (Table 15 and Fig. 40). The average bulk and grain densities over the sedimentary section are 1.91 and 2.77 g/cm^3, respectively. In contrast to the limited detail offered by discrete-sample measurements, GRAPE scanning of whole-round core

Table 11. Composition of headspace and Vacutainer gases for sediments from Holes 862A and 862B.

Core, section, interval (cm)	Depth (mbsf)	Hydrocarbon concentration (ppm)										
		C_1	C_2	C_3	i–C_4	n–C_4	i–C_5	n–C_5	C_{6+}	CO_2	C_1 (cm^3/cm^3)	C_1/C_2
Headspace												
141-862A-												
1H-2, 137–140	2.9	0	0	0	0	0	0	0	0	534	0.000	—
2H-4, 0–3	9.9	0	0	0	0	0	0	0	0	894	0.000	—
3H-2, 137–140	17.8	5	0	0	0	0	0	0	0	880	0.000	—
4H-CC, 10–13	20.7	0	0	0	0	0	0	0	0	813	0.000	—
141-862B-												
2X-1, 137–140	18.9	0	0	0	0	0	0	0	0	756	0.000	—
Vacutainer												
141-862A-												
3H-4, 20–21	19.6	0	0	0	0	0	0	0	0	621	0.000	—

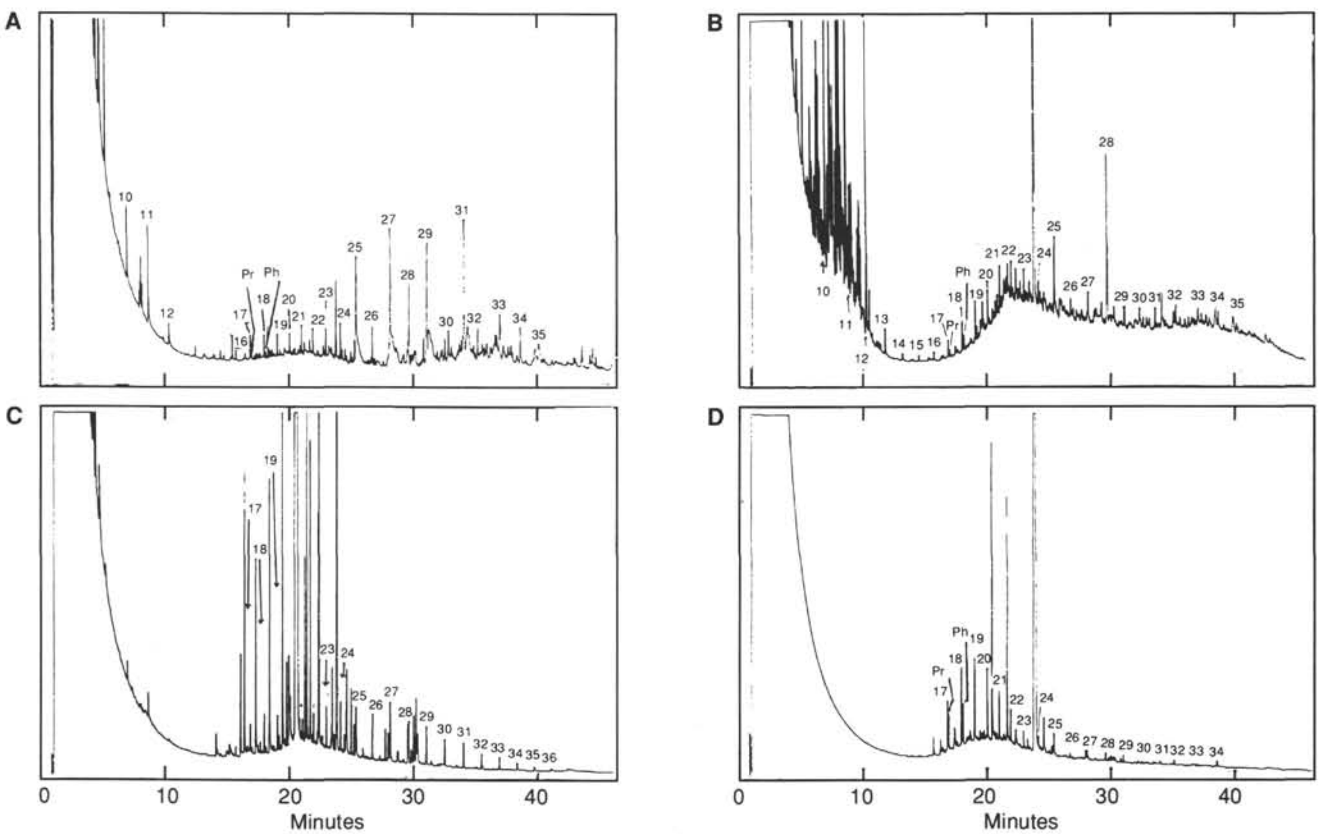

Figure 37. Gas chromatographic traces of the bitumen (hexane-soluble matter) of sediments from Holes 862A and 862B. **A.** Sample 141-862A-1H-2,137–140 cm. **B.** Sample 141-862A-3H-2, 145–150 cm. **C.** Sample 141-862B-2X-1, 147–150 cm. **D.** Sample 141-862B-2X-2, 137–140 cm (numbers refer to carbon chain length of n-alkanes, Pr = pristane, Ph = phytane).

sections reveals a gently sinuous profile of downsection changes in bulk density (Fig. 41). Excursions toward higher bulk density are thought to reflect textural changes, in particular the occurrence of sandy beds (Fig. 41). The grain density at Site 862 is virtually indistinguishable from that of much thicker sections of late Cenozoic sedimentary deposits drilled at Sites 859, 860, and 861 (see Physical Properties section, Site 861 chapter).

Sonic (V_p) Velocity

Although the data are noisy, the PWL information plotted in Figure 42 establishes that the average acoustic velocity of the Site 862 sedimentary section is close to 1600 m/s. Similar to the GRAPE results, the depth profile of velocity reveals gentle undulations in V_p readings. The slight oscillations appear to reflect changes in bulk density. Swings toward higher velocity (about 1650 m/s) appear to correspond to the location of discretely sampled sandy beds (Figs. 39 and 40) and the position of other sandy beds inferred from the GRAPE bulk density profile (Fig. 41).

Thermal Conductivity

Twelve thermal conductivity (TC) measurements were completed at Site 862. TC values for Hole 862A cores (10 measurements) and Hole 862B cores (two measurements) are listed in Table 16 and plotted vs. sub-bottom depth in Figure 43. Thermal conductivity ranges from a low of about 1.1 W/m·K to a maximum

Table 12. Extractable bitumen of sediments from Holes 862A and 862B.

Core, section, interval (cm)	Depth (mbsf)	C_{max}	C_{range} C_r–C_r	Pr/Ph	Pr/n-C_{17}	Ph/n-C_{18}	CPI	Organic matter type
141-862A-								
1H-2	2.9	31	10–36	1.25	0.25	0.22	1.85	Mar < Terr
2H-3	9.9	28	10–36	0.20	0.25	0.77	0.53	Mar > Terr
3H-2	19.4	28	10–36	0.50	0.43	0.46	0.49	Mar > Terr
3H-4	19.9	31	10–36	1.25	0.29	0.27	1.99	Mar > Terr
3H-4	20.2	28	15–36	0.18	0.15	0.55	0.96	Mar > Terr
141-862B-								
2X-1	28.6	27	10–36	0.80	0.18	0.16	0.98	Mar > Terr
2X-2	30.1	19	16–34	0.82	0.67	0.53	0.71	Mar > Terr

of a little over 1.3 W/m·K. No vertical trend of increasing or decreasing TC readings is evident in Figure 43, in keeping with the lack of systematic changes in sediment porosity and bulk density downsection (Figs. 40 and 41). The average TC value for the 12 measurements is 1.2 W/m·K, which for a sedimentary column of average bulk density near 1.9 g/cm^3 is virtually indistinguishable from sediment of similar density recovered at Sites 861 and 860.

Discussion and Overview

From the viewpoint of physical properties, one of the more interesting aspects of the thin sedimentary section penetrated at Site 862 is the absence of downsection gradients of decreasing intergranular space and moisture content. The missing gradients may reflect (1) a lack of recovery of the upper few meters of sediment, (2) a slow to very slow sedimentation rate that is much less than the rate of water venting, (3) rigidity to compaction provided by the abundance of coarse-textured deposits (Fig. 41), and (4) the possible recent loss (by erosion or mass-wasting processes) of the upper 10 or so meters of the sedimentary section. The presence of an upper Pleistocene section appears to preclude significant surface mass wasting processes (see Biostratigraphy section, this chapter). The large number of normal faults present through the sediment sequence (see Structural Geology section, this chapter) does indicate that the section has been greatly extended, but the complex structure is not reflected in the porosity profile.

The question concerning the geologic implication of the lack of a consolidation profile remains unresolved. However, when considering the general thinness of the sedimentary deposits burying the crest of the Taitao Ridge and the absence of positive overconsolidation or lithification evidence (i.e., excess bulk density and Vp) for a formerly thicker section at Site 862, we favor the notion that the profile reflects a combination of relatively low sedimentation rate and the accumulation of relatively coarse-grained material.

SUMMARY AND CONCLUSIONS

Site 862 was drilled on the Taitao Ridge during Leg 141. The purpose of Site 862 was to sample the basement rocks and overlying sediment of the Taitao Ridge, and to compare the tectonic history and evolution of the ridge with that of the Pliocene-aged Taitao ophiolite on land, and with the regional tectonic development of the triple junction region as a whole. Analyses of marine magnetic anomaly profiles, gravity data, and seismic reflection profiles across the Taitao Ridge indicated that the ridge is underlain by igneous rocks, most likely of oceanic affinity.

Site 862 is located near the crest of the Taitao Ridge, a prominent bathymetric ridge that juts out from the South American continental margin approximately 25 km south of the present location of the Chile margin Triple Junction. Because of the close proximity of the Taitao Ridge to the Taitao ophiolite, exposed 20 km to the east on the Taitao Peninsula, and marine geophysical data that suggests that the Taitao Ridge is of oceanic affinity, the Taitao Ridge was anticipated to be of oceanic origin and that it might be in the process of accretion to the Chile Trench forearc. Drilling at Site 862 confirmed that the Taitao Ridge is underlain by mafic-to-intermediate igneous material of oceanic affinity (Fig. 44), but the late Pliocene age of the sediment cover and the recovery of likely dacitic and/or rhyolitic materials indicate that the origin and tectonic evolution of the Taitao Ridge is more complex than originally hypothesized.

Two rock units were identified at Site 862: Unit I represents the thin sediment cover that blankets the Taitao Ridge and is divided into three subunits. Subunit IA, approximately 1.5 m thick, is composed of silty clay that grades to clayey silt and silty fine sand with clay. Subunit IB represents an increase in lithification of Subunit IA materials comprising claystone, silty claystone, and sandstone. Subunit IC represents the same lithology as Subunit IB, but with the addition of hydrothermal alteration deposits immediately above basement. The total sediment thickness at Site 862 is about 22 m.

Unit II is composed of apparently intercalated submarine basalt, rhyolite, and dacite flows with occasional sediment interbeds. Core 141-862B-2X recovered the depositional contact between Unit I sediment and Unit II igneous basement, and shows a 2-cm-thick hydrothermal reaction zone in the basal sediment. Igneous clasts display vesicular glassy chilled margins that can occasionally be observed to grade to variolitic plagioclase textures. Recognition of intersertal, subophitic, and ophitic textures suggest that a range of depths within cooling units was recovered.

The basalts are subalkalic to tholeiitic with phenocrysts of olivine, clinopyroxene, and plagioclase. In the dacite samples, phenocrysts often display pristine borders where they abut against plagioclase phenocrysts but are altered where they border the

Table 13. Rock-Eval and total organic carbon (TOC) of sediments from Hole 862A.

Core, section, interval (cm)	Depth (mbsf)	T_{max} (°C)	S_1 (mg/g)	S_2 (mg/g)	S_3 (mg/g)	TOC (%)	HI	OI	PI	S_2/S_3
862A-										
1H-1, 72–74	0.7	507	0.04	0.24	0.56	0.24	100	233	0.14	0.43
1H-4, 36–38	4.9	593	0.02	0.25	0.46	0.24	104	192	0.07	0.54
2H-1, 12–14	5.5	591	0.12	0.37	0.00	0.25	148	0	0.24	
2H-3, 127–129	9.7	591	0.00	0.22	0.00	0.10	220	0	0.00	
2H-6, 63–65	13.5	588	0.02	0.19	0.16	0.09	211	178	0.10	1.19
3H-1, 50–52	15.4	587	0.04	0.28	0.31	0.12	233	258	0.13	0.90
3H-2, 22–24	16.6	572	0.03	0.18	0.33	0.13	138	254	0.14	0.55
3H-4, 52–55	19.9	562	0.02	0.16	0.34	0.08	200	425	0.11	0.47
3H-4, 75–78	20.2	406	0.00	0.09	0.32	0.01	900	3200	0.00	0.28

Note: Because of low TOC, all parameters have little meaning.

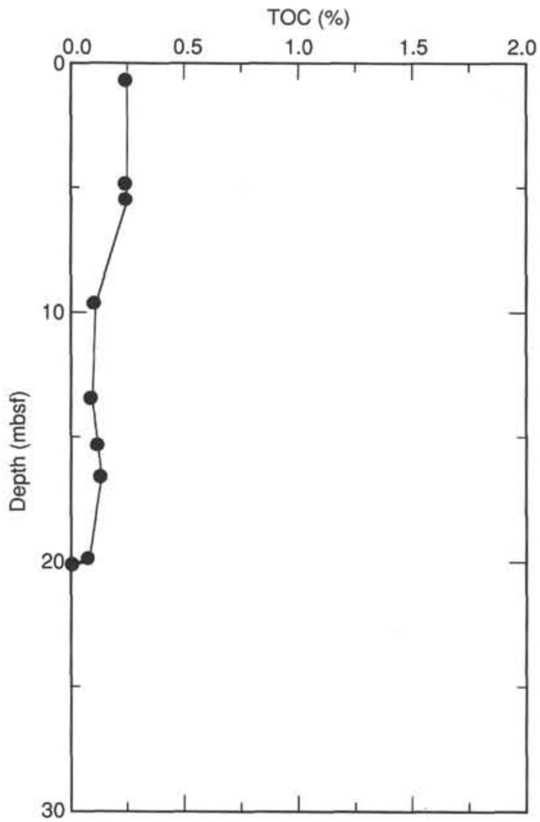

Figure 38. Total organic carbon content (Rock-Eval) vs. depth of sediments from Hole 862A.

groundmass. This suggests that, like the plagioclase, the hornblende is a primary phase in the magma chamber from which this material erupted.

Drilling may have recovered a sequence of interlayered basalt, dacite, rhyodacite, and rhyolite flows, but the small size of many of the recovered clasts may have allowed an order of recovery in the core liner that no longer reflects the original stratigraphy. What is clear, though, is that the basement of the Taitao Ridge is likely composed of a bimodal suite of basaltic and dacitic to rhyolitic eruptive materials.

Biostratigraphic observations indicate late Pliocene and Pleistocene ages for all of the recovered sediments and paleowater-depth estimates from benthic foraminifers bracket the present depth of the Taitao Ridge.

All samples from the sediments of the Taitao Ridge show normal magnetizations. Observed magnetic inclinations, however, are 30°–35° shallower than expected for this latitude, and primary magnetostratigraphy could not be determined. Complex multiple overprints in Core 141-862A-3H imply that moderate-temperature hydrothermal activity on this part of the ridge continued until after deposition of at least the lower 4.25 m of the sediment column.

Deformation of the sediment section at Site 862 is dominated by structures related to normal faulting. Both faults and bedding are often mineralized, providing dramatic planar markers for structural analysis. The local topography surrounding Site 862 is very steep, suggesting that gravity sliding may have been an important element of the deformational driving force. Recognition of boudinage of sand layers, implying some degree of brittle behavior of the sediments, suggests that deformation postdates lithification to a large extent. On the other hand, hydrothermal reaction zones overprint fault structures at the base of the sediment pile, suggesting faulting activity during the cooling of the underlying magmatic rocks. No igneous samples were recovered

Table 14. Interstitial water data obtained from squeezing whole rounds in titanium squeezers for Site 862.

Core, section, interval (cm)	Depth (mbsf)	IW vol. (mL)	Alk. (mM) (Gran)	Sal (Refr)	Cl (mM) (Tit'n)	SO_4 (mM) ($BaSO_4$)	NH_4 (mM) (Spec)	Mg (mM) (Tit'n)	Ca (mM) (Tit'n)	K (mM) (AES)	F (μM) (ISE)	B (mM) (Spec)	Ni (mM) (AES)
141-862A-													
1H-2, 145–150	3.00	25.00	2.89	35.00	560	28.60	23	51.01	10.55	13.80	75.5	0.45	539
2H-3, 145–150	9.90	36.00	3.14	35.50	558	28.70	26	50.39	10.45	14.50	88.8	0.43	536
3H-2, 145–150	18.00	32.00	2.86	35.50	558	28.70	16	51.05	9.91	14.60	65.4	0.44	538

Table 15. Index physical properties for Holes 862A and 862B.

Core, section, interval (cm)	Depth (mbsf)	Wet-bulk density (g/cm^3)	Dry-bulk density (g/cm^3)	Grain density (g/cm^3)	Wet-sediment porosity (%)	Dry-sediment porosity (%)	Wet-sediment water content (%)	Dry-sediment water content (%)	Wet-sediment void ratio	Dry-sediment void ratio
141-862-										
1H-1, 70	0.70	1.91	1.38	2.76	52.00	51.30	27.90	38.60	1.08	1.04
1H-1, 120	1.20	1.85	1.28	2.85	55.70	55.60	30.80	44.60	1.26	1.24
1H-2, 40	1.90	2.08	1.66	2.78	41.50	41.30	20.40	25.70	0.71	0.70
1H-4, 40	4.90	2.00	1.50	2.83	49.30	48.50	25.20	33.70	0.97	0.93
2H-1, 14	5.54	1.81	1.22	2.87	57.90	57.90	32.80	48.70	1.37	1.36
2H-1, 130	6.70	1.86	1.32	2.81	53.00	53.30	29.20	41.30	1.13	1.13
2H-2, 35	7.25	1.84	1.29	2.69	53.30	52.80	29.70	42.20	1.14	1.11
2H-3, 124	9.64	1.97	1.48	2.81	47.20	47.40	24.60	32.60	0.89	0.89
2H-5, 122	12.62	1.89	1.34	2.79	53.40	52.80	28.90	40.70	1.15	1.11
2H-6, 60	13.50	1.95	1.43	2.85	50.80	50.60	26.70	36.50	1.03	1.02
2H-7, 35	14.75	1.92	1.38	2.77	52.90	51.80	28.20	39.40	1.12	1.06
3H-2, 20	16.60	1.69	1.16	2.33	52.10	51.50	31.60	46.20	1.09	1.05
3H-2, 124	17.64	2.04	1.57	2.76	46.50	45.30	23.30	30.40	0.87	0.82
3H-4, 90	19.30	1.88	1.28	2.84	58.80	56.90	32.00	47.00	1.43	1.30
2X-1, 32	17.82	1.84	1.26	2.76	56.50	55.50	31.50	45.90	1.30	1.24
2X-1, 38	17.88	2.10	1.69	2.89	40.30	41.10	19.60	24.50	0.67	0.69
2X-2, 68	19.68	1.92	1.39	2.75	51.80	50.90	27.60	38.20	1.08	1.03
2X-3, 28	20.78	1.85	1.24	2.75	59.80	57.40	33.20	49.60	1.49	1.33

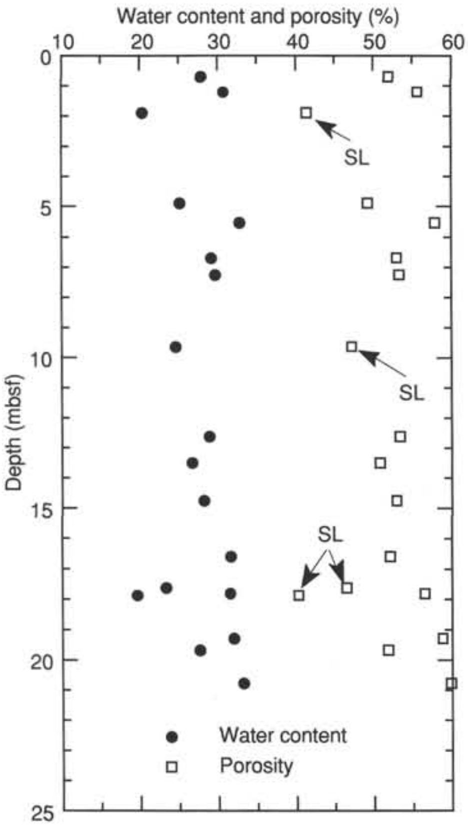

Figure 39. Discrete-sample wet-sediment water content and porosity vs. depth at Holes 862A and 862B. SL indicates samples from sand layers.

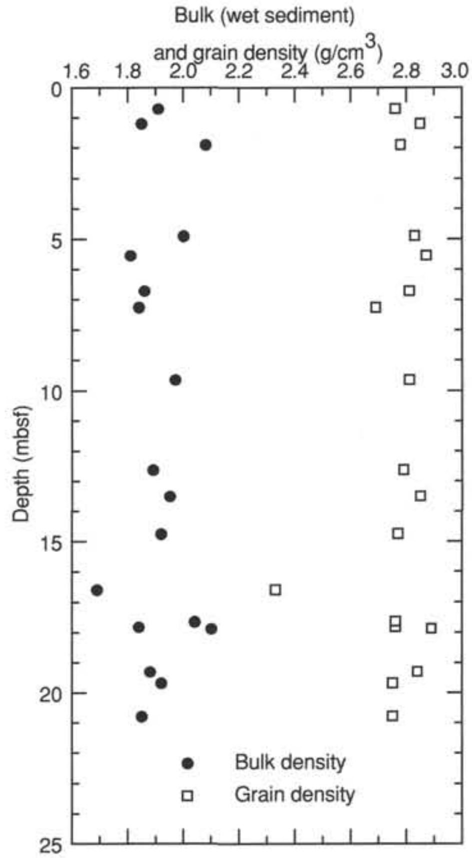

Figure 40. Discrete-sample bulk and grain densities vs. depth at Holes 862A and 862B.

in original orientation, so no structural analyses could be performed on those lithologies.

The total organic carbon content of the sediment section at Site 862 never exceeds 0.25%. CPI analysis indicates that the organic contents of all sediment samples are highly mature, as does the presence of some gasoline-range hydrocarbons. The high level of thermal maturity in such young, thin sediments that have never been deeply buried indicates deposition on hot, volcanic basement followed by vigorous hydrothermal activity. This relationship supports the inference that the Taitao Ridge cannot be much older than its sediment cover.

The seismic velocity of the sediment is about 1600 m/s throughout the thin sequence, and both bulk density and grain density are constant downsection. Similarities in these properties suggest that the sediment at Site 862 is of similar provenance to that at Sites 859 and 861.

Radiometric ages from the Taitao ophiolite are clustered between 3 and 5 Ma (early Pliocene to earliest late Pliocene), and foraminifer-bearing strata within the ophiolite yielded a late Pliocene-Pleistocene fauna (Forsythe and Prior, this volume). The probable age of the basement of the Taitao Ridge overlaps with the age of the Taitao ophiolite. Dacites and rare rhyodacites and rhyolites have been reported from the Taitao ophiolite (Forsythe and Prior, this volume), together with basalts and basaltic andesites. The similarity between this assemblage and the basement recovered at Site 862, together with the concordance in their ages, suggest that both features are genetically related and may in fact form one tectonostratigraphic unit.

Magnetic anomalies on the Antarctic Plate to the north of the Taitao Ridge at the same distance from the spreading axis correspond to the Nunivak subchron, roughly 4.2 Ma. The basement at Site 862 may be close to this age, in which case the Taitao Ridge probably arose by volcanism at the spreading axis. Alternatively, if the basement is late Pliocene in age, then Taitao Ridge volcanism occurred off the spreading axis. The strike of the Taitao Ridge follows the Taitao Fracture Zone, and it may be that the ridge arose from volcanism along this fracture zone.

Whether the Taitao Ridge formed on- or off-axis cannot be definitely stated until the basement age at Site 862 is refined. The question of whether the Taitao Ridge is currently attached to the Antarctic or the South American Plate is also unresolved for either scenario. However, if the Taitao Ridge originated along the Taitao Fracture Zone, it cannot have been attached to the South American Plate for very long, as relative motion between the Antarctic and South American plates would have slowly offset the fracture zone and the ridge once the latter was obducted.

REFERENCES

Anson, G.L., and Kodama, K.P., 1987. Compaction-induced inclination shallowing of the post-depositional remanent magnetization in a synthetic sediment. *Geophys. J. R. Astron. Soc.*, 88:673–692.

Arason, P., and Levi, S., 1990. Models of inclination shallowing during sediment compaction. *J. Geophys. Res.*, 95:4481–4500.

Borradaile, G.J., 1981. Particulate flow of rock and the formation of cleavage. *Tectonophysics*, 72:305–321.

Brace, W.F., Paulding, B.W., and Scholz, C.H., 1966. Dilatancy in the fracture of crystalline rocks. *J. Geophys. Res.*, 71:3939–3953.

Burchfield, B.C., and Davies, G.A., 1972. Structural framework and evolution of the southern part of the Cordilleran orogeny, Western United States. *Am. J. Sci.*, 272:97–118.

Claypool, G.E., and Kaplan, I.R., 1974. The origin and distribution of methane in marine sediments. *In* Kaplan, I.R. (Ed.), *Natural Gases in Marine Sediments:* New York (Plenum), 99–139.

Deamer, G.A., and Kodama, K.P., 1990. Compaction-induced inclination shallowing in synthetic and natural clay-rich sediments. *J. Geophys. Res.*, 95:4511–4530.

Didyk, B.M., and Simoneit, B.R.T., 1989. Hydrothermal oil of Guaymas Basin and implications for petroleum formation mechanisms. *Nature*, 342:65–68.

Didyk, B.M., Simoneit, B.R.T., Brassell, S.C., and Eglinton, G., 1978. Organic geochemical indicators of palaeoenvironmental conditions of sedimentation. *Nature*, 272:216–222.

Elliot, D., 1976. The energy balance and deformation mechanism of thrust sheets. *Philos. Trans. R. Soc. London A*, 283:289–312.

Emeis, K.-C., and Kvenvolden, K.A., 1986. Shipboard organic geochemistry on JOIDES Resolution. *ODP Tech. Note*, 7.

Espitalié, J., Madec, M., Tissot, B., Menning, J.J., and Leplat, P., 1977. Source rock characterization method for petroleum exploration. *Proc. 9th Ann. Offshore Technol. Conf.*, 3:439–448.

Farrington, J.W., Davis, A.C., Tarafa, M.E., McCaffery, M.A., Whelan, J.K., and Hunt, J.M., 1988. Bitumen molecular maturity parameters in the Ikpikpuk well, Alaskan North Slope. *Org. Geochem.*, 13:303–310.

Fisher, R.V., and Schmincke, H.-U., 1984. *Pyroclastic Rocks:* New York (Springer Verlag).

Forsythe, R.D., and Nelson, E., 1985. Geological manifestations of ridge collision: evidence from the Golfo de Penas-Taitao Basin, Southern Chile. *Tectonics*, 4:477–495.

Hamblin, W.K., 1965. Origin of "reverse drag" on the down-throw side of normal faults. *Geol. Soc. Am. Bull.*, 76:1145–1164.

King, R.F., 1955. Remanent magnetization of artificially deposited sediments. *Mon. Notes R. Astr. Soc., Geophys. Suppl.*, 7:115–134.

Kroenke, L.W., Berger, W.H., and Janecek, T.R., et al., 1991. *Proc. ODP, Init Rept.*, 130: College Station, TX (Ocean Drilling Program).

Levi, S., and Banerjee, S., 1990. On the origin of inclination shallowing in redeposited sediments. *J. Geophys. Res.*, 95:4383–4390.

Lutze, G.F., and Altenbach, A., 1988. *Rupertina stabilis* (Wallich), a high adapted, suspension feeding foraminifer. *Meyniana*, 40:55–69.

Musgrave, R.J., Delaney, M.L., Stax, R., and Tarduno, J.A., in press. Magnetic diagenesis, organic input, interstitial-water chemistry, and the paleomagnetic record of the carbonate sequence on the Ontong Java Plateau. *In* Berger, W., Kroenke, L., and Mayer, L., *Proc. ODP, Sci. Results*, 130: College Station, TX (Ocean Drilling Program).

Piper, D.W.J., 1978. Turbidite muds and silts in deepsea fans and abyssal plains. *In* Stanley, D.J., and Kelling, G. (Eds.) *Sedimentation in Submarine Canyons, Fans, and Trenches:* Stroudsburg, PA (Dowden, Hutchison, and Ross).

Raleigh, C.B., and Marone, C., 1986. Dilatancy of quartz gouge in pure shear. *In* Hobbs, B.E., and Heard, H. (Eds.), *Mineral and Rock Deformation: Laboratory Studies.* Am. Geophys. Union, Geophys. Monogr., 36:1–10.

Reading, H.G., 1978. *Sedimentary Environments and Facies:* New York (Elsevier).

Sanfilippo, A., Westberg-Smith, M.J., and Riedel, W. 1985. Cenozoic radiolaria. *In* Bolli, H.M., Saunders, J.B., and Perch-Nielsen, K. (Eds.), *Plankton Stratigraphy:* Cambridge (Cambridge Univ. Press), 631–712.

Shipboard Scientific Party, 1982. Guaymas Basin: Sites 477, 478, and 481. *In* Curray, J.R., Moore, D.G., et al., *Init. Repts. DSDP*, 64 (Pt. 1): Washington (U.S. Govt. Printing Office), 210–415.

Simoneit, B.R.T., Brenner, S., Peters, K.E., and Kaplan, I.R., 1981. Thermal alteration of Cretaceous black shale by basaltic intrusions in the eastern Atlantic. II: Effects on bitumen and kerogen. *Geochim. Cosmochim. Acta*, 45:1581–1602.

van Morkhoven, F.P.C.M., Berggren, W.A., and Edwards, A.S., 1986. Cainozoic cosmopolitan deep-water benthic foraminifera. *Bull. Cent. Rech. Explor.-Prod. Elf-Aquitaine*, 11:1–421.

Verosub, K.L., 1977. Depositional and postdepositional processes in the magnetization of sediments. *Rev. Geophys. Space Phys.*, 15:129–143.

Walsh, J.J., and Watterson, J.S., 1988. Analysis of the relationship between displacement and dimensions of faults. *J. Struct. Geol.*, 10:238–347.

Ms 141IR-109

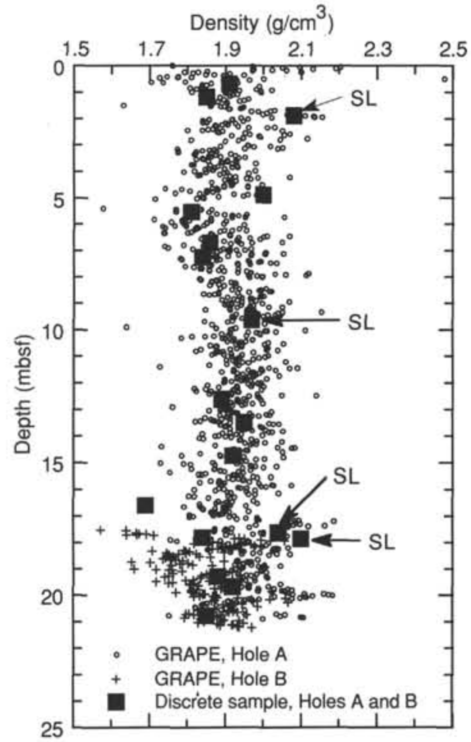

Figure 41. Discrete-sample and GRAPE measurement of wet-sediment bulk density vs. depth at Holes 862A and 862B. SL indicates discrete samples taken from sand layers. A possible sand layer at the base of the section was not sampled but has been inferred from a strong positive swing of GRAPE bulk-density values.

NOTE: For all sites drilled, core-description forms ("barrel sheets") and core photographs have been reproduced on coated paper and can be found in Section 3, beginning on page 449. Forms containing smear-slide data can be found in Section 4, beginning on page 665. Thin-section data are given in Section 5, beginning on page 691.

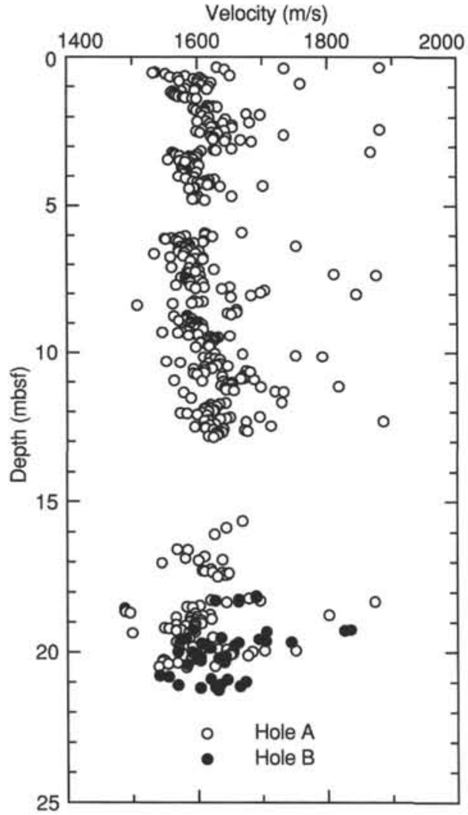

Figure 42. *P*-wave logger (PWL) determination of sediment acoustic velocity (V_P) vs. depth at Holes 862A and 862B.

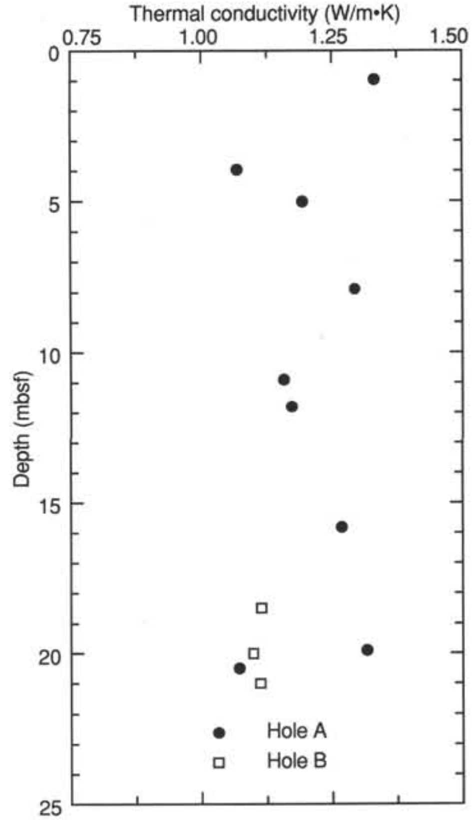

Figure 43. Thermal conductivity vs. depth at Holes 862A and 862B.

Table 16. Thermal conductivity measurements for Holes 862A and 862B.

Core, section, interval (cm)	Depth (mbsf)	Thermal conductivity (W/m·K)
141-862A-		
1H-1, 96	0.96	1.33
1H-3, 96	3.96	1.07
1H-4, 50	5.00	1.19
2H-2, 100	7.90	1.29
2H-4, 100	10.90	1.16
2H-7, 40	11.80	1.17
3H-1, 90	15.80	1.27
2X-1, 100	18.50	1.11
3H-4, 50	19.90	1.32
2X-2, 100	20.00	1.10
3H-4, 109	20.49	1.07
141-862B-		
2X-3, 50	21.00	1.11

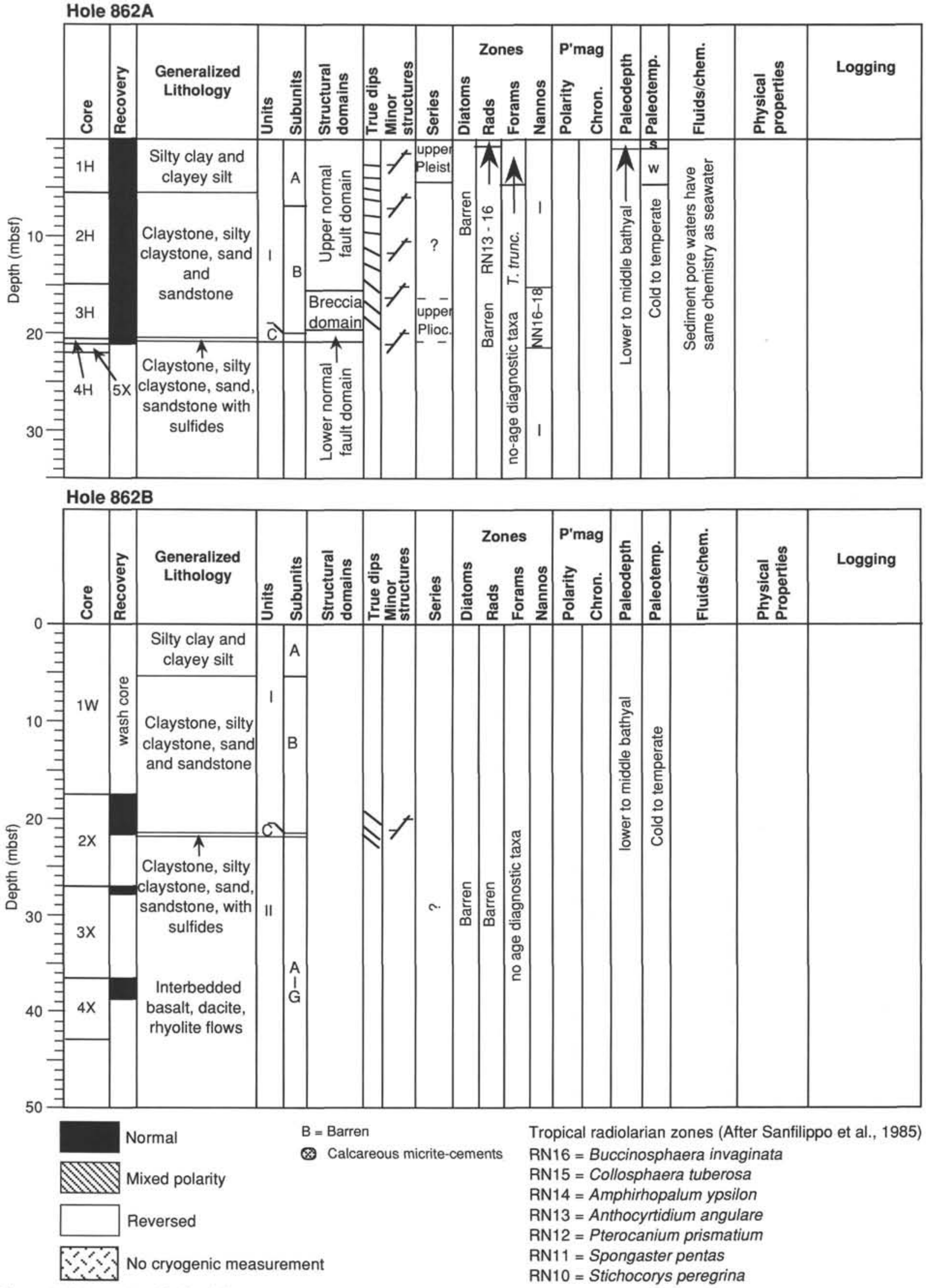

Figure 44. Master chart for Site 862.

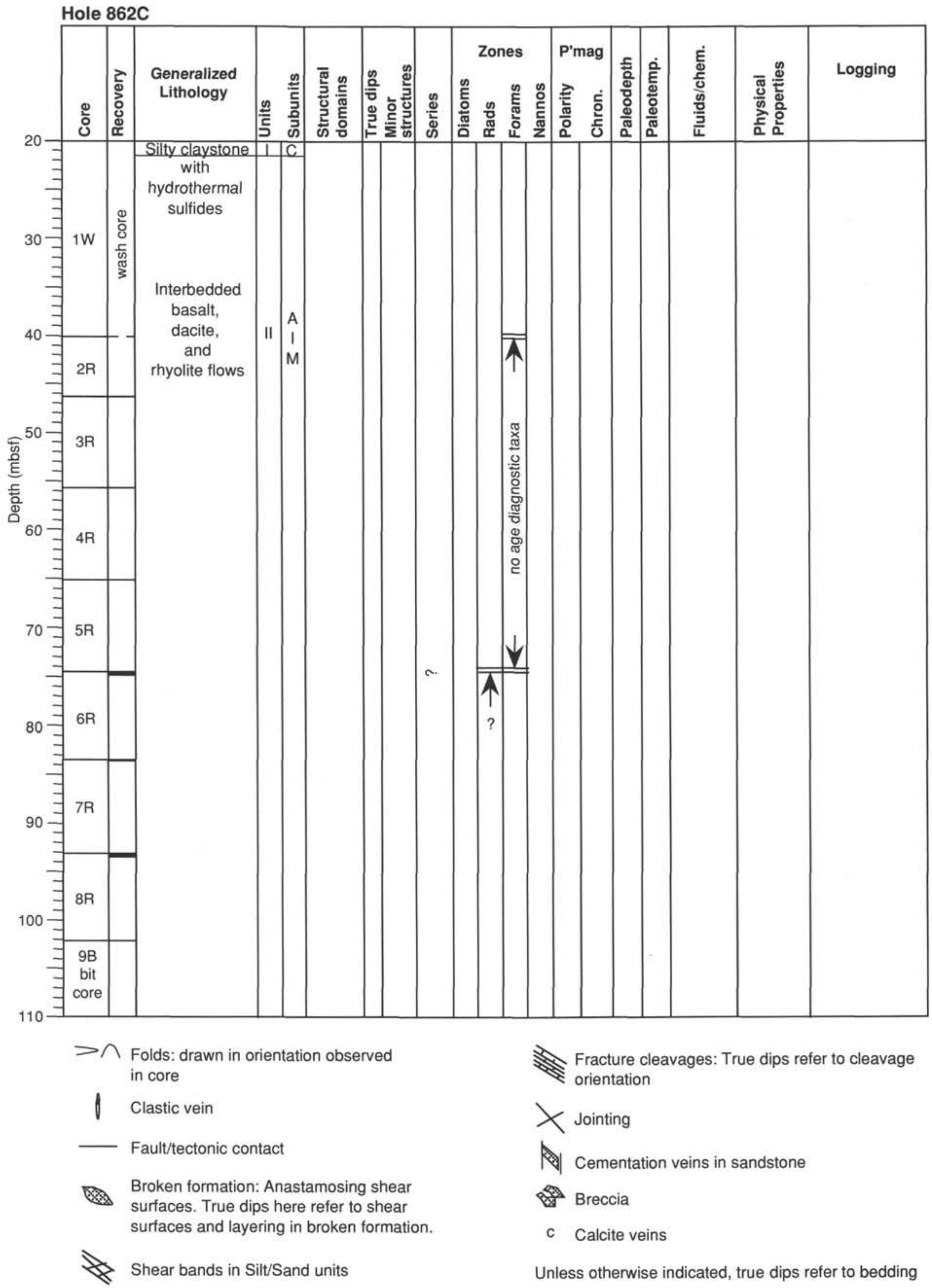

Figure 44 (continued).